Geometric Modeling and Characterization of the Circle of Willis

Hrvoje Bogunović

TESIS DOCTORAL UPF / 2012

Thesis submitted in partial fulfillment of the requirements
for the degree of Doctor of Philosophy.

Departament de Tecnologies de la Informació i les Comunicacions
Universitat Pompeu Fabra

Cover design by the author using Adobe Illustrator and MATLAB. The front cover presents the geometric model of the cerebral arteries extracted from an image shown by its three principal maximum intensity projections. The arterial segments of the model forming the Circle of Willis are denoted in green. The back cover illustrates the geometric characterization of the terminal bifurcation and the siphon segments of the internal carotid artery.

Geometric Modeling and Characterization of the Circle of Willis

ISBN: 978-84-615-9731-4

Typeset in LaTeX.

Director Prof. Alejandro F. Frangi
Associate Professor
Universitat Pompeu Fabra, Barcelona, Spain
Professor of Biomedical Image Computing
University of Sheffield, Sheffield, UK

Co-director Dr. José María Pozo
Visiting Professor
Universitat Pompeu Fabra, Barcelona, Spain
Research Associate
University of Sheffield, Sheffield, UK

Reading Committee:

Prof. Wiro Niessen
Erasmus Medical Center, Rotterdam, The Netherlands

Prof. Vicent Caselles
Universitat Pompeu Fabra, Barcelona, Spain

Dr. Petia Radeva
Universitat de Barcelona, Barcelona, Spain

Dr. Joan Martí Bonmatí (Reserve)
Universitat de Girona, Girona, Spain

Dr. Coloma Ballester (Reserve)
Universitat Pompeu Fabra, Barcelona, Spain

This work was carried out in the Center for Computational Imaging and Simulation Technologies in Biomedicine (CISTIB), at the Departament de Tecnologies de la Informació i les Comunicacions at the Universitat Pompeu Fabra, Barcelona, Spain. The work was partially supported by: the @neurIST Integrated Project (co-financed by the European Commission through the contract no. IST-027703), the FI-DGR 2009 fellowship of AGAUR, the Agency for Administration of University and Research Grants of the Regional Government of Catalonia, the CENIT programme of CDTI, the Industrial and Technological Development Centre of the Spanish Ministry of Science and Innovation, under the research projects CDTEAM and cvREMOD (CEN-20091044), and Philips Healthcare B.V. (Best, The Netherlands).

Mami, tati i seki

Contents

List of Figures

List of Tables

List of Acronyms

χ^2	Chi-square
1D	One-dimensional
2D	Two-dimensional
3D	Three-dimensional
3DRA	3D Rotational Angiography
ACA	Anterior Cerebral Artery
AcoA	Anterior Communicating Artery
AMC	Academic Medical Center
ANOVA	Analysis of Variance
BA	Basilar Artery
BoI	Bifurcations of Interest
CE	Contrast Enhanced
CeVD	Cerebrovascular Disease
CFD	Computational Fluid Dynamics
CI	Confidence Interval
CMDS	Classical Multidimensional Scaling
CoW	Circle of Willis
CT	Computed Tomography
CTA	Computed Tomography Angiography
CV	Cross-Validation
DSA	Digital Subtraction Angiography
FDA	Functional Data Analysis
FOV	Field of View
GAR	Geodesic Active Regions
GRAPPA	Generalized Autocalibrating Partially Parallel Acquisition
HCPB	Hospital Clinic i Provincial de Barcelona
HU	Hounsfield Units
ICA	Internal Cerebral Artery
IIS	Image Intensity Standardization
ISE	Iso-intensity Surface Extraction
KB	Knowledge Base
LBFGSB	Limited memory Broyden Fletcher Goldfarb Shannon with Simple Bounds
LDA	Linear Discriminant Analysis
LDDMCM	Large Deformation Diffeomorphic Metric Curve Mapping

LDDMM	Large Deformation Diffeomorphic Metric Mapping
LoA	Limits of Agreement
MAP	Maximum A Posteriori
MCA	Middle Cerebral Artery
ML	Maximal Likelihood
MOTSA	Multiple Overlapping Thin Slab Acquisition
MRA	Magnetic Resonance Angiography
MRI	Magnetic Resonance Imaging
MVA	Multivariate Analysis
MVN	Multiple Valued Neuron
NC	Non-Contrast
NN	Nearest Neighbors
OPR	Out-of-Plane Rotation
PC	Phase Contrast
PCA	Posterior Cerebral Artery
PcoA	Posterior Communicating Artery
PGA	Principal Geodesic Analysis
rARG	Rooted Attributed Relational Graph
RKHS	Reproducing Kernel Hilbert Space
ROI	Region of Interest
SAH	Subarachnoid Hemorrhage
SD	Standard Deviation
SENSE	Sensitivity Encoding
SFS	Sequential Forward Selection
SNR	Signal-to-Noise Ratio
SVM	Support Vector Machine
TB	Terminal Bifurcation
TE	Echo Time
ToF	Time-of-Flight
TR	Repetition Time
VEGF	Vascular Endothelial Growth Factor

Preface

The thesis that follows would never have seen the light of day without the support of many people. First and foremost I would like to express my gratitude to my co-supervisors: Alejandro Frangi and José María Pozo. To Alex for giving me the opportunity to embark on this journey, building such a diverse lab and advising me throughout the years. To José for his day-to-day guidance, rigorous research and infinite patience. I was also fortunate to be working within the team led by Rubén Cárdenes and María Cruz Villa-Uriol, who besides providing leadership and insights, readily served as psychologists when the going got tough. I would also like to thank Alessandro Radaelli, for taking care of me in the initial period of the thesis. Further, I am grateful to the fellow "angio" students Chong Zhang, Arjan Geers, Hernán Morales, and Ján Margeta for all the discussions we had and for keeping me company in the office until late at night.

I would like to thank all my clinical coauthors for keeping my research within clinically applicable context and helping out with the validation. To Juan Macho, Luis San Román and Jordi Blasco from Hospital Clinic, Barcelona. To Charles Majoie, and René van den Berg from Academic Medical Center, Amsterdam. To Raphaël Blanc and Michel Piotin from Fondation Rothschild, Paris. To Hugo Gratama van Andel for revealing to me many secrets behind angiographic imaging.

Big thanks to all the current and past members of the lab, who made the atmosphere so enjoyable and kept the spirits high. They all would deserve a special mention, but would make the acknowledgments longer than the thesis.

Na kraju, najvažnije, neizmjerno sam zahvalan mojoj obitelji i prijateljima, koji su bili uz mene svih ovih godina doktorata i redovito me zvali iako sam ja rijetko nalazio vremena da se javim.

Abstract / Resumen

Abstract. Cerebrovascular diseases can result in stroke, which is among the leading causes of morbidity and mortality in the developed countries. There is a growing interest in understanding the factors that influence the risk of stroke and how blood is distributed throughout the brain. This motivated a search for "geometric risk factors", the configurations of vasculature that provoke high hemodynamic stress on the vessel wall, which is assumed to be associated with the development of vascular diseases.

The goal of this thesis was the development of methods that starting from angiographic image enable the geometric analysis of the major cerebral vasculature, in particular the part known as the Circle of Willis (CoW), which exhibits a large anatomical variability and is a common site of diseases. Special emphasis was put on making methods automated to produce results that are objective (operator-independent) and repeatable to minimize variability propagation to later analysis. The path to the goal was divided into three subgoals. Each subgoal resulted in a scientific contribution published or submitted to a peer-review journal.

In the first contribution we improve a vascular segmentation method to achieve robustness in segmenting images coming from different imaging modalities and clinical centers and we provide exhaustive segmentation validation. The validation was performed on 3D rotational angiography and magnetic resonance angiography images, the two modalities used for the proposed characterization. Once the vasculature is successfully segmented, in the second contribution we propose a methodology to extensively characterize the geometry of the internal carotid artery (ICA), which due to its large geometric variability has been of special interest as a potential risk factor for the onset or rupture of aneurysms. This includes the development of a method to automatically identify the ICA from the segmented vascular tree. Finally in the third contribution, this automated identification is generalized from individual vessel to a collection of vessels including their connectivity and topological relationships. This is presented as a method for anatomical labeling of the vascular segments forming the entire CoW. Identifying the corresponding vessels in a population enables comparison of their geometry using the methodology introduced for the characterization of the ICA. Thus, the above three contributions complete our initially considered goal.

Resumen. Una de las causas principales de morbilidad y mortalidad en los países desarrollados son los derrames cerebrales, asociados a enfermedades cerebrovasculares. Existe un creciente interés en la comprensión de los factores de riesgo que influyen en la aparición de derrames cerebrales así como los factores que determinan la distribución sanguínea en el cerebro. Esto ha motivado una búsqueda de "factores geométricos de riesgo", como configuraciones del sistema vascular que provocan alto estrés hemodinámico en las paredes de las arterias, que se cree que están asociadas con el desarrollo de enfermedades vasculares.

El objetivo de esta tesis es el desarrollo de métodos que a partir de imagen angiográfica permitan el análisis geométrico de las principales arterias cerebrales, en particular, la parte conocida como el Círculo de Willis (CW), que exhibe una gran variabilidad anatómica y que es una región donde predomina la aparición de patologías vasculares. Se ha hecho especial énfasis en que los métodos desarrollados estén automatizados para producir resultados objetivos (independiente del operador) y repetibles para minimizar la propagación de la variabilidad en el análisis posterior. El trabajo realizado se ha dividido en tres subobjetivos, cada uno de los cuales ha dado lugar a una contribución científica publicada o enviada a una revista con revisión externa.

En la primera contribución se ha mejorado un método de segmentación vascular para lograr robustez en la segmentación de imágenes procedentes de diferentes modalidades y centros clínicos, con una validación exhaustiva. Esta validación se ha realizado para imágenes de angiografía rotacional 3D y angiografía por resonancia magnética, las dos modalidades utilizadas para la caracterización propuesta. Una vez que el sistema vascular está correctamente segmentado, en la segunda contribución se ha propuesto una metodología para caracterizar ampliamente la geometría de la arteria carótida interna (ACI), que debido a su gran variabilidad geométrica ha sido de interés especial como un posible factor de riesgo de aparición o ruptura de aneurismas. Esto ha incluido el desarrollo de un método para identificar automáticamente la ACI a partir del árbol vascular segmentado. Finalmente, en la tercera contribución, esta identificación automática se ha generalizado a una colección de arterias incluyendo su conectividad y sus relaciones topológicas. Esto se ha presentado como un método para el etiquetado anatómico de los segmentos vasculares que forman el CW. Finalmente, la identificación de las arterias en un conjunto de individuos puede permitir la comparación geométrica de sus árboles arteriales utilizando la metodología introducida para la caracterización de la ACI. Así, estas tres contribuciones completan el objetivo considerado inicialmente.

1

General Introduction

1.1 Motivation and clinical context

The brain is an organ that is critically dependent on its blood supply. If this supply is disrupted, permanent damage to the affected area in the brain will occur, a condition known as *stroke*. A cerebrovascular disease (CeVD) is a dysfunction of the blood vessels supplying the brain that can lead to a stroke, and consequently to disability or death. In the western society, stroke is major cause of disability and the second leading cause of death, after heart disease and before cancer [1, 2]. Stroke appears in two forms: *ischemic* and *hemorrhagic*. Ischemic is the more common of the two, and is responsible for 80% of strokes. In contrast, hemorrhagic stroke has higher fatality rate.

Ischemic stroke is caused by low perfusion, which starves the brain tissue of oxygen carrying blood. It occurs mainly due to *thrombosis* or *embolism*. Thrombosis appears when thrombus (blood clot) forms inside the blood vessel reducing the lumen size to the point of blocking the blood flow. Embolism occurs as flow blockage by arterial embolus, debris originating from elsewhere in the body, most frequently from thrombus. Other, less frequent, causes of ischemic stroke are *systemic hypoperfusion* which produces a general decrease in blood supply and *venous thrombosis*, where locally increasing venous pressure exceeds the pressure generated by the arteries, preventing the blood reaching the brain. Atherosclerosis, a disease where the arteries harden and narrow, is principally responsible for creation of thrombuses and consequently ischemic stroke. It develops as a result of the accumulation of cholesterol, when multiple plaques start forming within the arterial wall. The plaque can then burst the wall and induce a formation of thrombus.

Intracerebral hemorrhage occurs when blood leaks into the brain. It is a serious medical condition since it can increase intracranial pressure. The spontaneous bleed normally results from rupture of abnormal blood vessels such as cerebral aneurysms. Cerebral aneurysms are pathological dilatations of the wall of arteries and their rupture are the principal cause of subarachnoid haemorrhage (SAH), an extensive bleeding onto brain surface with up to 50% fatality rate [3].

High blood pressure, smoking, drug abuse, cholesterol, inactivity, among other things, are affecting artery walls and are known risk factors for CeVD. Unfortunately, diseases like atherosclerosis and aneurysms progress slowly, mainly without symptoms, and cause the stroke to occur suddenly. Therefore, they are mostly found incidentally or after the stroke occurs, which is often too late. When identified, it is important to weigh the risk of treatment against the risk of the disease producing the stroke. Treatments involving surgery, or drugs, carry their risks and side-effects and a small risk of stroke can be found acceptable. However, the mechanisms leading to the formation and growth, and the stroke risk of atherosclerosis and aneurysms are still not fully understood.

1.1.1 The Circle of Willis

The brain is a highly vascularized organ due to its high blood flow rate and high oxygen demand, which consumes 15% of the blood output from the heart. The cerebral vasculature varies across individuals to such an extent that only a few of

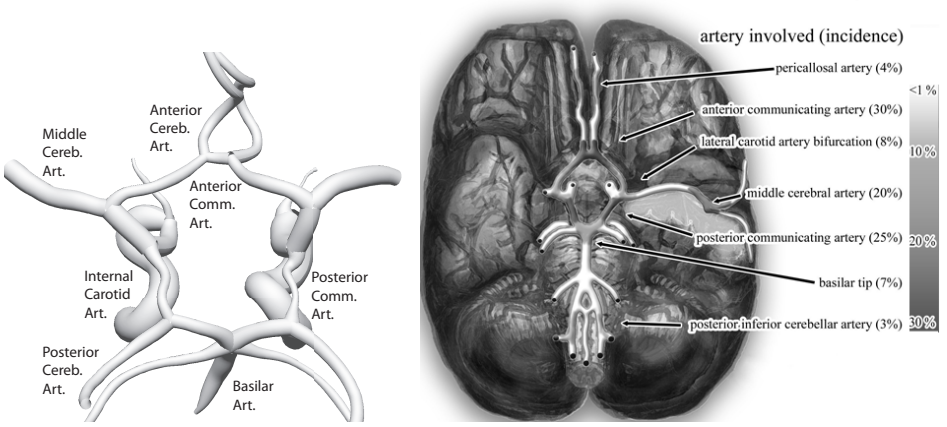

(a) **(b)**

Figure 1.1: The Circle of Willis: (a) Main arteries. (b) The most common sites of cerebral aneurysms (image by Nicholas Zaorsky, M.D.).

the largest vessels are consistent and have anatomical names. The main cerebral arteries are located at the base of the brain and are connected in a circle known as the Circle of Willis (CoW). The CoW is named after English neuroanatomists Thomas Willis (1621-1675) [4], who was the first to present the detailed description of this arterial circle and understand its importance.

The CoW conducts the blood flow supplied through the left and right carotid arteries, and the vertebral arteries to the brain [5]. It is the only region of the human body where the arteries form a circle, by design. As it connects the left and right anterior circulation with each other and with the posterior one, the circle serves as a source of collateral flow, and is very adaptable to any flow changes as a result of sudden artery occlusions. Thus, it has a crucial role in maintaining brain's blood supply.

The CoW is composed of the following arteries (Fig. 1.1(a)): Left and right anterior cerebral artery (ACA), anterior communicating artery (AcoA), left and right posterior cerebral artery (PCA), left and right posterior communicating artery (PcoA). The afferent internal carotid arteries (ICA) and the basilar artery (BA), as well as efferent middle cerebral arteries (MCA), are also commonly considered as part of the CoW.

A characteristic property of the CoW is that it exhibits a large anatomical variability, not only in geometry but also in topology where some vessels could be duplicated, hypoplastic or completely missing. In total, eighty-three variations in CoW have been denoted [6]. The standard, complete and symmetric CoW is estimated to be present in only $40-50\%$ of the healthy population [7,8]. Thus, not evey CoW is equally adaptable to potential vascular occlusions. Furthermore due to conducting blood flow at a high rate and its complex geometry, it is a common site of CeVD, in particular cerebral aneurysms tend to occur close to its artery bifurcations [9] (Fig. 1.1(b)).

1.1.2 Vascular geometry

Quantifying and analyzing the geometry of the cerebral arteries, in particular those forming CoW, is of great interest. There is still a lack of knowledge on the characteristic geometric parameters capable of differentiating between normal and pathologic vasculature or associated with endovascular treatment outcome. This can be also attributed to the difficulty in analyzing the complex and variable vascular geometry of the CoW. Thus, there is a clear need to develop tools and techniques for patient specific geometric characterization of the CoW, enabling personalized and predictive medicine [10, 11].

Geometric Risk Factors

The locations where vascular pathologies tend to occur are in general non-uniformly distributed across the vasculature. For example, cerebral aneurysms have strong preference for occurring at specific locations, and are frequently found at or near the regions of high vascular curvature in arteries of the CoW [9]. Similarly, atherosclerosis often occurs at carotid bifurcation or close to arterial bendings [12].

This phenomenon cannot be explained exclusively by risk factors such as hypertension, diabetes, smoking or gender, which are all systemic and influence the entire vasculature, hence not providing mechanisms for disease localization. Thus, it has long been speculated and recently confirmed that local hemodynamic forces (coming from blood motion), in particular the vascular *wall shear stress*, play an important role in the initiation and localization of pathologies [13–17], which in turn could explain their nonuniform distribution [18]. Furthermore, it is known that the variation in geometric configuration of vasculature contributes to a corresponding variation in predisposing hemodynamic forces [19, 20]. Taking this into account, Friedman et al. [21] introduced the concept of "geometric risk factors" as the geometric features that provoke high hemodynamic stresses on the vessel wall. As a result, a significant effort has been put by the biomedical research community to investigate the relationship between vascular geometry, hemodynamics and vascular diseases [12, 15, 22–30].

An important condition for the geometric risk factor concept is the presence of sufficient individual variability in geometry to induce important variations in individual hemodynamics [31]. This is particularly satisfied by the CoW, where the large anatomical variations affect the volume flow rates in the feeding arteries [32, 33], and the incidence of variations and asymmetry has already been found to be correlated with the presence of aneurysms [34].

Endovascular treatment

Treatment of stroke is increasingly performed using minimally invasive surgery known as endovascular intervention, as an alternative to open neurosurgery. It involves introduction of a catheter into the blood vessel and navigating inside the vascular network to the treatment location. There, appropriate endovascular devices like stents, or coils in the case of aneurysms, are deployed. Thus, accurate quantitative assessment of 3D arterial geometry is important for endovascular device selection, and preoperative planning of interventions [35, 36].

The operator's choice for the technique or device is already influenced by geometric and anatomical characteristics and there is a trend to apply specific type of devices to specific anatomy. A quantitative analysis of the geometry of the vessels will allow interventionalist to make more informed decisions in choosing access paths and selecting appropriate devices [37]. Stent deployment is especially sensitive to underlying geometry, and for effective treatment the dimensions of the device must match closely the vessel geometry, which led to define geometric parameters related to stent fitness [38, 39]. Another potential application is in personalized microcatheter shaping, for achieving safe entry and stability during coil placement [40–43]. Appropriately curved microcatheters better conform to the arterial anatomy and are more stable and hence less likely to be forced out of position during the treatment [44].

Other applications

There are a myriad of other applications that would benefit from studying the geometry of cerebral vasculature and that need methods for its description and quantification. Already cataloging vascular attributes like tortuosity, radii, branching frequency and curvature could answer many questions. How these attributes vary in a population and how they change with onset of a disease? What is their dependency across locations, and whether they follow a normal distribution [45]? Similarly how are they affected by aging [46] or what is the effect of exercise [47]? Are there any differences between gender, race and handedness [48]? Could some of the vascular attributes be associated to malignancy status of the tumor they supply [49, 50] and predict the treatment response [51, 52]?

Other interesting examples of geometric studies include investigating the processes and mechanisms of vascular patterning [53]. The major vessels are patterned by the genome but the branching of finer vessels is more stochastic. Understanding the role of genetics in vascular formation is also important due to possible relationships with some disorders. For instance an association has been found between Alzheimer's disease and abnormal vascular networks through a vascular endothelial growth factor (VEGF) expression [54, 55].

1.2 Geometric characterization of the vasculature

The important role of vascular geometry motivates the design of processing pipelines for the image-based, subject specific geometry characterization. The availability of quantitative measures would enable to study the association of local and global geometrical properties such as vessel curvature, tortuosity, length, radius, branching patterns, and the topology of the CoW with clinical events and therapy failure or to statistically analyze the variation of the CoW across a population or between the diseased and healthy subjects.

In general, the angiographic data is becoming readily available due to widespread use of 3D imaging devices, but there is still a lack of techniques for characterization of cerebrovascular geometry which can efficiently process the data. The characterization task is made difficult by two factors. First, by the large anatomical variability of cerebral vasculature, and with no direct correspondence

of blood vessels between subjects besides a few large ones [45]. Second, by the difficulty of designing methods that can obtain measurements from various types and quality of images in a robust, accurate and objective way [56, 57].

A successful geometric characterization pipeline would consist of the following elements:

- **Angiographic image acquisition**. Characterization of vascular geometry starts with angiographic image, acquired to obtain subject specific data.
- **Geometric modeling and anatomical labeling**. From the image, an accurate geometric model of subject's vascular network is extracted. In addition, individual, named vessels are identified to establish correspondence between subjects.
- **Characterization and statistical analysis**. Characterization consists of defining a set of meaningful geometric descriptors and a metric to measure (dis)similarity between geometric models. This is followed by the statistical analysis to estimate variability within a group of subjects or to discriminate between different groups, in an effort to derive the knowledge from the data or answer biological or medical questions.

The above elements of the pipeline are illustrated on the example of geometric characterization of internal carotid artery (ICA) (Fig. 1.2). Of special importance is that the elements are automated. This makes them operator-independent and highly repeatable to minimize variability propagation to other steps of the characterization pipeline. Furthermore, reducing the amount of manual interaction enables streamlining the geometric characterization of a large number of cases, hence increasing the power of the final statistical analysis.

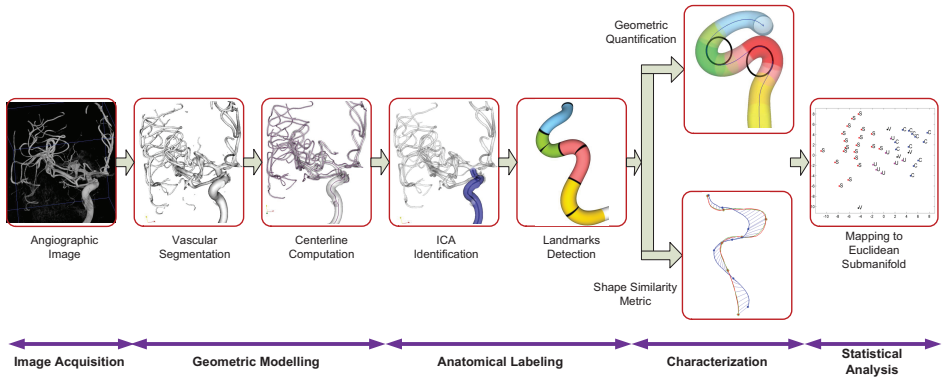

Figure 1.2: Pipeline for geometric characterization of internal carotid artery [58]. (See color insert)

1.2.1 Angiographic image acquisition

The 3D image acquisition of cerebral vasculature is nowadays routinely achieved with three different image modalities: X-ray 3D Rotational Angiography (3DRA),

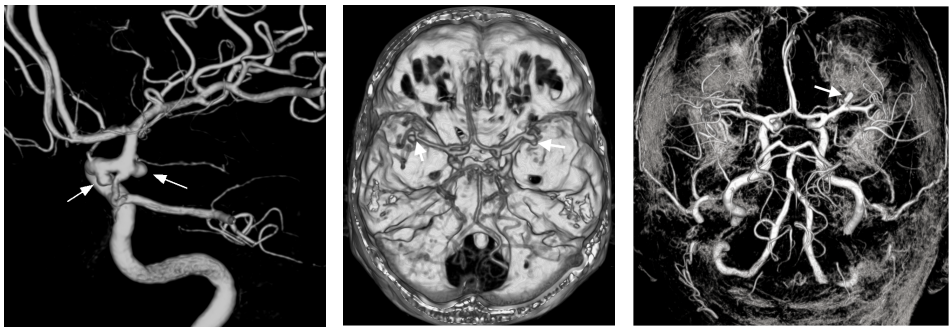

(a) 3DRA **(b)** CTA **(c)** Time-of-flight MRA

Figure 1.3: Images of the Circle of Willis of patients bearing aneurysms, from the three angiographic modalities. Aneurysms are denoted with white arrows. In 3DRA, acquisition of the right anterior part of the CoW was performed. CTA shows the skull bone as well.

Computed Tomography Angiography (CTA) and Magnetic Resonance Angiography (MRA). 3DRA imaging device is used during endovascular interventions and 3D reconstructions are normally done for treatment planning and later evaluating their success. It is considered an invasive procedure because of the requirement of catheter insertion into artery, which carries a small but significant risk of complication. Thus, for diagnosis and follow ups, preference is given to noninvasive computed tomography angiography (CTA) and magnetic resonance angiography (MRA) [9]. Examples of images acquired with the three modalities are shown in Fig. 1.3. In the following we briefly review and compare their main characteristics.

3D Rotational Angiography

3DRA performs an isotropic 3D reconstruction from multiple conventional 2D projection angiograms, obtained with C-arm X-ray imaging device. It is the most recent of the three angiographic modalities, made possible by the improvements in C-arm gantry movement and reconstruction algorithm speeds [59]. After catheter is positioned into carotid artery, iodinated contrast is injected into blood stream and acquisition started, which acquires $\approx$ 120 images, in a couple of seconds while rotating around 240^o. Compared to other modalities, it produces images with the highest spatial and contrast resolution. Contrast makes the vessels have high attenuating coefficient and consequently the brightest objects in the image. However there are several common image artifacts [60–62] due to inhomogeneous contrast distribution and beam hardening. In addition, there is no correspondence between an imaged tissue and a range of image intensity values, as the intensities are typically scaled to span the full dynamic quantization range. Thus, the tissue's intensity values depend on the selected reconstruction region, the contrast dose as well as the presence of other high attenuating objects, like coils, clips or stents, placed during treatment.

Computed Tomography Angiography

In CTA, contrast material is injected into a vein, and remains present in the vascular system for a duration of $20 - 30$ s. To acquire an entire head volume, a fast imaging is required to make acquisition during the maximal enhancement of the vessels, which was made possible with the introduction of spiral (helical) acquisitions with multirow detectors [63]. During the vessel enhancement period, acquisition is performed where the continuous rotation of the gantry is combined with simultaneous patients movement through the gantry. Compared to 3DRA, CTA is safer, less time-consuming and is more cost-effective. Furthermore, the obtained image intensities have standardized Hounsfield units (HU). On the downside, the contrast agent does not make vessels the highest intensity objects (nonenhanced: 30-45 HU, enhanced: 150-300 HU) as bones appear brighter with intensity ranging from 700 (spongy bone) to 3000 HU (dense bone). Combined with anisotropic and lower spatial resolution than 3DRA, this makes segmentation of vasculature challenging, especially for arteries passing next to cranial structures. Therefore, several approaches based on utilizing non-enhanced CT image, to subtract the bone tissue from CTA have been explored [64, 65].

Magnetic Resonance Angiography

MRA comprises of a group of techniques based on magnetic resonance imaging (MRI) to image blood vessels. The non-contrast MR angiography (NC-MRA) [66], relies on blood flow effects and the main two modalities used to image cerebral vasculature are: time-of-flight ToF-MRA, and phase-contrast PC-MRA. Compared to CTA and 3DRA, NC-MRA is the only acceptable modality for imaging healthy volunteers, as it does not involve ionizing radiation or contrast administration. However, acquisition speed and spatial resolution are lower and operating costs are higher. Furthermore images are susceptible to flow-related artifacts [67] and may have difficulties in visualizing small vessels with slow or turbulent flow [8].

In the contrast enhanced CE-MRA, the images are no longer dependent primarily on the inflow effect of the blood, which produces a better signal-to-noise ratio (SNR) and fewer artifacts. There, synchronizing the image acquisition with the arrival of the contrast agent is critical, which triggered the recent development of contrast agents that remain in the blood pool for several hours [68]. Longer time available for image acquisition enables higher resolution imaging, with the downside of having both arteries and veins enhanced at the same time. CE-MRA is not completely harmless as it does involve introduction of paramagnetic contrast agent but the contrast is less toxic and smaller quantities are needed than those used in CTA/3DRA. In general, MRA is under constant development, high magnetic fields (3T and 7T) devices [69] providing better SNR are becoming more available, and parallel imaging techniques [70, 71] are being improved to speed up acquisition or alternatively to increase the spatial resolution.

1.2.2 Geometric modeling and anatomical labeling

The task of geometric modeling is to extract the vasculature from angiographic image and to suitably represent it for its later characterization. Successful model-

ing the geometry of cerebral vasculature with pathologies is challenging. Cerebral blood vessels have a complex, tortuous anatomy with high variability of size and curvature. They often intertwine or run in closely parallel courses, and their geometry can be affected by calcifications, aneurysms, and stenoses.

Vessel lumen segmentation from angiographic image is the crucial step toward the accurate quantification of vasculature. Despite a big effort from the scientific community, as reviewed in [72, 73], it still remains a difficult task. Difficulty mainly arises from limited image contrast and spatial resolution, which are critical factors compared with the size of the vascular segments. Furthermore, acquisition devices produce image artifacts, have variable SNR and suffer from partial volume effects especially where the vessel is close to other vessels or skull bone. Thus, a segmentation process normally starts with a pre-filtering of angiographic image to further enhance vascular, elongated structures and suppress background and noise [74–77].

Vascular pathologies like stenoses and especially aneurysms exhibit high shape variability. Instead of modeling them explicitly, segmentation methods are made robust to pathologies, so that they can be detected afterwards as local deviations from the healthy vessel model [35, 78]. Geometric deformable models based on the level set framework [78–82] are especially suitable for this task, as they are able to handle changes of topology and adapt locally to the shape of complex structures. In addition, the vessel lumen, obtained from the propagating surface, is represented implicitly on the image grid by a distance map, hence allowing for subvoxel precision, of special interests when segmenting images with limited spatial resolutions.

Vasculature, being composed of tubular shapes, can be efficiently represented by a set of connected vessel centerline space curves. Therefore, after the segmentation, a *skeletonization* procedure is performed to obtain 4D points indicating the spatial position of each sequential vessel skeleton point and the associated local cross-section radius. Skeletonization methods are mainly based either on topological thinning, distance transformation or Voronoi diagrams [83]. In topology preserved thinning, the boundary is iteratively peeled until one-voxel thick medial curve is obtained [84]. Other approaches constrain centerlines to lie on paths maximally distant from the boundary [85,86], where the distance map can be replaced by Voronoi diagram of boundary points [87, 88]. As it is performed after the segmentation, potential segmentation errors are reflected on the obtained skeleton, which then requires further pruning to remove spurious components.

Instead of performing skeletonization after the vessel segmentation, an inverse approach is to attempt centerline extraction directly from the image, e.g. by tracking intensity ridges [89, 90]. The main problem with such methods is that they often require manual initialization and the obtained set of centerlines can be disconnected, which requires their later reconnection [91, 92]. However, the extracted centerlines can then be used to topologically and spatially constrain a subsequent segmentation of the lumen surface. Thus, segmentation and skeletonization are interdependent methods, and one facilitates and improves the computation of the other. Finally, geometric models are post-processed to compensate for some inaccuracies introduced during segmentation and skeletonization and to refine the data prior to later analysis [93].

For population analysis, it is important to be able to register and compare CoW across subjects. Thus, anatomical correspondence between vascular segments, known as *anatomical labeling*, has to be established [94]. This can be seen as a further segmentation of geometric model, where vascular segments with known anatomical names are identified.

1.2.3 Characterization and statistical analysis

We next review the main approaches used for the characterization and statistical analysis of geometry, relevant for the work developed in this thesis.

Geometric quantification

One characterization approach is to describe the geometry with a series of local or global features. The choice of features depends on the application and target hypothesis. The shape of a vessel centerline curve is already a rich source of geometric information. In particular its various tortuosity metrics are of special interest as a potential indicator of pathology development [45, 95–97]. In addition, centerline's local curvature and torsion describe 3D bending of the vessel and twisting of the curvature plane in space [57, 98] and are known to affect the underlying hemodynamic forces [19, 99]. They also enable computing several derived measures like curvature and torsion energy [100, 101], or axial twist [98]. Besides the centerline shape, local vessel diameters are related the blood flow capacity and often used measures are cross-section area, mean thickness, volume [102, 103], or radius tapper along the vessel [104]. When comparing with other vessels, they can detect hypoplasia and measure vascular thickness asymmetry [105, 106].

Apart from vessels, geometry of bifurcations and higher order branchings have been of interest as they are exposed to disturbed flow, making them a common site of pathologies [56]. First requirement is to locate the center of bifurcation and obtain its branch directions in an objective way [36, 56, 57, 104, 107, 108]. Then various branching features can be computed: The distribution of branching angles [108], the bifurcation planarity [57, 109] or expansion factor and asymmetry computed by comparing daughter branch cross-sectional areas with the parent one [110]. Further, statistically observing the vascular graph at a larger scale, branching frequency [45] and their patterns [111, 112] can be obtained.

Shape similarity metric

Each subject's set of geometric features can be considered as a single high-dimensional vector. This assumes that there is an anatomical correspondence established between subjects, so that the corresponding features are being compared. As different features span different range of values, it is not clear how to normalize them and weigh their contributions in the shape metric. One measure of shape similarity is to normalize features by their mean and standard deviation and then simply compute the Euclidean distance between the normalized feature vectors.

As an alternative, computational anatomy [113] emerged as a discipline focused on the quantitative analysis of variability of anatomical shape in a population.

There, individual subject shapes are modeled as transformations of a single template shape. In the absence of realistic physical deformation models, diffeomorphic transformations are used. This provides one-to-one and smooth transformations with smooth inverse, which assure topological consistency and avoid anatomically unrealistic folding artifacts [114]. This further led to the development of large deformation diffeomorphic metric mapping (LDDMM) framework [115, 116], by registering two shapes, this framework not only provides a diffeomorphic correspondence between them, but also defines a metric in the shape space as the length of geodesic curves matching one shape to another. In general, such deformations cannot account for non-diffeomorphic differences that might appear due to e.g. changes in topology nor for those that are below their regularizing spatial scale [117]. However, they can be used as a way to decompose the anatomical differences into two parts: geometric ones encoded in the deformation and the "texture" ones (e.g. topological or small scale differences) encoded in the residuals [118].

Statistical analysis

From a set of geometric features a sequence of univariate statistical tests can be performed to identify those that are statistically significantly different between two groups of subjects [12, 20]. The advantage is that the identified features provide direct interpretation of the difference. However, as more features are being compared, it becomes more likely that the two groups will appear to differ on at least one feature, which is known as *multiple comparison* problem. Thus, statistical significance threshold has to be adjusted appropriately [119].

To take into account the correlation between features, an alternative to a mass univariate testing is to consider all features together and then perform multivariate analysis (MVA). The MVA is then able to discover significant patterns which are distributed among features. There, the main limit is the *curse of dimensionality*, when few subjects are available compared to the high dimensionality of the feature space, and regularities could be found in the training set that are accidental. Thus, a form of dimensionality reduction is performed in a preprocessing step, most often based on principal component analysis or factor analysis.

The MVA consists of either generative or discriminative modeling [120]. In generative modeling, a probability density is estimated for each group, frequently assuming multivariate normal distribution. Then the classification of unknown instances can be performed by applying the Bayes theorem. Instead of using a generative model and modeling within class variance, it is possible to directly estimate the separation between the groups using a discriminative model, which in many practical situations gives better classification results [121]. The most successful example of non-linear discriminative models are support vector machines (SVM) [122]. They work by projecting the data into a high number of dimensions, where they can be better separated using a linear hyperplane. Taking the hyperplane which maximizes the margin confronts the problem of high dimensionality. Both generative and discriminative models rely on having a notion of similarity between shapes. Besides using simple Euclidean distance between feature vectors, the shape distance measure can come from other frameworks like LDDMM.

Unlike mass-univariate approaches, multivariate techniques are global and not localized to discrete regions. Thus, interpreting the findings is more complex. Here, generative models have advantage that we can sample the learned distribution from the mean along the principal directions of variation to visualize the main captured variability within a group. For discriminative models, when linear classifiers were used, one could also sample along the principal discriminative direction to observe the shape changes from one population to the other [123]. However, visualizing the shape differences in the case of non-linear discriminative models is more complex [124], hence they are more appropriate for evaluating how well the model can separate between classes.

1.3 Objectives of the thesis

The main objective of the thesis is to design, develop and implement an automated methodology for image-based geometric analysis of the major cerebral vasculature, in particular of the arteries forming the CoW. The path to the goal is subdivided by proposing solutions for the three tasks:

- Vascular segmentation of images coming from different modalities and clinical centers.
- Anatomical labeling of the arteries forming the CoW.
- Geometric characterization of individual vessels.

1.4 Overview and contributions of the thesis

The proposed solutions to each of the three subgoals are presented in the next three chapters. They provide the main contributions of the thesis.

Chapter 2 describes the improvement of an automated vascular segmentation method based on geodesic active regions (GAR) to achieve robustness in segmenting images coming from different imaging modalities and clinical centers. This is accomplished by introducing an image intensity standardization filter, designed to ensure a correspondence between specific tissues and intensity ranges common to every image that undergoes the standardization process. The improved GAR segmentation was then exhaustively validated on images from patients containing cerebral aneurysms in the area of the CoW from 3DRA and ToF-MRA images, the two modalities used in the later geometric characterization.

In **Chapter 3**, we propose a methodology to extensively characterize the geometry of the ICA, which due to its large geometric variability has been of interest as a potential risk factor for the onset or rupture of aneurysms. Here, we develop a method for detecting anatomical landmarks of the part known as carotid siphon by modeling it as a sequence of four bends and selecting their centers and interfaces between them as landmarks. The bends are detected from the trajectory of the curvature vector expressed in the parallel transport frame of the centerline curve. Using the detected landmarks, we characterize the geometry in two complementary ways. First, with a set of local and global geometric features, known

to affect underlying hemodynamics. Second, using LDDMM to quantify pairwise shape similarity. In addition, we develop a method to automatically identify the ICA from segmented vascular tree.

In **Chapter 4**, we generalize the automated identification of ICA from a single to a collection of vessels in a method for anatomical labeling of the vascular segments forming the entire CoW. The proposed method is trained on a set of pre-labeled examples, where it learns the variability of local bifurcation features as well as the variability in the structure. Then, the labeling of the target vasculature is formulated as maximum a posteriori probability (MAP) estimate, where the likelihood of labeling individual bifurcations is regularized by the prior structural knowledge of the graph they span. Furthermore, the introduced method is applicable to graphs with a cycle and multiple roots, which is a special requirement for labeling CoW.

Each of these three chapters are self-contained, and are an adaptation of the articles that were submitted or published in a peer-reviewed journals. Thus, some of the elements from the introduction will be repeated. Finally, **Chapter 5** concludes the thesis and discusses the outlook and future work.

2

Automated Segmentation of Cerebral Vasculature using Geodesic Active Regions: an Evaluation Study

This chapter presents evaluation of an improved version of an automated segmentation method based on geodesic active regions (GAR) for segmenting cerebral vasculature with aneurysms from 3DRA and ToF-MRA images available in the clinical routine. Three aspects of the GAR method have been improved: execution time, robustness to variability in imaging protocols and robustness to variability in image spatial resolutions. The improved GAR was retrospectively evaluated on images from patients containing cerebral aneurysms in the area of the Circle of Willis and imaged with two modalities: 3DRA and ToF-MRA. Images were obtained from two clinical centers, each using different imaging equipment. Evaluation included qualitative and quantitative analyses of the segmentation results on 20 images from 10 patients. The gold standard was built from cross-sections of vessels and aneurysms, manually measured by interventional neuroradiologists. GAR has also been compared to iso-intensity surface extraction. In addition, since patients had been imaged with two modalities, we performed an inter-modality agreement analysis with respect to both the manual measurements and each of the two segmentation methods. Both GAR and ISE differed from the gold standard within acceptable limits compared to the imaging resolution. The repeatability of GAR was superior to manual measurements and ISE, while the inter-modality agreement was similar between GAR and the manual measurements.

The content of this chapter is adapted from the following publication:

H. Bogunović, J.M. Pozo, M.C. Villa-Uriol, C.B.L.M. Majoie, R. van den Berg, H.A.F. Gratama van Andel, J.M. Macho, J. Blasco, L. San Román, and A.F. Frangi. Automated segmentation of cerebral vasculature with aneurysms in 3DRA and ToF-MRA using geodesic active regions: an evaluation study. *Medical Physics*, 38(1): 210-222, 2011.

2.1 Introduction

Cerebral aneurysm is a vascular pathology that tends to appear near bifurcations of arteries in the Circle of Willis. Although aneurysm prevalence is relatively low, estimated to be between 1% - 5% [9], aneurysm rupture causes sub-arachnoid haemorrhage (SAH) having a high fatality rate (between 40% and 60%) [125]. Traditionally, for aneurysm detection, catheter 2D digital subtraction angiography (DSA) was considered as gold standard [125] but lately it is being supplemented or replaced by 3D rotational X-ray angiography (3DRA) [126]. Due to its superior spatial and contrast resolution, 3DRA is normally also used for treatment planning (surgical clipping or endovascular intervention). However, for diagnosis and follow ups, preference is given to noninvasive computed tomography angiography (CTA) and magnetic resonance angiography (MRA): contrast enhanced CE-MRA and time-of-flight ToF-MRA [127].

Ruptured aneurysms are almost always treated. However, in the case of unruptured aneurysms, the indication for preventive treatment is not straightforward and the risk of treatment has to be carefully balanced against the risk of rupture. Computational modeling is increasingly used to characterize the aneurysms in order to find suitable predictors of risk of rupture [10]. Most notably, aneurysm shape characterization [128, 129] and analysis of its hemodynamic features using computational fluid dynamics (CFD) [14, 130] are becoming increasingly important. These results are strongly determined by the modeled geometry of the aneurysms and surrounding vessels. Therefore, vascular segmentation from radiographic images is a key methodology in the computational analysis of the vasculature.

The segmentation of cerebral vasculature with aneurysms is a difficult task often due to their complex geometry as well as limited image contrast and spatial resolution, which are critical factors compared with the size of these vascular segments. Throughout their management cycle, patients undergo a variety of imaging examinations with various modalities. In addition, patients with ruptured aneurysms have 3DRA and CTA scans while patients with unruptured ones are preferably followed only with MRA. Thus, it is desirable to apply a cerebrovascular segmentation method able to cope coherently with different imaging modalities so that computational results are comparable. Furthermore, it is important that the applied segmentation method is completely automated. This has a two-fold advantage. First, the segmentation method should be objective (operator-independent) and highly repeatable to minimize variability propagation to other steps of the analysis pipeline. Second, requiring manual interaction from the operator increases the processing time and needs the allocation of human resources.

To the best of our knowledge no effective solution is currently available for the automated and multimodal segmentation of cerebral vasculature with aneurysms. Recently, Manniesing et al. [131] reported a successful feasibility study for the automated segmentation of CTA images but their evaluation did not cover aneurysms, thus it is not clear how their results would extrapolate to diseased parts of the vasculature. Hernandez et al. [78] proposed a method based on a geometric deformable model called geodesic active regions (GAR) and presented promising results for automated segmentation of cerebral aneurysm from different modalities

(3DRA and CTA). However, limiting factors for its application in clinical routine was its lack of robustness to the variation in imaging protocols and its elevated computational costs.

The purpose of this study was to introduce improvements into the GAR method and to evaluate its potential and limitations in segmenting cerebral vasculature with aneurysms from 3DRA and ToF-MRA images available in the clinical routine, including different clinical centers and imaging equipment. The evaluation was performed retrospectively on images of patients having cerebral aneurysms. The segmentation results were compared to the gold standard obtained from manual measurements performed by interventional neuroradiologists. To analyze the segmentation consistency across the two imaging modalities, patients having both 3DRA and ToF-MRA examinations were chosen.

2.2 Materials and methods

2.2.1 Patient selection

Ten patients (3 male, 7 female; age range: 35-70; mean age: 57 years) with 16 cerebral aneurysms scanned with 3DRA and ToF-MRA within a short period (1 week) were retrospectively selected from two different clinical centers (7 from Academic Medical Center (AMC), The Netherlands and 3 from Hospital Clinic i Provincial de Barcelona (HCPB), Spain). Each center used different imaging equipment. Anonymized imaging data sets were used and the institutional review board approved the study, which had no influence on patient management. From the database of suitable candidates, patients were selected on the basis of the location of aneurysm to ensure that location variability followed their natural probabilities of occurrence as reported in [9]. For patients having multiple aneurysms only those present in both 3DRA and MRA images were eligible. Eventually, one aneurysm per patient was singled out. The different locations were: internal carotid artery (3), posterior communicating artery (2), anterior communicating artery (1), middle cerebral artery (3) and basilar tip (1). Aneurysms varied in size: small aneurysm of 3-5 mm (5), medium aneurysm of 8-9 mm (4) and a large aneurysm of 19 mm (1).

2.2.2 Scanning protocols

3DRA images from AMC (*HCPB, respectively*) were acquired with a single-plane angiographic unit: Integris Allura Neuro; Philips Healthcare, Best, The Netherlands (*AXIOM Artis; Siemens Medical Solutions, Erlangen, Germany*). Non-ionic contrast agent: 320 mgI/mL iodixanol, Visipaque (240 *mgI/mL iohexol, Omnipaque*), GE Healthcare, Cork, Ireland, was injected through a 6F catheter positioned in an internal carotid artery or vertebral artery. 100 images (120 *images*) were acquired during a 240^o (180^o) rotational run in 8 seconds with 15 to 21 ml contrast agent at 3 ml/s. On a dedicated workstation, 3D images were reconstructed with a 256^3 matrix with a reconstructed voxel size of $0.19 \times 0.19 \times 0.19$ mm ($0.39 \times 0.39 \times 0.39$ *mm*).

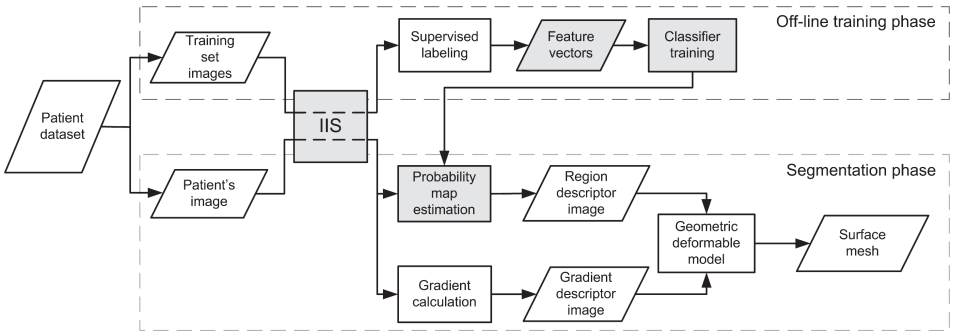

Figure 2.1: Workflow of the automated vascular segmentation method GAR. New or improved components are highlighted in gray.

MR imaging examinations in AMC (*HCPB, respectively*) were performed on a 3.0-Tesla system: Intera R10; Philips Healthcare, Best, The Netherlands (*TrioTim; Siemens Medical Solutions, Erlangen, Germany*). The protocol included 3D ToF-MRA with multiple overlapping thin slab acquisition MOTSA (*with single slab acquisition*). The parameters were as follows: TR/TE, 21/4 ms (23/4 *ms*); flip angle, 20^o (15^o); 512×326 (640×288) acquisition matrix, reconstructed to 1024×1024 (640×480); FOV, 200×170 mm (200×150 *mm*), 85% (75%) rectangular FOV; 1.0 mm thick sections interpolated to 0.5 mm (0.5 *mm thick sections*); 220 sections (160 *sections*) acquired, resulting in a coverage area of 110 mm (80 *mm*). The measured voxel size was $0.39 \times 0.61 \times 1$ mm ($0.31 \times 0.52 \times 0.5$ *mm*), and the reconstructed voxel size was $0.2 \times 0.2 \times 0.5$ mm ($0.31 \times 0.31 \times 0.5$ *mm*). The scanning time was reduced with sensitivity encoding SENSE parallel imaging (*generalized autocalibrating partially parallel acquisition GRAPPA*), with a reduction factor of 1.5 (2), which resulted in an acquisition time of 7 min (4.5 *min*).

2.2.3 Segmentation method

The workflow of the automated vascular segmentation method GAR is shown in Fig. 2.1. The core of the methodology was originally presented in [78], and in [132] the image intensity standardization (IIS) filter was introduced. In this work, we improve some of the components of the workflow, but we first summarize the methodology that has remained unchanged.

The method is based on the geometric deformable model within the level set framework [133]. The internal force of the deformable model is defined as the local curvature of the evolving surface, while the external one combines region-based descriptors with gradient ones to drive the evolution of the model towards the vascular boundaries. The equation driving the evolution of the surface is expressed as:

$$\frac{\partial}{\partial t}\Phi + \zeta(k_{out} - k_{in}) \mid \nabla\Phi \mid -\eta(\varepsilon g K_m \mid \nabla\Phi \mid + \nabla g \cdot \nabla\Phi) = 0 \qquad (2.1)$$

where Φ is an implicit function whose zero level set at any time t of the evolution represents the vascular surface. The gradient descriptor g is inversely proportional

to the gradient magnitude of the image and helps stopping the evolution at the vessel boundary. The descriptor K_m is the minimal curvature of the level set surface at each point, which favors the smoothness of the surface. The region descriptors k_{in} and k_{out} are defined by

$$k_{in}(\mathbf{x}) = -\log(P_{in}(\mathbf{x})); k_{out}(\mathbf{x}) = -\log(P_{out}(\mathbf{x})) \tag{2.2}$$

where P_{in} and P_{out} are the probabilities that the voxel $\mathbf{x}$ belongs to inner and outer regions with respect to the vascular lumen. The constant parameters ε, ζ and η control the influence of the curvature, region-based and gradient-based descriptors, respectively, and were fixed as published in [78].

In general, the GAR workflow is divided into two main phases: off-line training and segmentation.

Off-line training phase. Performed only once for each imaging modality. Images forming the training set are passed through IIS filter and interactively labeled into three regions: vessel, background and undecided region, which normally corresponds to partial volume voxels. Then, the feature vectors are calculated at training points randomly selected from vessel and background regions. Finally, the fuzzy classifier is trained in a supervised fashion on the set of feature vectors. The output is a set of parameters of the classifier used to compute the probabilities P_{in} and P_{out} during the segmentation phase.

Segmentation phase The image being segmented is first passed through the IIS filter. At each image voxel, the feature vector is calculated and the probability of belonging to a particular region is estimated with the previously trained classifier. In parallel, the gradient magnitude is computed. Following Eq. 2.1, the level sets associated with Φ evolve toward a local minimum of the energy functional trying to maximize the probability for the vessel region inside the zero level set and the probability for the background region outside, taking also into account the curvature and the gradient information at the boundaries. The zero level set at the steady solution corresponds to the segmented vessel lumen surface. The resulting surface is extracted as a 3D triangular mesh with sub-voxel precision.

Such methodology is specially suitable for vessel segmentation from different modalities, since for each one the region descriptors are learned from an appropriate training set of images.

In this work, we have introduced the following three improvements to the components of the workflow: The classifier has been replaced, the computation of the feature vector has been modified and the IIS technique has been adapted to handle large deformations.

Multiple valued neuron classifier

The originally proposed probability estimation was performed using k nearest neighbors (k-NN) algorithm on the training set. However k-NN is not convenient for fuzzy classification and is highly computationally demanding since during the classification it repeatedly searches for the nearest neighbors within the stored

training feature vectors. Thus, we replaced it with the multiple valued neuron (MVN) [134]. This improves the classification speed by approximately 8 times since most of the computational cost is in the training phase, which is performed only once. Furthermore, larger sets of points (1M as opposed to 20k used with k-NN) were used for training as their size does not influence the classification speed of MVN. Using more points allowed building a training set with larger number of images thus achieving better classifier generalization.

Voxel-based scale space

Features forming the feature vector are computed on multiple scales. To handle a large variety of possible image resolutions, the range of scales used for feature calculations is now based on image voxel spacing instead of being predefined and fixed. More details on how features are calculated are given in Appendix.

Image intensity standardization (IIS)

To get good estimates of the probability map, the images composing the training set should describe well the image to be segmented. In MRA and 3DRA, the intensities do not have a direct physical interpretation and the intensity range for the same tissues can largely vary between images. The IIS [135] ensures that the intensity ranges corresponding to the same tissues are similar by establishing a correspondence between histograms taken from generic images and a histogram taken as a reference. The image histogram is aligned to the reference using a 1D non-linear registration technique. The generated intensity transformation is applied to the image volume, standardizing the intensity ranges. This enables the use of the same training set for any image of the same modality [132]. In this study, we improved the registration technique to make it robust to large deformations and applicable to both 3DRA and MRA images. Normalized cross-correlation is used as a similarity metric and the deformation is parameterized by cubic B-spline. Limited memory Broyden Fletcher Goldfarb Shannon with simple bounds (LBFGSB) algorithm [136] is used as optimizer. The registration is first initialized with a transformation composed of two control points aligning the histogram peaks and the largest intensity values. The registration is then performed following a multiscale approach: in three chained iterations, progressively incrementing the number of control points (4, 5 and 6), resetting their position equidistantly at the beginning of each iteration. The range of movement is limited to half the inter-control points distance [137]. This results in a diffeomorphic transformation since it is smooth and avoids folding. Although there is a constraint on the overall deformation, allowing further stretching or compression was not found necessary and it prevents instabilities. The IIS was able to align the histograms in both the 3DRA and MRA images of the patients (Fig. 2.2).

2.2.4 Segmentation evaluation method

One aneurysm and three surrounding vessels of clinical interest, both proximal and distal from the aneurysm (blood flow inlets and outlets) were selected per patient. The selected vessels and aneurysm had to be visible in both 3DRA and MRA

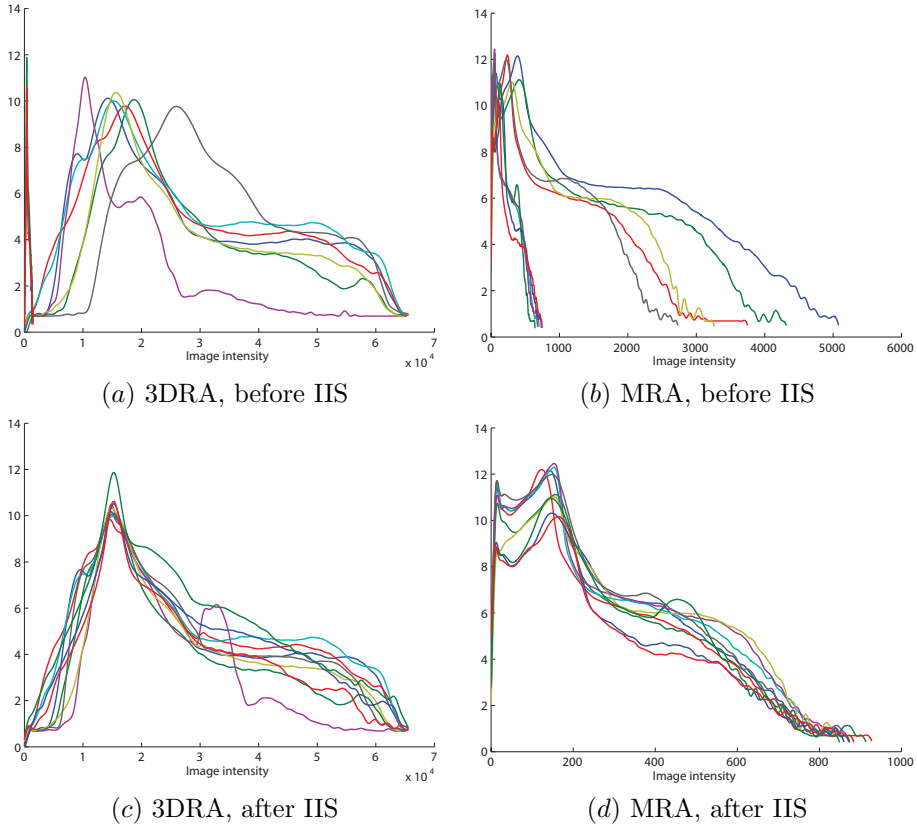

(*a*) 3DRA, before IIS (*b*) MRA, before IIS

(*c*) 3DRA, after IIS (*d*) MRA, after IIS

Figure 2.2: Image histograms of the 10 patients before (a, b) and after (c, d) image intensity standardization of 3DRA (a, c) and MRA (b, d) images. The logarithm of histogram values is displayed. (See color insert)

scans of the patient. On every image, for each selected vessel 10 cutting planes were automatically positioned 1 mm apart and orthogonal to the vessel centerline. Three additional cutting planes were manually positioned on the aneurysm, one cutting the neck and the other two passing through the center of the neck and the maximum aneurysm depth. This yields 33 cutting planes per image (660 in total). Once defined, the cutting planes were kept fixed throughout the evaluation study. The positions of the cutting planes were chosen to representatively sample the geometry of interest around aneurysm. Having a good segmentation of that region is important for subsequent computational modeling approaches.

The cutting planes applied to 3D intensity image produce 2D images with the vessel cross-section, where the manual measurements were performed. The same cutting planes applied to segmented surface mesh produce 2D contours, on which the same measurements were automatically extracted. Since the cutting planes were fixed, all the measurements were taken on the same cross-sections. Two measurements per cross-section were performed. Their definition together with the positioning of the cutting planes and examples of measurements of the

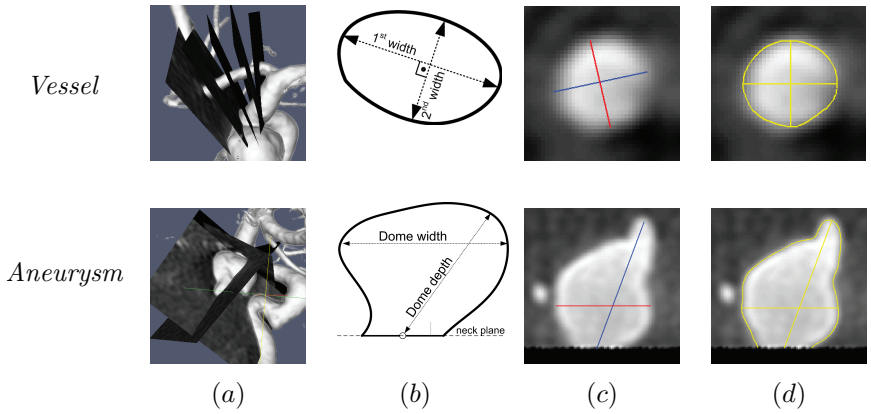

Figure 2.3: (a) Positioning of cutting planes. (b) For measuring vessels and aneurysm neck the two measuring segments need to be orthogonal to each other (1^{st} width is chosen first) and located where the width is maximum. Dome depth is the distance from the neck center to the farthest point on the dome, while dome width is the length of the longest chord of the dome parallel to the neck plane. (c) Example of manual measurements. (d) Example of automated measurements. (See color insert)

cross-sections are shown in Fig. 2.3.

The shape of the vessel and aneurysm neck cross-section was assumed to be round but not necessarily circular. We proposed to describe the shape by the two orthogonal widths, which capture its major and minor axes and reduce the ambiguity when performing the manual measurements. Measurements of the dome are relative to the neck plane and its center. For each aneurysm neck cross-section, its center was computed. Thus, all the parameters of the neck were fixed and did not introduce variability into the measurements of the dome.

To build the gold standard, manual measurements performed by 5 interventional neuroradiologists from two clinical centers in 2 sessions were averaged. The measuring guidelines were easily followed by the clinicians performing the manual measurements. We also compared the GAR to another segmentation method: interactive contouring based on iso-intensity surface extraction (ISE). The iso-intensity surface is the interface between the regions of the image I: $I \geq c$ (the inside) and $I < c$ (the outside), where c is a constant intensity value. The surface is obtained by marching cubes method [138] where the points at which the iso-intensity surface intersects the edges of the voxel cube are obtained by linear interpolation, producing a triangular mesh with sub-voxel accuracy. Four expert users, with more than 3 years of angiographic experience, performed ISE segmentation in 2 independent sessions.

In order to evaluate the inter-modality agreement, a correspondence between cutting planes in both imaging modalities was established for each patient. Cutting planes on vessels were manually aligned, starting the cutting sequence at the same anatomical position in both imaging modalities. To establish corresponding aneurysm cutting planes, the 3DRA and MRA segmented surface models were first rigidly registered. Then the cutting planes that were manually positioned in 3DRA were transferred to their corresponding locations in MRA.

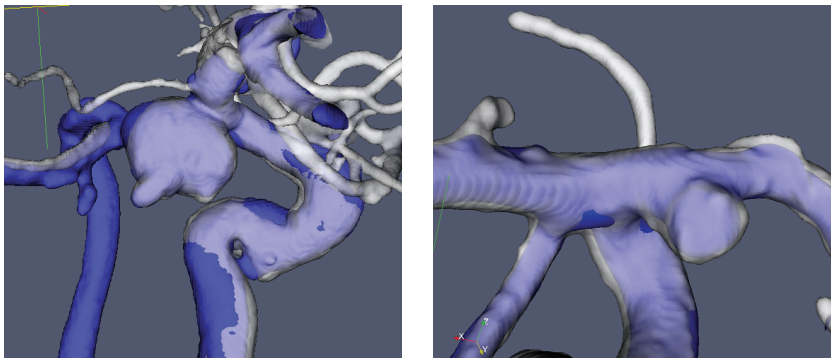

(a) (b)

Figure 2.4: Examples of the registered surfaces from the two modalities 3DRA (in white) and MRA (in blue). (See color insert)

The rigid registration was performed in a supervised fashion. First, corresponding pairs of points on the two meshes were identified and an initial transformation was applied to approximately align them. Next, the registration was refined using the Iterative Closest Point algorithm [139]. This was repeated until the two meshes were adequately registered after visual inspection (Fig. 2.4). To evaluate the repeatability of such procedure, the registration was performed three times for each pair of meshes.

Qualitative analysis

The segmentation results were qualitatively evaluated by visual inspection of the cross-sections obtained from the segmentation results. The cutting planes where the segmented contours were missing, unrealistically deformed or merged with neighboring vessels, were classified as erroneous. Their occurrence rate and the effects causing them were analyzed. However, they were excluded from the subsequent quantitative analysis, since they would otherwise introduce large errors, which are not representative of the segmentation performance in denoting the actual border of the vessel lumen.

Quantitative analysis

For the quantitative analysis, three main factors, as proposed by [140], were considered: repeatability, accuracy and efficiency. In addition, we also evaluated the global correctness by region overlap with manual segmentations and the inter-modality reproducibility.

Repeatability The main variability of GAR results is introduced by the differences between the images used as a training set for the classifier. This variability was estimated from results obtained with different training sets. In addition, we evaluated the influence that the number of images in the training set has on the variability. The variability of manual measurements

and ISE results is introduced by the observer, thus we estimated their inter- and intra-observer variability.

Accuracy For GAR and ISE methods it was estimated in two complementary ways. First, as an average absolute difference from the gold standard. Second, as limits of agreement with the gold standard, which represent the bias and the 95% likely range for the differences. From this, a variability index was introduced where deviations from the gold standard are put into perspective by comparing them to the variability of manual measurements.

Region overlap To complement the accuracy measurements, the segmentation results were converted from mesh to voxel representations and compared to manual segmentations performed on the geometry of interest by two experienced observers. Although less sensitive to small, sub-voxel variations, this more global metric can detect serious mis-segmentations of the vessel region. Two region overlap measures, as used in the recent works [141, 142], were calculated: the Dice [143] and the conformity [144] scores.

Efficiency Estimated as average time spent in segmenting an image. For automated GAR method, it was the computer execution time, while for interactive ISE, was the time spent by the observer deciding on the optimal iso-intensity value.

Inter-modality reproducibility Estimated for manual measurements and the two segmentation methods as limits of agreement between the corresponding values on the results from the two modalities.

As the evaluation is based on limits of agreement, variability index and region overlap scores, we summarize their calculation details.

Limits of Agreement (LoA). In order to analyze the LoA between each segmentation method and the gold standard in a repeated study (multiple sessions), a two-way analysis of variance (ANOVA) with a statistical linear mixed model was used [145]. To obtain the standard deviation of the method with respect to the ideal gold standard (having zero variability), the variability of the gold standard σ_{gs} was removed from the standard deviation of LoA (σ_{loa}).

$$\sigma_{\widehat{\text{loa}}} = \sqrt{\sigma_{\text{loa}}^2 - \sigma_{\text{gs}}^2}. \tag{2.3}$$

Variability index. To compare the deviation of segmentation results from the gold standard, with the variability of manual measurements, we defined the variability index (similar to the Williams index [146]) as the ratio of the method's standard deviation and the inter-observer variability of the manual measurements:

$$I = \frac{\sigma_{\widehat{\text{loa}}}}{\sigma_{\text{inter-clinician}}} \tag{2.4}$$

If the value of this index $I < 1$, the segmentation method deviates from the gold standard less than the manual measurements vary between themselves.

Region overlap scores. The Dice and the conformity scores are defined as follows:

$$\text{Dice} = 2\frac{|S_{\text{method}} \cap S_{\text{gs}}|}{|S_{\text{method}}| + |S_{\text{gs}}|} \times 100\%; \tag{2.5}$$

$$\text{Conformity} = \left(1 - \frac{|S_{\text{FP}}| + |S_{\text{FN}}|}{|S_{\text{TP}}|}\right) \times 100\%, \tag{2.6}$$

where S_{method} and S_{gs} are the sets of vessel region voxels labeled by the segmentation method and the gold standard, respectively. S_{FP}, S_{FN} and S_{TP} are the sets of false positives, false negatives and true positive voxels, respectively, with respect to the gold standard. $|X|$ denotes the cardinality of the set X. Both scores reach the value of 100% in the case of perfect overlap and are mutually related by

$$\text{Conformity} = 3 - \frac{2}{\text{Dice}}. \tag{2.7}$$

2.3 Results

Results are grouped according to the region of interest (aneurysms or vessels) and according to the imaging modality (3DRA or MRA). The two widths used as descriptors of vessel and aneurysm cross-sections were evaluated together. For reporting statistical significance, two-tailed 95% confidence intervals were considered.

2.3.1 Qualitative analysis

The following effects were causing erroneous segmentations in certain cutting planes:

Touching vessel effect Two vessels are merged and the 1$^{\text{st}}$ width is the sum of both vessel diameters. It occurred mostly in 3DRA images where small vessels can appear very close or touching. In ToF-MRA images, due to the low spatial resolution and the low blood flow in small vessels, these vessels are usually not visible in the images.

Missing vessel effect The cutting plane contains no segmentation contour. It happened mostly in ToF-MRA images due to the low signal in a vessel.

Wide aneurysm neck The aneurysm dome is merged with the surrounding vasculature. Hence, the neck is largely oversegmented.

Indented aneurysm Aneurysm neck and dome become severely undersegmented (shape is deformed) due to the low signal in the image. It happened only in ToF-MRA images, where the low signal is caused by flow induced artifacts (e.g. turbulent flow).

Table 2.1: Percentage of excluded cutting planes due to the occurrence of qualitative segmentation errors. Per modality there were: 300 planes positioned on vessels (10 patients, 30 planes each), and 30 planes positioned on aneurysms (10 patients, 1 plane positioned on the neck and 2 on the dome).

Effect	*Occurrence rate [%]*			
	GAR		ISE	
	3DRA	MRA	3DRA	MRA
Touching vessel effect	8.7 (26/300)	0.3 (1/300)	16 (48/300)	5.7 (17/300)
Missing vessel effect	0 (0/300)	2 (6/300)	0.3 (1/300)	2 (6/300)
Wide aneurysm neck	40 (4/10)	20 (2/10)	30 (3/10)	30 (3/10)
Indented aneurysm	0 (0/30)	17 (5/30)	0 (0/30)	10 (3/30)

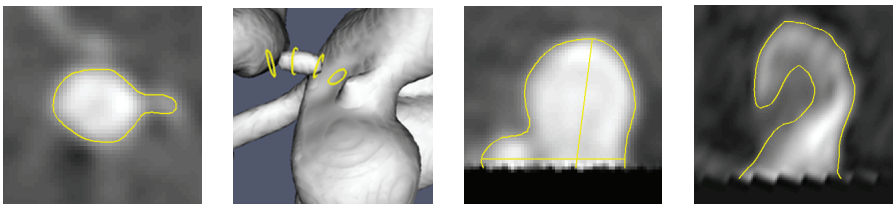

(*a*) (*b*) (*c*) (*d*)

Figure 2.5: Examples of qualitative errors: Touching vessel effect (a), missing vessel effect (b), wide aneurysm neck (c) and indented aneurysm (d). (See color insert)

Examples of the above-mentioned effects are shown in Fig. 2.5. The percentage of occurrence for each specific modality and segmentation method is shown in Table 2.1.

The occurrence rate of touching vessels in GAR was half of the value in ISE for 3DRA images (close to being statistically significant, $p = 0.06$, binomial-test) and significantly smaller than in ISE for MRA images ($p = 0.01$, binomial-test). The missing vessel effect was rare for both segmentation methods. In contrast, the problems at the aneurysm were equally frequent for both GAR and ISE ($p > 0.8$, binomial-test). The aneurysm neck is especially susceptible to qualitative errors since in many cases it is hard to approximate a neck using a 2D plane.

2.3.2 Quantitative analysis

Repeatability

The variability of the GAR segmentation results is mainly due to the training set and depends on the number of images used to produce it. This variability is expected to decrease as the size of the training set increases, because the variability introduced by manually segmenting each image is canceled out when averaging more images. To evaluate the repeatability of GAR, the segmentation of the 10 3DRA images was repeated with 16 different training sets: 4 sizes were selected to build the training set (number of images: 3, 6, 8 and 10) and, for each size, 4

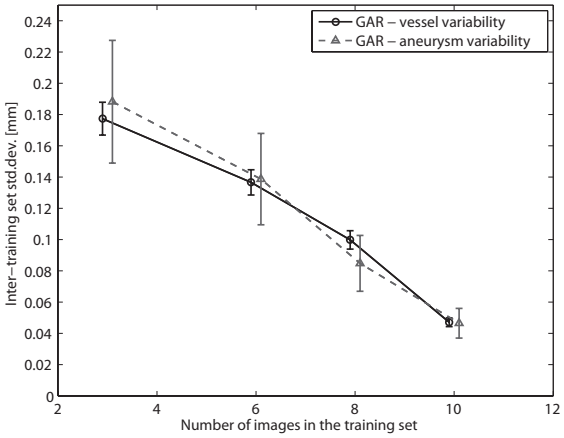

Figure 2.6: Inter-training set variability (from 4 different training sets) of GAR in 3DRA in relation to the number of images (3, 6, 8 and 10) used to build the training sets. Error bars present the 95% confidence intervals.

Table 2.2: Standard deviations (SD) of variability (two-way ANOVA) with their 95% confidence interval (CI), for manual measurements and ISE segmentation method.

	Method	*SD ± 95% CI [mm]*			
		Vessel		Aneurysm	
		3DRA	MRA	3DRA	MRA
Inter-observer	Manual	0.27 ± 0.02	0.30 ± 0.02	0.30 ± 0.05	0.29 ± 0.05
	ISE	0.18 ± 0.01	0.22 ± 0.01	0.15 ± 0.03	0.24 ± 0.05
Intra-observer	Manual	0.17 ± 0.01	0.18 ± 0.01	0.26 ± 0.05	0.20 ± 0.04
	ISE	0.14 ± 0.01	0.16 ± 0.01	0.11 ± 0.02	0.20 ± 0.04

independent (non-overlapping) sets of images were used. For training sets having 10 images, the inter-training set variability was less than 0.05 mm for the vessel and aneurysm regions (Fig. 2.6).

The operator-induced variability values for manual measurements and ISE segmentation method are presented in Table 2.2. The variability of the GAR method was clearly lower than even the intra-observer variability of the ISE and the manual measurements. The rest of the presented GAR results on 3DRA correspond to those made with 4 different training sets composed from 10 images each.

Accuracy

Limits of agreement of GAR and ISE with the gold standard are presented in Table 2.3 and displayed in Fig. 2.7(a) where they are compared to the inter-observer variability of manual measurements. The error is shown in Fig. 2.7(b) and is expressed as the average difference (in absolute values) between the segmentation methods and the gold standard. The variability index (Eq. 2.4) is shown in Fig. 2.7(c).

Table 2.3: Agreement between the segmentation methods and the gold standard, expressed as bias with its 95% confidence interval (CI) and the population's standard deviation (SD) (computed with Eq. 2.3).

Method	*LoA with gold standard: bias ± 95% CI (SD) [mm]*			
	Vessel		Aneurysm	
	3DRA	MRA	3DRA	MRA
GAR	-0.09 ± 0.03 (0.27)	-0.12 ± 0.04 (0.37)	0.09 ± 0.11 (0.19)	-0.14 ± 0.10 (0.22)
ISE	0.01 ± 0.03 (0.29)	0.15 ± 0.04 (0.39)	0.20 ± 0.12 (0.28)	0.11 ± 0.12 (0.31)

With the exception of the vessel region in MRA, the following observations are valid for GAR. The 95% limits of agreement were within those of manual measurements. The bias, although statistically significant, was small: less than one third of the image spatial resolution (~ 0.3 mm for 3DRA and ~ 0.5 mm for MRA) and two to three times smaller than the standard deviation. The average error, when equally weighted between vessel and aneurysm region, was 0.2 mm for 3DRA and 0.27 mm for ToF-MRA, which was similar to that of manual measurements. The variability index was below 1. Compared to ISE, GAR performed similarly in the vessel region and clearly better in the aneurysm region. In vessel region for MRA, both ISE and GAR performed worse than the manual measurements.

Region overlap

Manual voxel labeling has been performed by two operators on 3DRA and MRA images of the first 4 patients in a region of interest positioned around aneurysm, having an average size of 340000 ($70 \times 70 \times 70$) voxels. The region overlap scores between each of the two segmentation methods and the manual segmentations are shown in Fig. 2.8, and are compared to the corresponding score between both manual segmentations as a measure of the inter-observer variability. The scores were averaged from all pairs of images and gold standard manual segmentations.

The overlap scores with the gold standard, for both segmentation methods were larger or comparable to the inter-observer ones. Thus, no notable mis-segmentation occurred for neither of the methods. Overlap scores for GAR and ISE were similar which suggests that most of the differences between the results of the two methods are at the sub-voxel level.

Efficiency

The GAR execution time depends on the size of the evolving surface i.e. the amount of vasculature being segmented. On average, for a cuboidal region of interest with a size of 256^3 voxels, the execution time was 17 ± 4 min (standard deviation) on a standard PC with an Intel quad-core 2.4GHz processor and 4GB of memory. For ISE, on average ~ 5 min were required to decide on the optimal iso-intensity (the computational time for extraction of the iso-intensity surface was negligible).

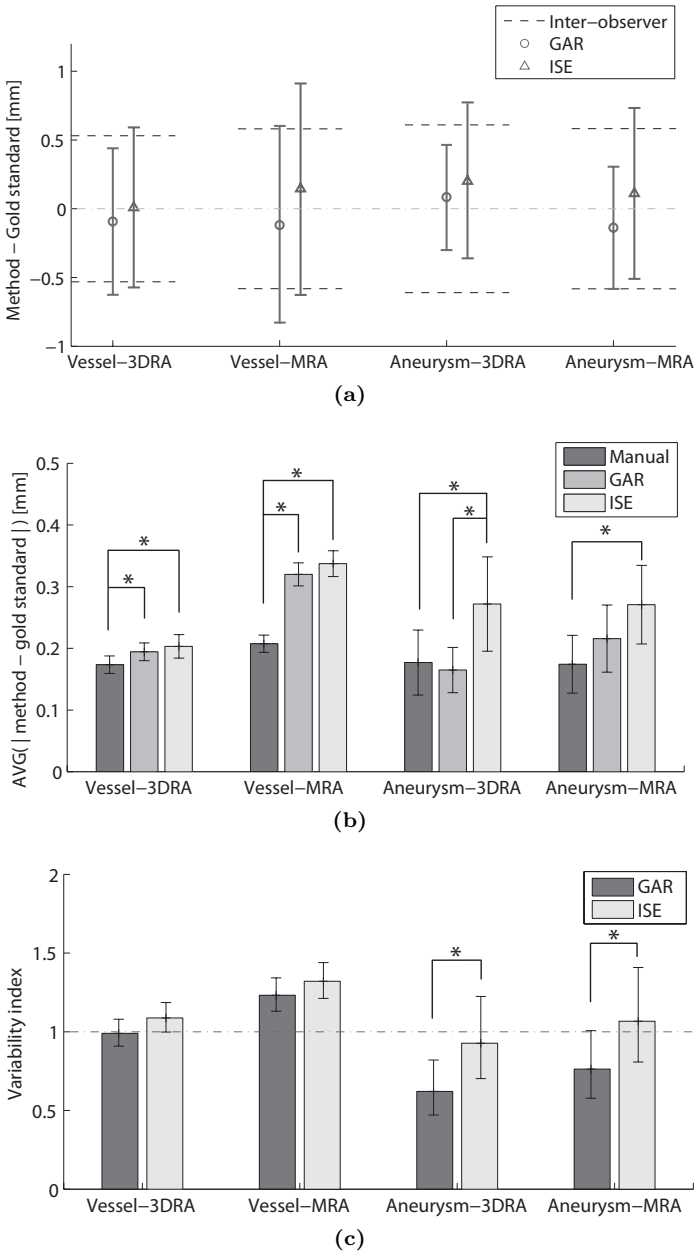

Figure 2.7: (a) Limits of agreement between the segmentation method and the gold standard. Bias is denoted with a marker while the bars correspond to 95% limits of agreement ($\pm 2\sigma_{\widehat{\text{loa}}}$). Agreements are compared with inter-observer limits of agreement for the manual measurements. (b) Average absolute difference from the gold standard with 95% confidence intervals. (c) Variability index with corresponding 95% confidence intervals. In (b) and (c), statistically significant difference ($p < 0.05$, t-test) is denoted with an asterisk (*).

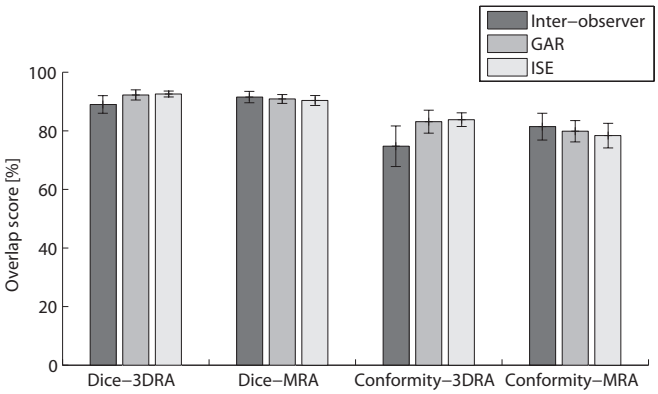

Figure 2.8: Dice and conformity region overlap scores for the segmentation methods and the gold standard, with their 95% confidence intervals.

Table 2.4: Inter-modality limits of agreement, expressed as bias (MRA-3DRA) with its 95% confidence interval (CI) and the population's standard deviation (SD).

Method	*Inter-modality LoA: bias ± 95% CI (SD) [mm]*	
	Vessel	Aneurysm
Manual	-0.21 ± 0.04 (0.48)	0.03 ± 0.22 (0.84)
GAR	-0.24 ± 0.04 (0.49)	-0.37 ± 0.24 (0.69)
ISE	-0.10 ± 0.05 (0.58)	-0.17 ± 0.25 (0.75)

Inter-modality reproducibility

Inter-modality agreement of manual measurements, and GAR and ISE methods are shown in Table 2.4. In the vessel region, GAR performed similar to manual measurements and both had a statistically significant bias. In the aneurysm region, the segmentation methods had large limits of agreement but were within those of the manual measurements. The variability introduced by the mesh registration procedure was 0.12 ± 0.05 mm (standard deviation with its 95% confidence interval), which was small compared to the standard deviations of the inter-modality limits of agreement.

2.4 Discussion

We evaluated the GAR method's potential for segmenting cerebral vessels and aneurysms in 3DRA and MRA images acquired at different medical centers and with different imaging equipment. Three main improvements to the GAR method were introduced to make it suitable for segmenting images from clinical routine. Using an MVN classifier speeded up the region-based probability map computation. Using a voxel based feature scale selection enabled handling a larger variety of image spatial resolutions. The IIS component enabled the training set to be built irrespective of the clinical center and the imaging equipment.

As revealed by the qualitative analysis, the success of the segmentation depended on the local complexity of the vascular geometry, especially in the aneurysm region. Vessels which are very close to each other or to the aneurysm were sometimes merged in the extracted geometrical mesh. This partly happened because of insufficient imaging resolution, which means that more difficult geometrical configurations would require higher resolution and contrast to noise ratio for ensuring successful segmentation. In ToF-MRA images, segmentation was further hampered by large signal variations due to slow or turbulent flow.

In general, when qualitative segmentation errors occur, further interactive post-processing is required to remove the artifacts from the mesh. Favorably, the artifacts are of local nature and are easily detected visually. The methods used for their removal depend on the application. For the use in computational blood flow simulations, a sequence of local operations like mesh element removal and hole filling followed by an additional volume-preserving smoothing are typically applied to improve the mesh quality and to correct for geometrical and topological irregularities. There are various open-source tools already available, like ReMESH [147], MeshLab [148] or GIMIAS [149], which are able to efficiently repair triangular meshes. Repairing the mesh is time consuming and depends on the extent of the artifacts and the operator's experience. As a reference, a single touching vessel artifact can be removed in less than 5 min. However, limiting the occurrence of such artifacts is still a strong incentive for the research community to continue designing new segmentation algorithms.

The GAR method has been compared to the ISE method. The aim was to do the comparison with a method that is already clinically available. ISE is commonly used as a segmentation method on the commercial workstations of the imaging equipment, since the highest intensities in 3DRA and MRA images correspond to vessels [150].

The automated GAR and interactive ISE methods differed from the gold standard within acceptable limits compared to the imaging resolution and had similar region overlap scores. GAR had an average accuracy of 0.2 mm for 3DRA and 0.27 mm for ToF-MRA, and had a repeatability of 0.05 mm. Compared to ISE, GAR had a lower qualitative error in the vessel region and a lower quantitative error in the aneurysm region. Moreover, GAR is automated and its repeatability was superior to both ISE and manual measurements. In contrast, the inter-observer variability of ISE could even result in differences in the extracted vascular topology, which would also mean adding a large variability to any subsequent vascular analysis.

Comparison of our evaluation setup and results to that of the current state of the art methods is given in Table 2.5. All the methods use some variant of the deformable model and produce results with sub-voxel precision. Most require interactive initialization in the form of a seeded region growing. Manniesing et al. [131] study is the most similar to ours. They also presented a fully automated method capable of extracting the whole vascular tree, as opposed to other groups focusing on the interactive segmentation of individual vascular segments, and used manual measurements of the cross-sections as gold standard. However, they describe the shape with only one diameter, no observer variability was reported and no aneurysms were included in the evaluation. Chang et al. [141] and Firouzian

et al. [142] used manual voxel-based segmentations as gold standard, loosing sub-voxel precision in the process. Firouzian et al. limited the evaluation to just the aneurysms but unlike Chang et al. they did report the inter-observer variability. Castro el al [151] and Antiga et al. [130] used digital and physical phantoms, respectively, which enabled them to estimate surface to surface distance to the gold standard. Castro et al. and Chang et al. combined the performance on vessels and aneurysms, which made the results biased towards the ones on vessels since aneurysms composed only a small part of the resulting volume or mesh. Finally, only Chang et al. compared their results with another method: intensity thresholding, a voxel-wise variant of ISE.

Ideally, the results of segmenting the same vasculature from two different modalities should coincide, although some differences might appear due to different image formation mechanisms. Of the two results from the two modalities, we assume that the one from 3DRA is closer to ground truth due to 3DRA's higher imaging resolution and contrast to noise ratio, which is also in agreement with the inter-observer variability being larger in MRA than in 3DRA. Thus, observing the inter-modality agreement in the vessel region, the GAR and the manual measurements tended to undersegment ToF-MRA on average. Probably, the actual vessel lumen was underestimated because of the very slow flow near the vessel wall and the saturation effects so the vessel seemed narrower in the cross-section image. In the aneurysm region we noticed differences in the shape of reconstructed aneurysms between 3DRA and MRA, especially for medium and large sized ones. This may be attributed to the difference in the contrast distribution, visible in 3DRA images, and the blood flow, visible in ToF-MRA images. Thus, although it was recently shown that 3T ToF-MRA and CE-MRA were equivalent in evaluating the occlusion status of cerebral aneurysms [152], CE-MRA might produce better images for the purpose of accurate aneurysm segmentation. However, understanding the cause of these differences between the two modalities goes beyond the scope of this study.

This evaluation study had some limitations. The most important one is that the performance was evaluated only on certain cutting plane positions, not on the entire extracted surface. In addition, cross-sections were only described with two measured widths. This decision was made to have less but meaningful measurements in a larger amount of images and processed by more clinicians. Otherwise the amount of required manual effort would have reduced the number of analyzed patients. However, we did perform a smaller study using region overlap scores and no notable mis-segmentations were observed. Lastly, the imprecision in establishing inter-modality correspondences between the cutting planes might have influenced the inter-modality limits of agreement.

Taking all the evaluation results into account, the GAR performed better than ISE in accuracy and repeatability, also achieving a good agreement with the gold standard in 3DRA and in ToF-MRA imaging modalities. Thus, we conclude that GAR is able to segment 3DRA and ToF-MRA images coming from clinical routine and is better suited than ISE for extracting vascular geometry for use in a computational modeling process.

Automated and repeatable image segmentation technique like GAR is essential to achieve reproducibility and consistency of the subsequent analysis steps in com-

putational modeling pipelines. Such pipelines rely on the availability of accurate patient-specific vascular models and are able to streamline the creation of personalized anatomical, structural and haemodynamic models [10]. These are then used to derive robust and reliable quantitative descriptors providing an integrated decision support system to assess the risk of aneurysm rupture in patients and to optimize their treatments.

Appendix. Multiscale feature vector

The region-based information of GAR is represented in the form of a probability map associated with a particular region R. For the application of vessel segmentation in 3DRA and MRA we define two regions: vessel region and background region. The estimated probability value at each voxel $\mathbf{x}$ of the probability map represents the conditional probability, $P(\mathbf{x} \in R \mid \mathbf{f}(\mathbf{x}))$, that voxel $\mathbf{x}$ belongs to region R observing the feature vector $\mathbf{f}(\mathbf{x})$. The feature vector $\mathbf{f}(\mathbf{x})$ is built from differential invariants [153] up to the second order and in the multiscale framework [154]. Differential invariants are invariant to rigid transformations but not to scale, thus they are computed at several scales (having standard deviations: $\sigma_0 \dots \sigma_m$).

$$\mathbf{f}(\mathbf{x}) = (f_{\sigma_0}, \dots, f_{\sigma_m})(\mathbf{x}). \tag{2.8}$$

The set of derivatives used at one scale consists of the local jet of order two (L, L_i, L^i_j) from which we compute the invariants. The formulation is given in Eq. 2.9, using Einstein tensor notation:

$$\mathbf{f}_{\sigma_n}(\mathbf{x}) = (L, L^i_i, L_i L^i, L^i_j L^j_i, L_i L^i_j L^j, L^i_j L^j_k L^k_i, L_i L^i_j L^j_k L^k). \tag{2.9}$$

When calculating the local jet, the image is convolved with a Gaussian kernel having standard deviation σ_n, which is related to the scale at which we compute the local-jet. Given the impossibility of computing the invariants at all scales, we need to quantize the scales.

To deal with the large variety of possible image resolutions, the scales used for feature calculations are based on voxel spacing and not on world spacing. It assumes that small vessels look like large ones just on a different scale so the number of voxels per vessel diameter is the important factor [155] instead of the vessel width in mm. By modeling the intrinsic image resolution as a Gaussian point spread function with standard deviation of half a voxel size, the standard deviation of the applied Gaussian filter kernel is taken as:

$$\sigma_n = \sqrt{\lambda_n^2 - 0.5^2}, \tag{2.10}$$

where the scales in voxel units are:

$$\lambda_n = 0.5 \exp(n\delta). \tag{2.11}$$

The scale sampling parameter δ was chosen to be 0.3 and the number of scales as 5, $n = 0, \dots, 4$. Both present a compromise between the density of sampling in the scale space and the computational requirements. As a result, the standard deviations of Gaussian filter kernels used are $\sigma_n = \{0, 0.5535, 0.9941, 1.5830, 2.4255\}$, expressed in voxel units. Having 7 features per scale, this produces for each voxel a 35 dimensional feature vector.

Table 2.5: Summary of state of the art methods for cerebral vasculature segmentation.

Method			*Evaluation setup*					*Results*
Reference	Algorithm type	User-interaction	# images	Gold standard	Locations per image	Vessels or aneurysms included	Modality	Accuracy (bias ± SD mm)
This work	deformable model	automated	20	manual measurements	33 cross-sections	both	3DRA ToF-MRA	3DRA: -0.09 ± 0.27 (vessel) 0.09 ± 0.19 (aneurysm) MRA: -0.12 ± 0.37 (vessel) -0.14 ± 0.22 (aneurysm)
			8	manually delineated volume	340K voxels around aneurysm			3DRA: Dice score: 92% Conformity score: 83% MRA: Dice score: 91% Conformity score: 80%
Firouzian et al. (2010) [142]	deformable model	interactive	11	manually delineated volume	all aneurysm voxels	aneurysms	CTA	Dice score: 82.1% volume difference: 14.1 mm^3
Chang et al. (2009) [141]	region growing & deformable model	interactive	15	manually delineated volume	all vessel voxels	both	3DRA	Conformity score: 68.36%
Manniesing et al. (2008) [131]	region growing & deformable model	automated	27	manual measurements	14 cross-sections	vessels	CTA	CTA: 0.0 ± 0.4
Antiga et al. (2008) [130]	colliding fronts & deformable model	interactive	2	physical phantom (patient specific)	entire vessel surface	vessels	CTA CE-MRA	CTA: 0.01 ± 0.06 MRA: -0.08 ± 0.11
Castro et al. (2006) [151]	region growing & deformable model	interactive	1	digital phantom	entire vessel surface	both	3DRA	maximal surface distance: 0.2 mm

3

Automated Landmarking and Geometric Characterization of the Carotid Siphon

This chapter presents a methodology for an objective and extensive geometric characterization of carotid siphon parameterized by a set of anatomical landmarks. We introduce a complete and automated characterization pipeline. Starting from the segmentation of vasculature from angiographic image and its centerline extraction, we first identify internal carotid artery (ICA) by characterizing vessel tree bifurcations and training a support vector machine classifier to detect ICA terminal bifurcation. On ICA centerline curve, we detect anatomical landmarks of carotid siphon by modeling it as a sequence of four bends and selecting their centers and interfaces between them. Bends are detected from the trajectory of the curvature vector expressed in the parallel transport frame of the curve. Finally, using the detected landmarks, we characterize the geometry in two complementary ways. First, with a set of local and global geometric features, known to affect hemodynamics. Second, using large deformation diffeomorphic metric curve mapping (LDDMCM) to quantify pairwise shape similarity. We processed 96 images acquired with 3D rotational angiography. The characterization based on pair-wise LDDMCM performed better in classification of the carotid siphon shape classes than the one based on geometric features.

The content of this chapter is adapted from the following publication:

H. Bogunović, J.M. Pozo, R. Cárdenes, M.C. Villa-Uriol, R. Blanc, M. Piotin, and A.F. Frangi. Automated Landmarking and Geometric Characterization of the Carotid Siphon. *Medical Image Analysis*, 16(4): 889-903, 2012.

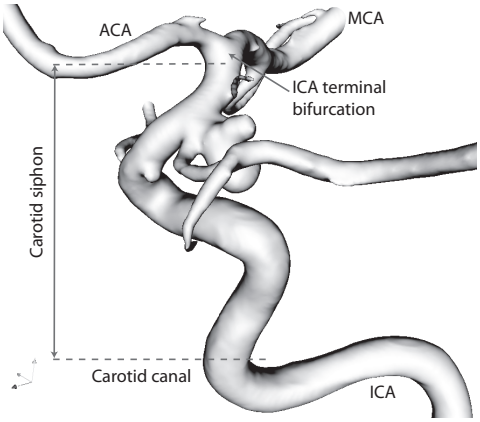

Figure 3.1: Carotid siphon with an aneurysm on the bifurcation with the posterior communicating artery.

3.1 Introduction

The locations where vascular pathologies tend to occur more frequently are in general non-uniformly distributed across the vasculature. For example, cerebral aneurysms (pathological bulging of arteries) have strong preference for occurring at specific locations, and are frequently found at or near the regions of high vascular curvature in arteries of the Circle of Willis [9]. Similarly, atherosclerosis (thickening of the arterial wall) often occurs at carotid bifurcation [12] or near the bifurcations of coronary arteries [13, 156].

Since geometry varies among different locations in the vasculature, it is believed that this geometric variation contributes to a corresponding variation in predisposing hemodynamic forces [20]. These forces, coming from blood motion, are speculated to play an important role in the initiation and localization of pathologies, which in turn could explain their nonuniform distribution [18]. Taking this into account, Friedman et al. [21] introduced the concept of "geometric risk factors" as the geometric features that provoke high hemodynamic stresses on the vessel wall.

An important condition for the geometric risk factor concept is the presence of sufficient individual variability in geometry to induce important variations in individual hemodynamics [31]. One vessel of clinical interest that satisfies this requirement is the internal carotid artery (ICA). Located on each side of the neck, ICA is the main vessel that feeds blood to the arteries forming the anterior circulation of the brain. The geometry of ICA varies widely across the population, in particular the part known as the carotid siphon [157]. The carotid siphon (Fig. 3.1) is the tortuous segment of the ICA that extends from the carotid canal to the terminal bifurcation (ICA-TB) at which the ICA bifurcates into the anterior cerebral artery (ACA) and the middle cerebral artery (MCA).

Geometry of ICA is of special interest as incidence rate of aneurysms on it is high, as one third of all cerebral aneurysms occur along the carotid siphon or its terminal bifurcation [9]. A couple of studies already identified effects linking

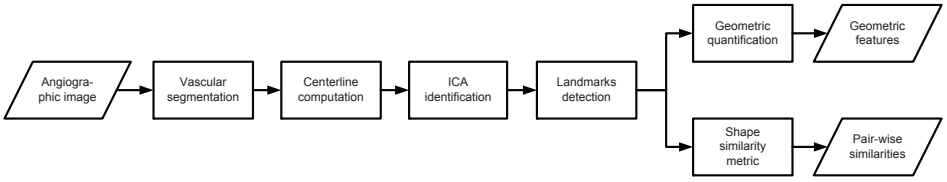

Figure 3.2: The image-based pipeline for geometric characterization of the carotid siphon.

geometry and aneurysmal pathology on ICA. Piccinelli et al. [158] concluded that ICA bends hosting ruptured aneurysms tend to be shorter, having smaller radius, lower maximum curvature, and the aneurysms are located closer to the bend center. Kim et al. [159] found that a relatively shorter length of the supraclinoid ICA may be a risk factor for the development of an ICA-posterior communicating artery aneurysm due to higher hemodynamic stress. The geometry of ICA was also of interest to evaluate endovascular accessibility of lesions and for treatment planning, which involves choosing the optimal path and selecting the appropriate type of microcatheters, guidewires and stents [38, 41, 42, 160].

The aim of this work is to provide a methodology for extensive geometric characterization of carotid siphon in an objective, robust and automated way, starting from an angiographic image. The characterization should allow the comparison of carotid siphons within and between subjects and measure their similarity. Such a method would facilitate cataloguing the normal values and the variability of carotid siphon geometry to guide future exploration and identification of specific geometric risk factors.

The summary of the chapter is the following. In section 3.2, we overview the state-of-the-art in the geometric characterization of vasculatures. In section 3.3, we start presenting the automated characterization pipeline (Fig. 3.2), with a focus on identifying ICA and detecting anatomical landmarks of carotid siphon. Based on these landmarks of correspondence, we propose two approaches for the geometric characterization (Fig. 3.2). One is based on computing several geometrically intuitive features (section 3.4), while the other on measuring the pair-wise similarity between carotid siphons taking their entire shape into account (section 3.5). In section 3.7, we validate the automated ICA identification and landmark detection and compare the two characterization approaches in their ability to separate carotid siphons having different shape classes, related to endovascular accessibility. Finally, section 3.8 discusses the benefits and limitations of the proposed characterization and presents our conclusions.

3.2 Related work

The geometric characterization of vasculature and in particular of ICA, have already attracted a lot of attention. The state-of-the-art can be divided into two main approaches. The most common one is to represent the vessel shape with a set of geometric indices, which are considered as candidates for being geometric risk factors. The other approach is to consider each point of a centerline as a function of its arc length parameter and then apply functional data analysis (FDA) to

explore the variability in a population.

Bullitt et al. [95] focused on the measure of tortuosity of the intracerebral vasculature. Three different tortuosity metrics were compared by their effectiveness in detecting several types of abnormalities. The same authors in [45], created a set of vessel attributes containing radius, three measures of tortuosity and branching pattern. Statistical properties of these attributes were then explored. In [161], the aim was to evaluate the maximal magnitude of deformation on the coronary artery and intracoronary devices due to heart contraction. Curvature, torsion and tortuosity and their change along the heart cycle were computed in a selected region of a coronary tree. In [96], tortuosity and deviation index as well as curvature angle were computed for describing the terminal part of the basilar artery. O'Flynn et al. [36] described the anatomy of normal human abdominal aorta and its side renal arteries with tortuosity, non-planarity of bifurcations, branching angles, curvature and torsion. In the works by Meng et al. [100,101], carotid siphon is characterized by its spatial complexity defined as the sum of the curvature and torsion energy. The above methods, apart that they limit the characterization to a small set of isolated geometric indices, require user-interaction.

A framework for geometric analysis of vasculature is introduced by Piccinelli et al. [57]. Starting from image segmentation and centerline extraction, vascular structures, are objectively characterized using computational geometry. Curvature, torsion and tortuosity are used to characterize centerlines. Parallel transport on the normal vector bundle of a curve is used for comparing angular positions at different locations. Using such framework, in [158], they presented a geometric characterization of ICA and searched for patterns that can be associated to the presence and rupture status of aneurysms. Vessel centerline is partitioned into a sequence of quasi-planar bends. Each bend is then characterized with several geometric indices: torsion peaks at proximal and distal endpoints, mean and maximum curvature, length, radius, angular orientation of aneurysm, etc. However, their method does not guarantee the correspondence of the bends, which is reflected by the discrepancy in the number of bends obtained from different subjects. Furthermore, the number of such obtained bends strongly depends on the applied scale for vessel centerline smoothing.

As opposed to computing geometric indices, Sangalli et al. [162] applied FDA to characterize a set of centerline curves of ICA. An atlas of curves was created where the reference curve and a set of affine transformations of arc length parameter are simultaneously estimated by Procrustes fitting. From the set of aligned curves, functional principal component analysis of their local radius and curvature was performed. Using the principal modes of variation corresponding to the change in radius and curvature, they were able to discriminate patients with aneurysms in different areas. In [163], they extended their atlas to allow for multiple reference curves. A method called *k-mean alignment* is proposed for simultaneous alignment and clustering of spatial curves. Thus, each cluster center corresponds to a different reference curve. They were able to obtain two reference curves which correspond to the two main classes of carotid siphon shape: Ω-shaped and S-shaped. However, as the transformations are restricted to be affine, the alignment does not assure correspondences between points and bends of curves. These inter-subject anatomical correspondences are essential for computing geometrical

descriptors. Besides, we consider them an important requirement for the correct shape comparison between ICAs.

3.3 ICA segmentation

3.3.1 Segmentation of the vasculature

Segmentations of the vasculature are performed in an automated way with a geometric deformable model called Geodesic Active Regions (GAR) [78, 164]. The method was demonstrated to be accurate for 3D rotational angiography (3DRA) and time-of-flight magnetic resonance (TOF-MRA) images. The result of the segmentation is a triangular mesh modeling the vascular lumen with sub-voxel precision.

3.3.2 Vascular tree centerlines computation

The shape of tubular objects, like vessels, can be approximated by the shape of their centerline (medial axis), which is a 3D spatial curve. We obtain the set of vessel centerlines in two steps. First, to obtain the estimate of the topology of the vascular tree, fast topological thinning based on collapsing fronts followed by a fast marching computation to assure centerline connectivity [165] was applied to obtain the skeleton of the segmentation (Fig. 3.3). The skeleton, due to imaging resolution and segmentation inaccuracies producing touching vessels, might not have the topology of a tree. However, its end-points do correspond to the root and the terminal leaves of the underlying vascular tree. The root was taken to be the end-point with the maximal associated radius at the lowest axial plane, which corresponded to the ICA entering the imaged field of view.

Second, the set of accurate centerlines is obtained by backtracking along the minimal cost path from the end-points toward the root using [88], implemented in the open-source library VMTK [166]. Every point of such centerline, corresponds to the center of a maximally inscribed sphere and the set of centerlines topologically form a rooted tree with the edges directed away from the root in accordance with the blood flow.

3.3.3 ICA identification

To identify ICA in the extracted vascular tree, we applied the method for detecting ICA-TB, that we preliminarily presented in [167]. A machine learning based approach is applied, where a classifier is trained on a set of labeled bifurcation feature vectors. Then, a breadth-first traversal of tree bifurcations is performed until the first positive detection. With this strategy we only needed to differentiate ICA-TB from other bifurcations along the ICA as the potential error would appear either as a false positive along the ICA or a false negative at its terminal bifurcation.

Origins of the bifurcations forming the vessel tree and their bifurcation vectors (unit vectors denoting directions of parent vessel and the two daughter branches), are defined using the objective and robust criteria of [56, 57]. The two daughter

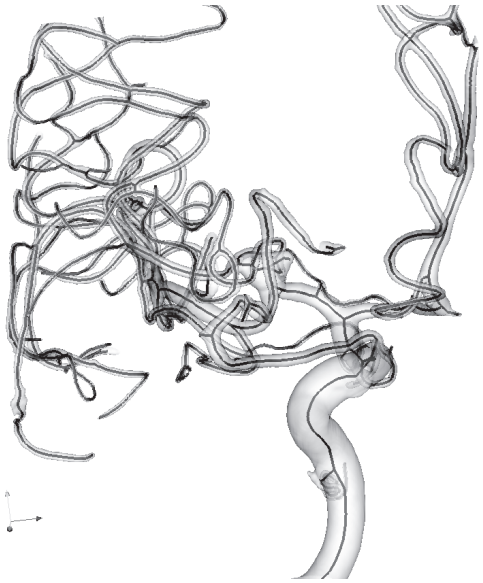

Figure 3.3: Segmented vascular mesh and its skeleton.

branches are differentiated by their radius: the larger daughter branch and the smaller daughter branch. Then, each bifurcation is geometrically characterized with the following 15 dimensional feature vector:

- Ratios of mean vessel radii between each pair of vessels forming the bifurcation (3).
- Sagittal, axial and coronal-components of the three bifurcation vectors (9).
- Angles between each pair of bifurcation vectors (3).

When compiling the feature vector, the two daughter branches are differentiated by their radius: Larger daughter branch and smaller daughter branch (Fig. 3.4(a)).

As a classifier, we employed $C-$Support vector machine ($C-$SVM) [168] where the training feature vectors $\vec{x}_i$ are mapped into a higher dimensional space having inner-product defined by a Gaussian kernel:

$$K(\vec{x}_i, \vec{x}_j) = \exp(-\gamma \|\vec{x}_i - \vec{x}_j\|^2), \qquad \gamma > 0 \tag{3.1}$$

SVM then finds a linear separating hyperplane with the maximal margin in this higher dimensional space. It has two parameters: the penalty C of the training error and the kernel parameter γ. Optimal classifier parameter values were obtained by a simple grid search through multiple combinations. The ones giving the best cross-validation (CV) score were chosen.

Finally, once the ICA-TB is detected, ICA is extracted as a sequence of 4D points (3 spatial centerline coordinates plus the vessel radius) along a curvilinear abscissa starting from the ICA-TB and proceeding toward the heart until it reaches the root of the tree (Fig. 3.4(b)).

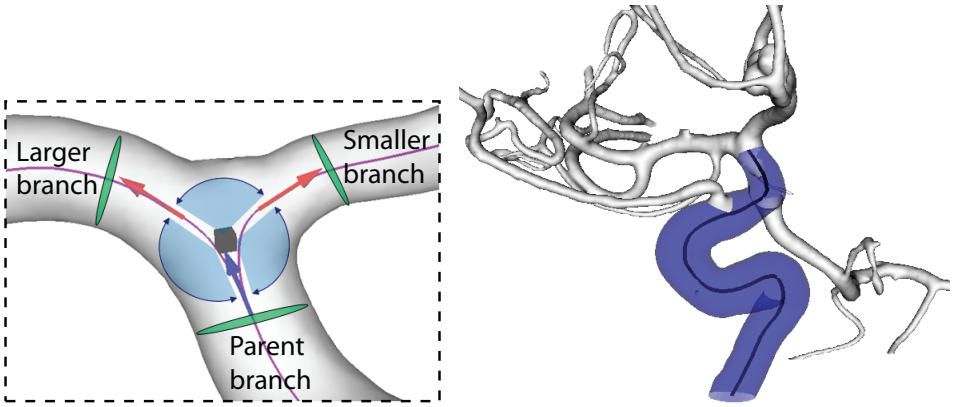

Figure 3.4: (a) Bifurcation characterization: Origin (black cube) and associated bifurcation vectors. (b) Example of identified ICA and its centerline. (See color insert)

3.3.4 Carotid siphon landmarks

To compare carotids within and between subjects, we identify a set of sparse landmark points of anatomical correspondence. They are essential as they will serve as a base for geometric characterization. We model the carotid siphon, the part of ICA from terminal bifurcation to carotid canal, as a sequence of four bends named (from ICA-TB towards the heart): *superior*, *anterior*, *posterior* and *inferior* bend, following their anatomical position with respect to the siphon center (Fig. 3.5). The inferior, posterior and anterior bends have been observed to be highly planar.For the superior bend, the planar approximation is not found to be valid as its shape resembles more a helix (non-zero torsion).

The landmarks we selected corresponded to: ICA-TB, the centers of the bends and to the interfaces between the bends of the model. However, for the helical superior bend, the location of its center turned out to be highly ambiguous and that landmark has consequently been omitted. The final set of chosen seven landmarks is shown in Fig. 3.5.

As the landmarks are associated with the four-bend model, we first identify the four bends on a centerline spatial curve. For this, we will make use of two natural frames defined on a spatial curve: The Frenet-Serret and the parallel transport one [169,170]. We start by giving an overview of the two frames and then present the method for bends and landmarks detection.

Frames on a spatial curve

Given a regular parameterized differentiable space curve Γ with a normalized arc length parameter s,

$$\Gamma = \{\vec{x}(s) | s \in [0,1], \vec{x} \in \mathbb{R}^3\}, \tag{3.2}$$

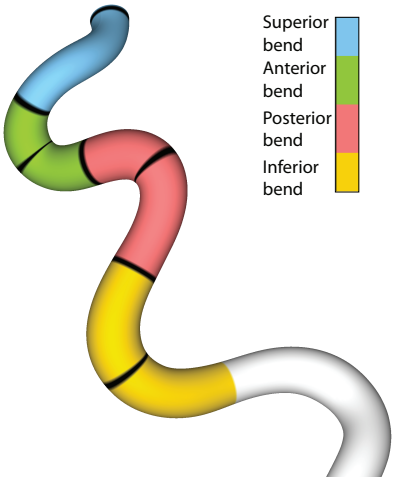

Figure 3.5: Carotid siphon with the four bends (in color) and the seven landmarks (in black). White area denotes: outside the region of interest. (See color insert)

the Frenet-Serret frame is defined locally by a triad: tangent $\vec{T}(s)$, normal $\vec{N}(s)$ and binormal $\vec{B}(s)$,

$$\begin{aligned}\vec{T}(s) &= \vec{x}\,'(s)\\ \vec{N}(s) &= \frac{\vec{T}'(s)}{\parallel \vec{T}'(s) \parallel} = \frac{\vec{x}\,''(s)}{\parallel \vec{x}\,''(s) \parallel}\\ \vec{B}(s) &= \vec{N}(s) \times \vec{T}(s) = \frac{\vec{x}\,'(s) \times \vec{x}\,''(s)}{\parallel \vec{x}\,'(s) \times \vec{x}\,''(s) \parallel}.\end{aligned} \tag{3.3}$$

Thus, $(\vec{T}(s), \vec{N}(s), \vec{B}(s))$ forms an orthonormal basis. $\vec{N}$ is a unit vector pointing towards the center of the locally osculating circle, i.e. in the direction the curve is curved. The vector $\vec{T}'(s) = \kappa(s)\vec{N}(s)$, with the magnitude being the scalar curvature $\kappa(s) = \parallel \vec{x}\,''(s) \parallel$, is then called the *curvature vector*. Example of Frenet-Serret frame on a spatial curve is given in Fig. 3.6(a). Frenet-Serret frame can change orientation abruptly and is not defined when curve is locally straight ($\vec{x}\,''(s) = 0$).

The parallel transport frame [169], is the frame obtained by parallel transport in the normal bundle of the curve. It can be obtained from any orthonormal basis $\{\vec{E_1}(0), \vec{E_2}(0)\}$ spanning the plane orthogonal to the tangent $\vec{T}(0)$ at the initial point $\vec{x}(0)$, by parallel transporting it along the curve. The following equation defines such a frame:

$$\begin{bmatrix} \vec{T}'(s) \\ \vec{E_1}'(s) \\ \vec{E_2}'(s) \end{bmatrix} = \begin{bmatrix} 0 & k_1(s) & k_2(s) \\ -k_1(s) & 0 & 0 \\ -k_2(s) & 0 & 0 \end{bmatrix} \begin{bmatrix} \vec{T}(s) \\ \vec{E_1}(s) \\ \vec{E_2}(s) \end{bmatrix}. \tag{3.4}$$

$\vec{E_1}'$ and $\vec{E_2}'$ depend only on $\vec{T}$ and are parallel to it, hence are well defined everywhere on a regular spatial curve, regardless of curvature. Example is given in

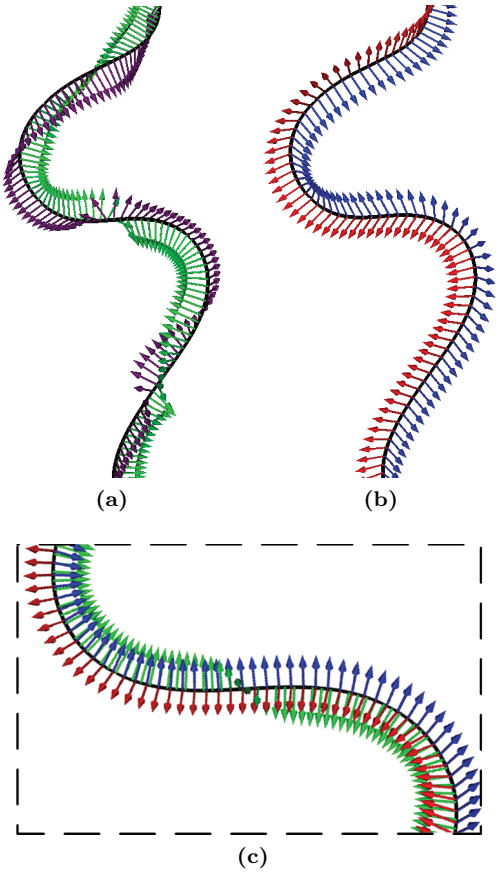

Figure 3.6: Centerline spatial curve with: (a) Frenet-Serret frame with normal $\vec{N}$ (green) and binormal $\vec{B}$ (purple) vectors. (b) Parallel transport frame with $\vec{E_1}$ and $\vec{E_2}$ (red and blue). (c) Normal vector $\vec{N}$ in the region of bend transition changes the orientation with respect to $\vec{E_1}$ and $\vec{E_2}$. (See color insert)

Fig. 3.6(b). Such frame is smoothly varying and not affected by the underlying torsion.

We are interested in representing the curvature vector in the parallel transport frame:

$$\vec{T}'(s) = \kappa(s)\vec{N}(s) = k_1(s)\vec{E_1}(s) + k_2(s)\vec{E_2}(s). \tag{3.5}$$

Thus, k_1 and k_2 are the components of the curvature vector with respect to basis $\{\vec{E_1}, \vec{E_2}\}$ and every spatial curve is uniquely represented in the (k_1, k_2) space up to a rotation. Indeed, this introduces a natural extension to 3D of the notion of the oriented or signed curvature restricted to 2D plane curves. Such a representation avoids the computation of torsion (which requires third-order derivatives), hence we only require curves to be of class C^2, which makes it more stable and robust to the level of noise on the extracted curve.

Bends and landmarks detection

Bends are curved parts of the centerline and are separated by a local curvature minimum at their ends. However, the total number of the curvature extremums varies across population and also depends on the scale and on the extent of ICA visible in the image. To avoid false positive detections due to consecutive curvature minimums forming the same anatomical bend, we will make use of curvature vector expressed in the parallel transport frame. The main idea is to use the property that the curvature vector changes orientation at the bend transitions, while $\vec{E_1}$ and $\vec{E_2}$ of the parallel transport frame remain stable along the curve (Fig. 3.6(c)). To detect the bend transitions, we then use the curve representation in the above defined (k_1, k_2) space. Thus, the change of bends between two centerline points corresponding to local curvature maximums is expected to produce a wide angle ($\theta > 90°$) between their vectors. On the other hand, if the angle between them is small ($\theta < 45°$), the two curvature maximums are expected to belong to the same bend (Fig. 3.8(a)).

We argue that this is a more robust approach to bend subdivision than the one based on observing the torsion and curvature peaks along the centerline, presented by Piccinelli et al. [158]. The sensitivity of the torsion profile to the amount of noise on the centerline makes it difficult to select the level of centerline smoothing, as the level appropriate for one subject is not necessarily appropriate for the others. The proposed representation in (k_1, k_2) space is a more stable approach as the angle between curvature vectors of two centerline points corresponds to the amount (integral) of torsion between them. Detecting bend transitions with a set of angle thresholds was able to consistently identify the corresponding bends across subjects. This is demonstrated in Fig. 3.7, where the results of the two approaches are compared.

The landmark that will serve as a reference point to identify all four anatomical bends is the one in the middle, marking the interface between the anterior and the posterior bend. It is identified by combining the curvature information with the coronal coordinate of the centerline (Fig. 3.8(b)). As the anterior bend is anatomically positioned at the front, starting from the position of maximum of the coronal coordinate of the centerline and moving against the blood flow we search for the two neighboring curvature maximum points that have $\theta > \alpha_{\text{ant-post}}$, where $\alpha_{\text{ant-post}}$ is a threshold parameter. The point of curvature minimum between the two such maximums is then the interface landmark.

From the anterior-posterior interface landmark, and moving along the blood flow, we identify the anterior and the superior bends by searching for their interface landmark point as curvature minimum where the two surrounding points of curvature maximums have $\theta > \alpha_{\text{sup-ant}}$. Similarly, moving opposite to the blood flow we identify the posterior-inferior interface landmark with $\alpha_{\text{post-inf}}$. Subsequently, the end of the inferior bend and ROI is found with $\alpha_{\text{inf-end}}$. The threshold parameters were fixed to $\alpha_{\text{ant-post}} = 60°$, $\alpha_{\text{sup-ant}} = \alpha_{\text{post-inf}} = 45°$, and $\alpha_{\text{inf-end}} = 110°$ after observing θ values appearing in a subset of our data.

Once the bends are detected, we estimate their central landmarks. We model the central landmark to correspond to the center of the curved segment of the bend at a scale where its centerline has only one curvature maximum. Thus, if a bend is initially composed of multiple curvature peaks we observe the bend at a

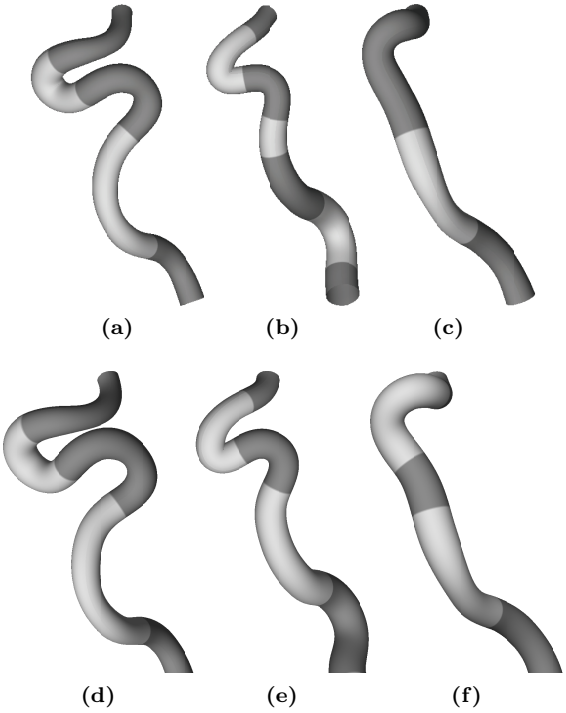

Figure 3.7: Subdivision of carotid siphon into bends. (a-c) Bend subdivision using the method of [158] with the same level of Laplacian smoothing of the centerlines. The scale appropriate for case (a), is to small for case (b) and too large for case (c). (e-f) The four bends detected on the same subjects using the proposed method, with fixed, small level of centerline smoothing.

larger scale. This is achieved by convolving the centerline curve of the bend with a Gaussian function, as the standard deviation of the Gaussian increases. Such curve evolution is repeated until only one curvature maximum remains. Then, the central segment is defined as the region around the curvature maximum, delimited on both sides by the mean of the curvature values at the maximum and at the corresponding end. The central landmark is taken as the midpoint of the central segment (Fig. 3.8(c),(d)).

3.4 Geometric quantification

Having identified the bends and the landmarks of the carotid siphon, we are now able to compute a set of local and global features that quantify its geometry. As the shape is defined by the object geometry that is invariant under *similarity transformation* (translation, rotation, and uniform scaling) [171], the proposed set of features is accordingly made invariant under this transformation. We compute the following set of geometric features.

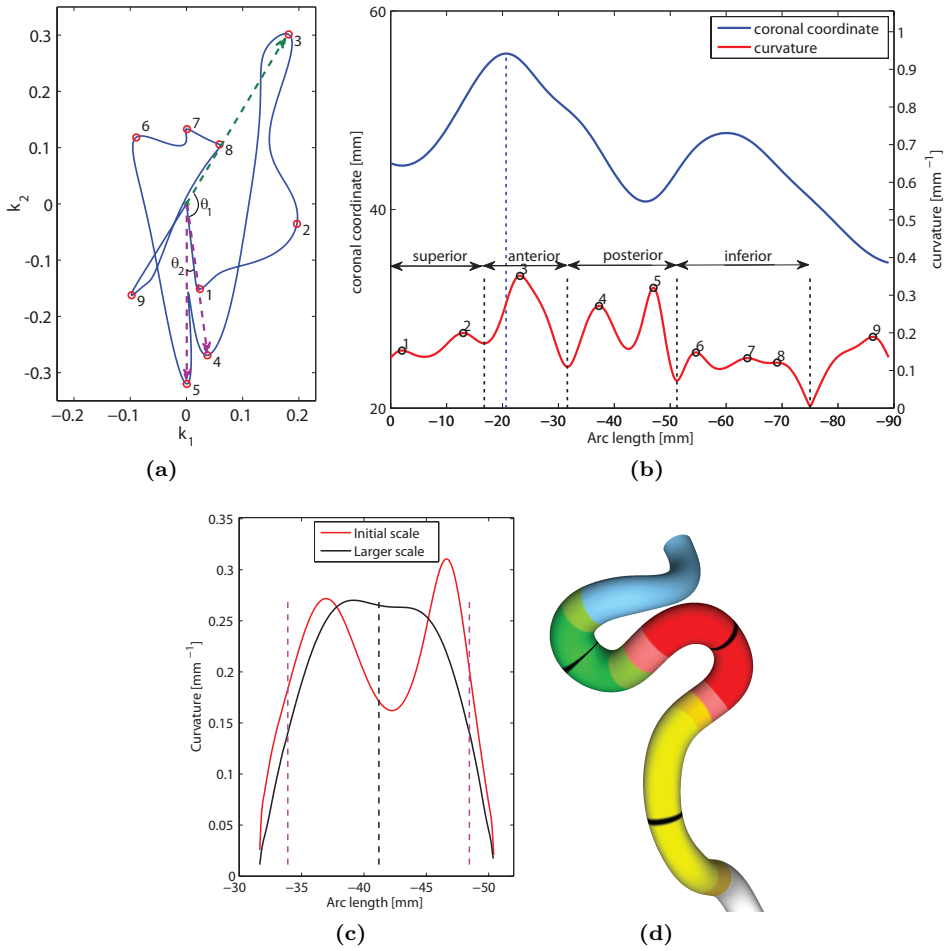

Figure 3.8: Bends and landmarks detection: (a) (k_1, k_2) space of the centerline. Numbers denote the curvature peaks sequentially starting from ICA-TB. Between points 3 and 4 ($\theta_1 \approx 120°$) there is a transition of bends. Points 4 and 5 ($\theta_2 \approx 20°$) belong to the same bend (posterior). (b) Coronal coordinate and the curvature of the centerline. The global coronal coordinate maximum is denoted with vertical blue line. The interface landmarks between the four bends are denoted with vertical black lines. (c) Estimation of central segment (bounded with two vertical magenta lines) and central landmark (vertical black line) of the posterior bend, using scale space. (d) The four bends with their central segments (in more saturated color: green, red, yellow) and central landmarks (black). (See color insert)

3.4.1 Bend lengths and average vessel radius

Lengths of each of the four bends are presented as percentages of the region of interest occupied by each of the bends, obtained from their normalized arc lengths.

Vessel cross-section area is more related to hemodynamic properties than the radius of the maximally inscribed sphere [102]. Thus, we define as local vessel radius, the radius of a circle having the same cross-section area. Along the centerline of the bend, perpendicular cutting planes are automatically positioned to obtain

the vessel cross-sections from the segmented mesh, and the circle equivalent radius is computed. However, if the aspect ratio of minimal over maximal cross-section diameter is below certain threshold (the value of 0.75 is chosen after visual observation), the section is considered to cross an aneurysm or a vessel bifurcation, the cross-section is ignored and its diameter value is linearly interpolated from its neighbors.

3.4.2 Osculating planes

For the bends that are observed to be quasi-planar (inferior, posterior, anterior), their osculating planes are fitted to the points forming the central segment of each bend using least squares fit. The plane normal vector defined by its sagittal, axial and coronal-components is then used as a feature.

3.4.3 Change of osculating planes

The bends forming the siphon are concatenated in a non-planar way and the osculating planes change. In general, it has been shown that non-planar connection of double-bend geometries influences the hemodynamics, especially the mixing and swirling of blood flow [99]. Thus, we quantify this change of osculating planes of the siphon with the following values:

- Angles between all pairs of osculating plane normal vectors $\vec{n}_i$ computed directly as: $\arccos(\vec{n}_i \cdot \vec{n}_j), i \neq j$.

- Directed angles between osculating plane normal vectors of consecutive bends, computed after parallel transporting one to another on the normal bundle of the curve.

- Two directed angles describing the ouf-of-plane rotation (OPR) of two consecutive bends (*proximal* and *distal*): inferior and posterior; posterior and anterior. One (OPR_1) corresponds to the rotation around the axis lying in the plane of the proximal bend while being orthogonal to the centerline tangent at the transition landmark between the two bends (Fig. 3.9(a)). The other (OPR_2) corresponds to the rotation around the axis defined by the centerline tangent at the transition landmark between the two bends (Fig. 3.9(b)).

3.4.4 Bending radii

The points of the central segment of each planar bend are fitted with a circle using Gauss-Newton method for non-linear least squares optimization (Fig. 3.10). Radius of the circle divided by the average vessel diameter of the corresponding bend is then used.

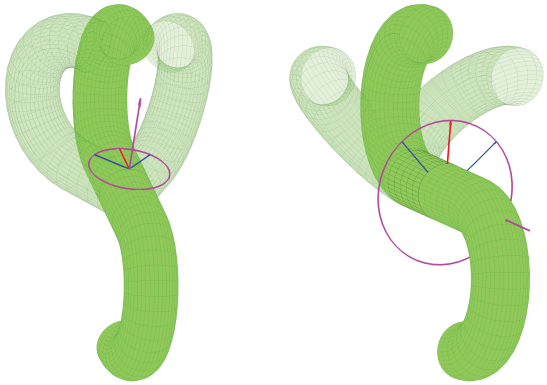

(a) OPR_1 **(b)** OPR_2

Figure 3.9: Illustration of the measured change of osculating planes between the posterior and the anterior bend. Each angle (between blue and red vectors) measures the rotation around the corresponding axis (magenta). (See color insert)

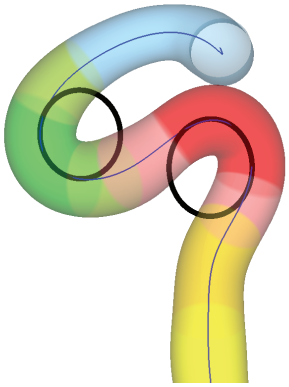

Figure 3.10: Circles (in black) fitted to the central segments of the anterior and the posterior bends. (See color insert)

3.4.5 Global features

Global features are computed from the region of interest starting from the terminal bifurcation of ICA until the most proximal landmark (center of the inferior bend). We consider five global features:

Tortuosity Defined as the relative increment in the length of a curve deviating from a rectilinear line, tortuosity χ is computed as [57]:

$$\chi = \frac{L}{d} - 1, \tag{3.6}$$

where L is the total arc length of the centerline under analysis and d is the Euclidean distance between its endpoints.

Bending and twisting energy The energy required to bend and twist a straight

line into its curved shape. It corresponds to the average value of the square curvature κ and torsion τ, respectively, over the total arc length L of the centerline under analysis. Bending energy (BE) and twisting energy (TE) are defined as [101]:

$$\mathrm{BE} = L^2 \int_0^1 \kappa^2(w)dw; \quad \mathrm{TE} = L^2 \int_0^1 \tau^2(w)dw, \tag{3.7}$$

The L^2 factor guarantees scale invariance.

Curvature ratio and torsion ratio Dimensionless ratios of vessel radius with curvature and torsion radii form part of the Dean and Germano numbers that characterize flows in curved tubes [172]. Thus, we define mean squared curvature ratio (CR) and mean squared torsion ratio (TR) as:

$$\begin{aligned} \mathrm{CR} &= \int_0^1 R^2(w)\kappa^2(w)dw; \\ \mathrm{TR} &= \int_0^1 R^2(w)\tau^2(w)dw, \end{aligned} \tag{3.8}$$

where, R, κ and τ are local vessel radius, curvature and torsion, respectively.

3.5 Shape similarity metric

In addition to geometric quantification, we characterize the variability of carotid siphon shapes using the framework of computational anatomy [113]. There, shape variations are modeled by diffeomorphisms (differentiable transformations with differentiable inverse). One of the proposed paradigms for diffeomorphic registration is the large deformation diffeomorphic metric mapping (LDDMM) [116], which apart from providing correspondences between shapes defines a metric in shape space.

To establish the shape similarity distance measure between carotid siphons, we use the large deformation diffeomorphic metric curve mapping (LDDMCM) [173], between each pair of their centerline curves. The registration of two spatial curves C and S is performed by searching for a diffeomorphism φ, which matches the given curves: $\varphi(C) = S$, taken as the end point $t = 1$ of a flow of diffeomorphisms ϕ_t modeled by a time-dependent velocity vector field $v_t : \mathbb{R}^d \to \mathbb{R}^d$ as

$$\frac{\partial \phi_t}{\partial t} = v_t(\phi_t); \quad \phi_0(x) = x. \tag{3.9}$$

The distance between the two curves in the shape space, D(C,S), is then defined by the *length* of the *shortest* diffeomorphism flow matching them:

$$D(C, S) = \inf \rho(\phi_t), \quad \text{when} \quad \phi_0(C) = C, \quad \phi_1(C) = S. \tag{3.10}$$

The *length* is defined as the deformation cost function

$$\rho(\phi_t) = \left(\int_0^1 ||v_t||_V dt \right)^{\frac{1}{2}}, \tag{3.11}$$

where the space V is a reproducing kernel Hilbert space (RKHS) of the smooth velocity fields with reproducing kernel being the Gaussian function with standard deviation σ_V, which determines the smoothness of the deformation.

The optimal transformation $\varphi = \phi_1$ is then computed by minimizing the energy functional

$$J_{C,S}(\phi_t) = \gamma\rho(\phi_t)^2 + E(\phi_1(C), S), \tag{3.12}$$

where E is a curve matching term and γ is a parameter of regularization weight. The matching term defined in [173] was

$$E_{\mathrm{cr}}(\phi_1(C), S) = ||\mu_{\phi_1(C)} - \mu_S||^2_{W^*}, \tag{3.13}$$

where μ_C is a linear functional that embeds the curve C in a RKHS W^* of *currents*, enabling comparison of curves without assuming point correspondences between them. The reproducing kernel is defined by the Gaussian function with standard deviation σ_W, representing a spatial scale of *currents*, and determines the scale of geometric details of curves that are taken into account. σ_W was set to a small value of 2 mm.

We extend the matching term by landmark matching of our previously (subsection 3.3.4) extracted $N = 7$ landmarks $(\vec{x_n}, \vec{y_n}), n = 1, \ldots, N$. This assures anatomically valid matching as the anatomical landmarks are required to correspond. We apply inexact landmark matching [174] with normalized Euclidean metric, assuming independency between the landmarks

$$E_{\mathrm{lm}}(\phi_1(\vec{x}), \vec{y}) = \sum_{n=1}^{N} \frac{||\vec{y_n} - \phi_1(\vec{x_n})||^2}{\sigma_n^2}, \tag{3.14}$$

where each landmark n has σ_n associated, which represents the expected inaccuracy in its localization.

Thus, the final energy term that we minimize is

$$\begin{aligned} J_{C,S,\vec{x},\vec{y}}(\phi_t) = \gamma\rho(\phi_t)^2 &+ \gamma_{\mathrm{cr}} E_{\mathrm{cr}}(\phi_1(C), S) \\ &+ \gamma_{\mathrm{lm}} E_{\mathrm{lm}}(\phi_1(\vec{x}), \vec{y}), \end{aligned} \tag{3.15}$$

where γ, γ_{cr}, and γ_{lm} are weights of the regularization, curve matching and landmark matching terms, respectively. As the E_{cr} and E_{lm} matching terms are not symmetric to the choice of source and target curves, neither is the resulting pairwise distance. To symmetrize it, we take the distance to be the mean value from minimizing $J_{C,S}$ and $J_{S,C}$:

$$D(C, S) = \frac{1}{2}(D(C, S) + D(S, C)). \tag{3.16}$$

Before the start of the LDDMCM registration, the two curves are registered under the similarity transformation as any variability described by this transformation is not considered as difference in shape. The importance of adding the landmark matching term is demonstrated in Fig. 3.11. Although the transformed centerlines are similar, the registration without using the landmarks does not provide correct anatomical correspondences of the bends and underestimates the geodesic distance in shape space, compared to the one that does match the landmarks.

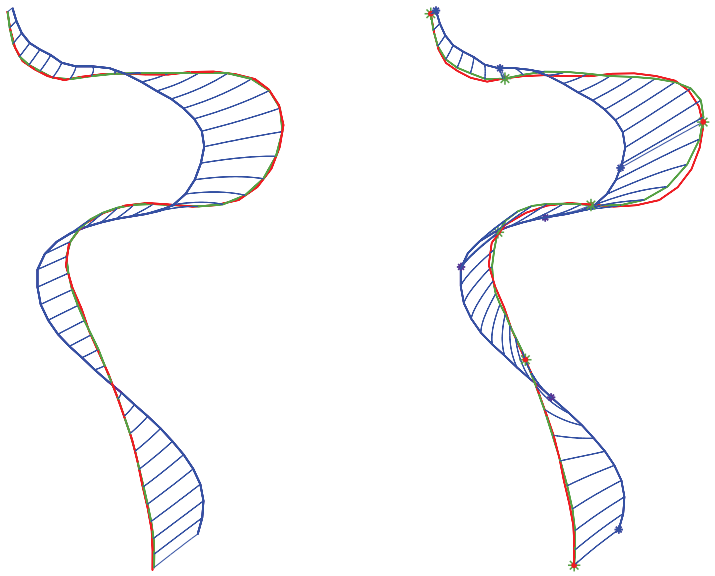

(a) $D = \rho(\phi_t) = 5.7$ **(b)** $D = \rho(\phi_t) = 6.8$

Figure 3.11: Diffeomorphic registration of source centerline (blue) to target centerline (red), with the registered centerline (green) and estimated distance D in shape space: (a) without ($E = E_{\text{cr}}$) and (b) with landmark matching term ($E = E_{\text{cr}} + E_{\text{lm}}$). (See color insert)

3.6 Evaluation methodology

In this section, the methodology applied for evaluating the elements of the geometric characterization pipeline is presented.

3.6.1 ICA classification performance

To evaluate the success of ICA-TB identification, 5-fold cross-validation (CV) was repeated 10 times and the estimated accuracy of correct classification was taken as the average CV success rate for all repetitions. To provide a better understanding of which are the most discriminating bifurcation features, we performed feature selection as a sequential forward selection (SFS). Starting with an empty set, at each forward (inclusion) step, the feature added to the feature subset is the one that maximizes the cross-validation (CV) classification rate.

3.6.2 Landmark detection

As the later geometric characterization is based on the landmarks, their detection has been extensively evaluated both qualitatively and quantitatively.

Qualitative evaluation

First, the carotid siphons were visually inspected to check whether they have been been partitioned into the four bends and that none of them were merged or split. Second, to evaluate the stability of the thresholds chosen for the four bends of the model, we displayed the probability densities of angles θ in (k_1, k_2) space (Fig. 3.8(a)) between curvature maximums that belonged to the true and false transitions.

Quantitative evaluation

The landmarks from the four-bend model attempt to reproduce the human intuition of where are the corresponding points representing bend transitions and their centers. As the model is just an approximation of objects having much larger anatomical variability, these points do not necessarily coincide with the curvature properties like the maximum and minimum. Thus, we considered expert observer as the best reference for identifying these corresponding points along the siphon. The reference landmark positions were obtained as the average across multiple observers of the manually placed ones. To evaluate the accuracy of the automatically determined landmarks we then computed:

- The *limits of agreement* of the automatically determined landmarks with the reference, which represent the 95% confidence interval of the differences [175] and are expressed as bias and standard deviation σ_{loa}.
- The standard deviation of the inter-observer variability σ_{o}, computed using one-way analysis of variance (ANOVA) [145].
- The variability index I, defined as the ratio of the above two standard deviations:

$$I = \frac{\sigma_{\text{loa}}}{\sigma_{\text{o}}}. \tag{3.17}$$

  If the value of this index $I < 1$, the landmarks from the automated method deviate from the reference less than the manually placed landmarks vary between observers.

3.6.3 Geometric quantification

The values of the computed geometric features (section 3.4) depend on the estimated landmark positions. Thus, we compared the values of features computed from automatically determined landmarks to the ones obtained with manually placed landmarks. Reference is taken to be the average of the values obtained from individual landmarkings by each observer. We then computed for each feature the variability index I (Eq. 3.17) and the normalized mean error computed as absolute error divided by the population range of values.

3.6.4 Shape similarity metric

The pairwise shape similarities also depend on the estimated landmark positions. We take the reference to be the shape distances obtained using the reference land-

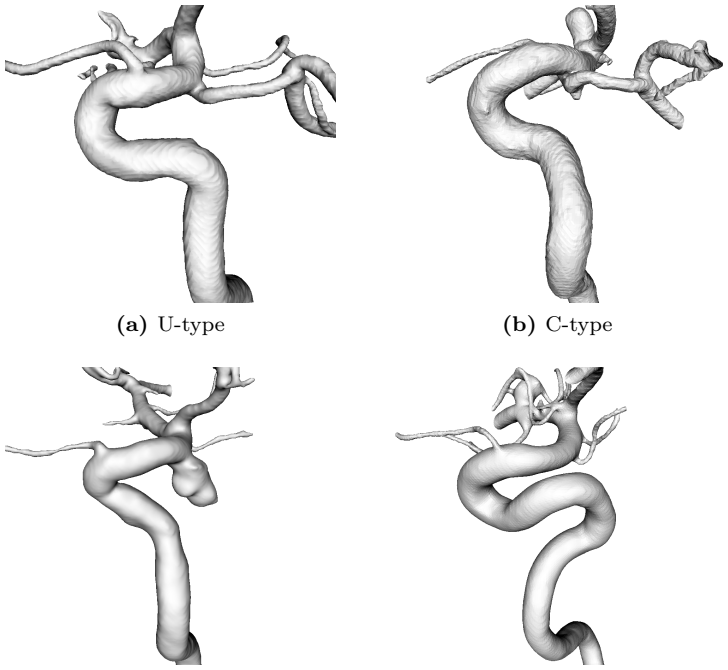

(a) U-type **(b)** C-type

(c) V-type **(d)** S-type

Figure 3.12: Examples of carotid siphon shape classes.

mark positions and enforcing the exact landmark matching during the registration process. Exact landmark matching is enforced by setting a high value to the weight γ_{lm} in Eq. 3.15. The distances based on automated landmarking were then computed with three different options for the landmark matching terms: no landmark matching, exact landmark matching, and the proposed inexact landmark matching. The limits of agreement with the reference for these three variants are computed and compared. In addition, we evaluated how different choices of the parameter σ_V, which defines the smoothness of the deformation field, affect the obtained distances and the matching residuals (Eq. 3.12).

3.6.5 Carotid siphon shape classes

To evaluate and compare the characterizations based on the proposed geometric features and LDDMCM, two clinicians labeled the class of siphon shape following the classification proposed by [157]. Such classification has been used in evaluating the vascular accessibility between the guide-catheter and the lesion [37]. Essentially, there are four shape classes: U, C, V and S (Fig. 3.12), with variation being mainly in the part of the anterior and the posterior bend. We then expect that the siphons characterized by the two proposed schemes will cluster by classes i.e. the siphons belonging to the same class will have similar geometric features and small LDDMCM distance to each other.

The following steps were then performed. First, we applied dimensionality reduction to map all the carotid siphons to an Euclidean submanifold. Principal Geodesic Analysis (PGA) [176] is applied on the geometric features as they are composed of a mixture of features in $\mathbb{R}^+$ (radii and lengths), SO(2) (angles), and S^2 (normal vectors). Each normal vector is treated as a single feature, having two degrees of freedom. Similarly, for LDDMCM, classical multidimensional scaling (CMDS) [177] is applied. We performed two dimensionality reductions. One to 2D, for the purpose of visualizing and qualitatively evaluating the achieved clustering. The other, to a smallest dimension still preserving the 99% of the total data variance, for the purpose of quantitative evaluation as a classification success rate of a linear classifier. In the obtained submanifold, we trained a classifier using linear discriminant analysis (LDA) and leave-one-out cross-validation classification rate is reported as a measure of how well separated the four classes are. Finally, we looked at the LDDMCM classification performance for different choices of σ_V while for the characterization based on geometric features we performed SFS of features to identify the most relevant ones.

3.7 Results

The geometric characterization pipeline was retrospectively applied to 96 images acquired with 3DRA, from 86 patients (age range: 33−76, mean age: 53 years, 74% women). Contrast was injected to enhance the vessels comprising anterior cerebral circulation of either left (43) or right (53) hemisphere (10 patients had both sides imaged). Acquisitions were performed with an angiographic unit: Allura Xper FD20 (Philips Healthcare, Best, The Netherlands). On a dedicated workstation, 3D images were reconstructed with a 256^3 matrix having a voxel size of $0.29 \times 0.29 \times 0.29$ (mm). All images were successfully segmented and had their vascular tree centerlines and topology extracted.

3.7.1 ICA classification performance

From all 96 vascular trees, the feature vectors of 297 bifurcations along ICA were manually labeled as "terminal" (96) or "non-terminal" (201), and supplied to SVM classifier for training and cross-validation (CV) (Fig. 3.13). Feature selection revealed that the two features that contributed the most to the ICA-TB discrimination were: *ratio of mean radii between the smaller and the larger daughter branches* and *axial component of the smaller daughter branch vector*. At peak CV rate (6 selected features) ICA-TB was misclassified in only one case (99% success) rate, producing one false positive and zero false negatives (99.5% specificity and 100% sensitivity). The false positive sample was the only example available of a bifurcation of ICA with a tentorial marginal branch, hence during its testing none were present in the training data. The results show that the chosen features describe adequately the bifurcation.

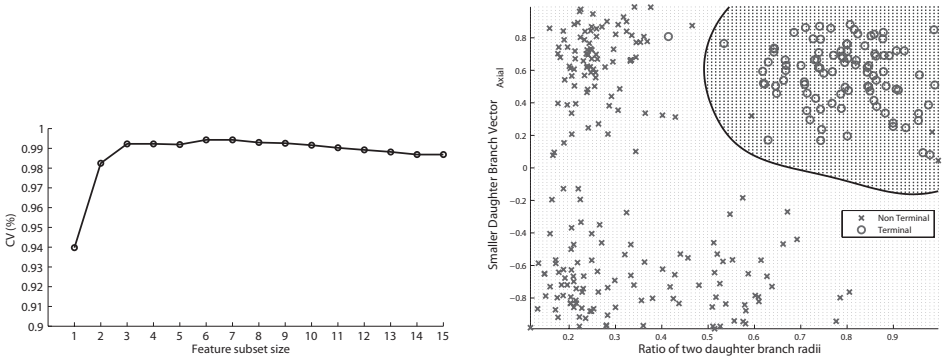

Figure 3.13: Classification of ICA-TB with SVM. (a) Cross-validation (CV) classification rates for sequential forward selection of features. (b) Example of classification in 2D feature space where the two features chosen were the ones giving the highest CV rate. The classifier trained in this 2D space misclassified one terminal and three non-terminal vectors (In 6D space there is only one non-terminal misclassified).

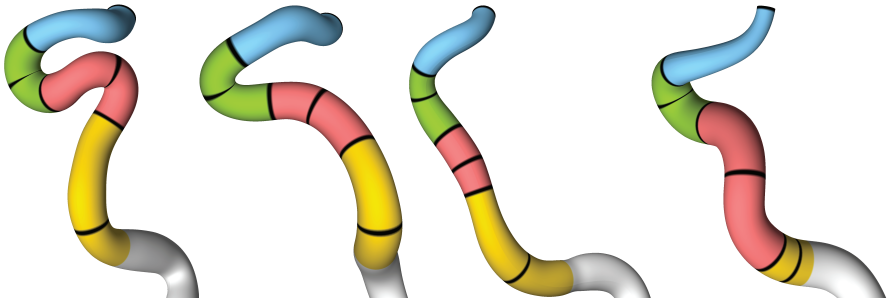

Figure 3.14: Automated landmarking examples:(a-c) Successful cases. (d) A case where the posterior and the inferior bend were merged into one ($\theta_{\text{post-inf}} = 40°$). (See color insert)

3.7.2 Landmark detection

Qualitative evaluation

Detection of landmarks for partitioning the carotid siphon into bends failed in three cases (97% success rate) (Fig. 3.14). Failure occurred mostly when the transition between the posterior and the inferior bend was missed due to small angle between vectors in (k_1, k_2) space ($\theta < \alpha_{\text{post-inf}} = 45°$, Fig. 3.14(d)).

Evaluation of threshold stability is shown in Fig. 3.15. Of the four thresholds, the $\alpha_{\text{ant-post}}$, $\alpha_{\text{inf-end}}$ are the more stable ones, as they separate two distributions tightly grouped around their means. We can observe that any choice of $\alpha_{\text{ant-post}}$ in the range of $[40^o - 80^o]$ would produce the same results. Choice of $\alpha_{\text{post-inf}}$ and $\alpha_{\text{ant-sup}}$ is more critical but given that they were evaluated on a large number of cases, a good generalization is expected.

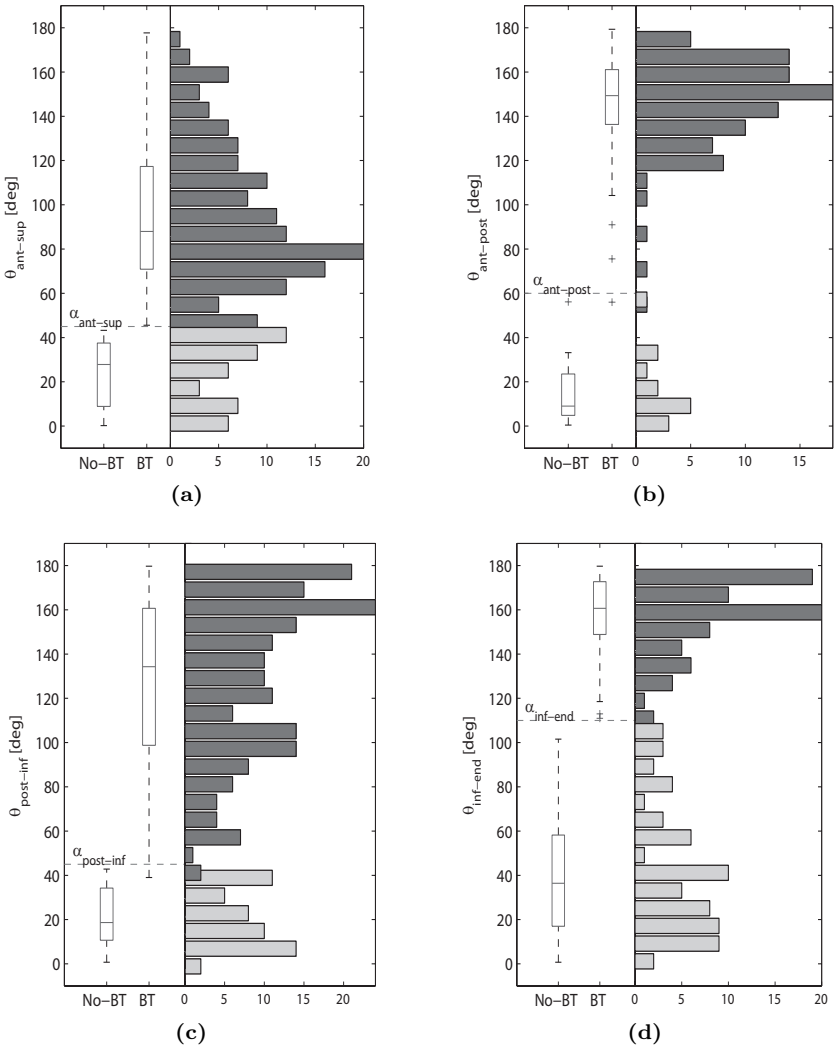

Figure 3.15: Distribution of angles in (k_1, k_2) space that present bend transition (BT) and non-bend transition (No-BT), in a form of a box-plot and histogram. (a) anterior-superior, (b) anterior-posterior, (c) posterior-inferior, (d) inferior-end.

Quantitative evaluation

Three observers manually placed the landmarks on sequentially chosen subset of 50 cases. The results are shown in Fig. 3.16. The transition between the superior and the anterior bend (L1) has the largest localization error in both bias and standard deviation. However, this is the location with the largest inter-observer variability as well. For other landmarks, either the bias is not statistically significant or the variability is within 50% of the inter-observer one. The central landmarks (L2, L4, L6) are particularly well detected with no significant bias and the deviation from

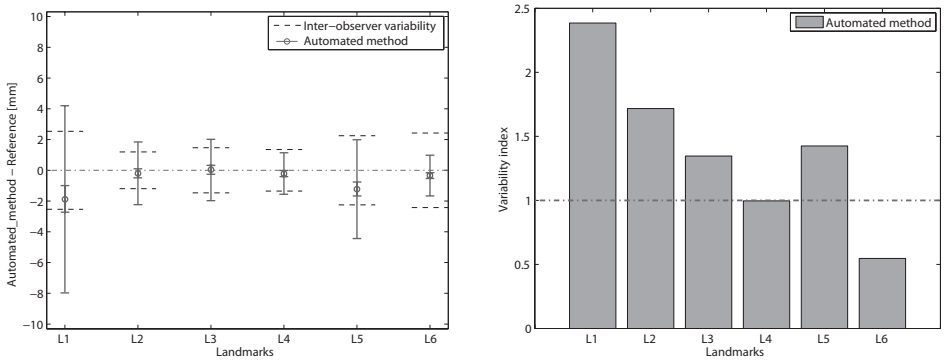

(a) **(b)**

Figure 3.16: (a) Limits of agreement between automated landmarking and the reference. Bias is denoted with a marker and 95% confidence interval, while the bars correspond to 95% limits of agreement ($\pm 2\sigma_{\text{loa}}$). Agreements are compared with inter-observer limits of agreement for the manual measurements (b) Variability index for each landmark. Landmarks are ordered from distal to proximal: superior-anterior (L1), central anterior (L2), anterior-posterior (L3), central posterior (L4), posterior-inferior (L5) and central inferior (L6).

the reference being below the inter-observer one for the posterior and the inferior bends.

3.7.3 Geometric quantification

The evaluation results for the total set of geometric features is shown in Fig. 3.17. We can observe that all the features have $I < 1.8$ and normalized mean absolute error below 8% with more than half of them having $I < 1.3$ and error less than 3%. Thus, we can assume that landmark localization is sufficiently accurate not to affect the computed geometric features.

3.7.4 Shape similarity metric

For the registrations using inexact landmark matching, previously evaluated σ_{loa} (Fig. 3.16(a)) of each landmark's limits of agreement are used to normalize corresponding Euclidean distances ($\sigma_n = \sigma_n^{\text{loa}}$) in Eq. 3.14. Thus, the larger the landmark's discrepancy from the reference, the smaller is its influence during the registration.

The parameters γ_{cr} and γ were experimentally set to $\gamma_{\text{cr}} = 1$ and $\gamma = 0.1$, for all registrations. Observing the effect of the parameter σ_V on the registration results, for large σ_V (> 6 mm), due to strong smoothness constraint on the deformation, the final matching precision deteriorates. At such scales, the deformation is not accounting for the details that we consider to be part of the difference in geometry as opposed to noise. Small σ_V (< 1 mm), allows highly irregular speed fields and nearby regions start to move independently. The obtained distance is not representative of the one in the shape space and the registration optimization is likely to end in a local minimum. The analysis (Fig. 3.18) confirms this observation.

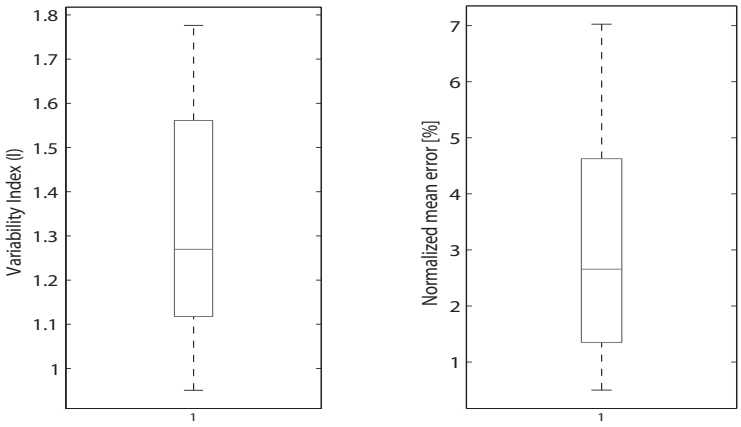

Figure 3.17: Boxplot for geometric features, showing the distribution of: (a) variability index and (b) normalized mean error. Boxes span the lower (higher) quartiles and whiskers extend up to 1.5 the inter-quartile range.

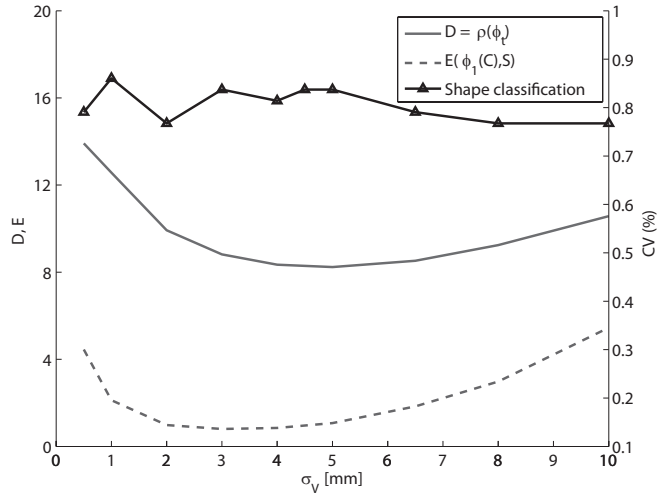

Figure 3.18: Sensitivity to the parameter σ_V of: The distance D, the matching residual E after the registration with inexact landmark matching (average curves across pair-wise registrations), and the cross-validation (CV) siphon shape classification rate.

The values of σ_V from the range $[1, 6]$ produce small matching error and the optimal choice depends on a priori assumptions and the final application. We chose $\sigma_V = 4.5$ mm, which is the scale of the average vessel diameter. This choice is later reevaluated for the application to siphon shape classification.

For the inexact landmark matching, to find γ_{lm} we took a small sample of the first 10 cases and used it as a training set. Then, the sweep search with $\gamma_{\mathrm{lm}} = \{2^{-3}, \ldots, 2^3\}$ was performed and the value that produced the best agreement with

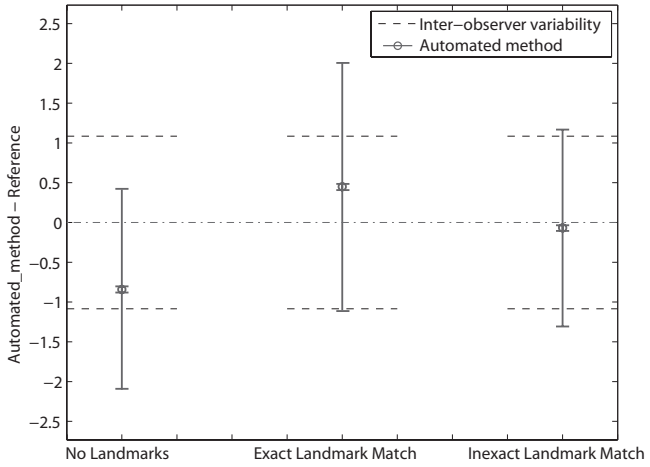

Figure 3.19: Limits of agreements of distances based on automated landmarking with the reference distances. Results for LDDMCM with the three types of landmark matching terms are shown: None, exact and inexact.

the reference was used ($\gamma_{\text{lm}} = 1$).

To compare the results with the three different landmark matching terms, the distances based on automated landmarking were then computed with: no landmark matching ($\gamma_{\text{lm}} = 0$), exact landmark matching ($\gamma_{\text{lm}} = 100$), and the proposed inexact landmark matching ($\gamma_{\text{lm}} = 1$). The limits of agreement with the reference for these three variants are shown in Fig. 3.19. We can observe: First, that using landmarks is important as otherwise the obtained similarity distances are underestimated. Second, using the proposed inexact landmark matching showed improvements in terms of smaller bias and standard deviation compared to enforcing exact landmark matching, since any inaccuracies in landmark localization influence less the registration process. The distances obtained with inexact landmark matching had the variability index $I = 1.1$, which is close to the variability obtained with the manual landmarking.

3.7.5 Carotid siphon shape classes

As many siphons had ambiguous shape, only the ones where both clinicians agreed on the shape class were used (43 cases). The first step in the evaluation is the dimensionality reduction and we look at the residual variances as a measure of the obtained statistical fit (Fig. 3.20(a)). Residual variance is defined as $1 - R^2$, where R is the correlation coefficient between the pairwise point distances in a subspace and the original space. We can observe that the items with characterization based on the LDDMCM can be better represented in a low dimension ($< 5D$) than the ones characterized by the geometric features. For other dimensionality reductions, both characterizations produce similar residual variances and the more dimensions used, the better the statistical fit.

Observing, the items mapped to a 2D Euclidean submanifold (Fig. 3.20(b) and (c)), LDDMCM appears to produce more discriminating clusters than the

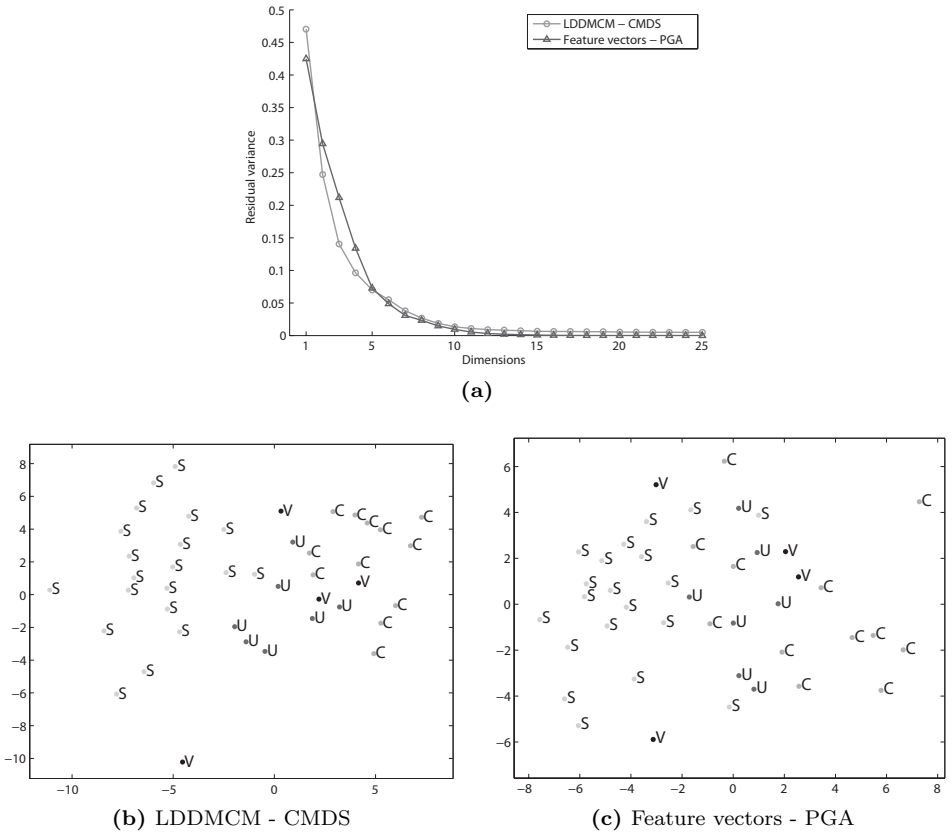

(a)

(b) LDDMCM - CMDS

(c) Feature vectors - PGA

Figure 3.20: Dimensionality reduction to a submanifold. (a) Comparison of residual variances after dimensionality reduction. (b,c) Items mapped to a 2D Euclidean submanifold, with labels denoting siphon shape classes.

geometric features. This is confirmed by the classification of labeled items mapped to a 12-dimensional submanifold (where residual variance for both approaches is negligible), as there $CV_{\text{LDDMCM}} = 84\%$ while $CV_{\text{Feature}} = 63\%$. To further evaluate the importance of using landmark matching in the registration process, we computed the CV rate for the results obtained without the landmark matching term: $CV_{\text{LDDMCM\_no\_landmarks}} = 77\%$, which produced worse class separability than the proposed method.

LDDMCM classification for different choice of σ_V parameter (Fig. 3.18), shows that the performance is very stable in the range $[3, 5]$ mm, and still quite stable (77%-86%) in the entire evaluated range $[0.5, 10]$ mm. The results of geometric feature selection are shown in Fig. 3.21. Using the feature selection improves the CV rate and the peak $CV_{\text{Feature}} = 77\%$ is reached already with four features. The four features in the order of importance were: *tortuosity*, *normal vector of the anterior bend's osculating plane*, *length of the anterior bend* and the *bending radius of the anterior bend*. This is in good agreement with the visually observed variability of shape types, which is mostly due to the change in the geometry of

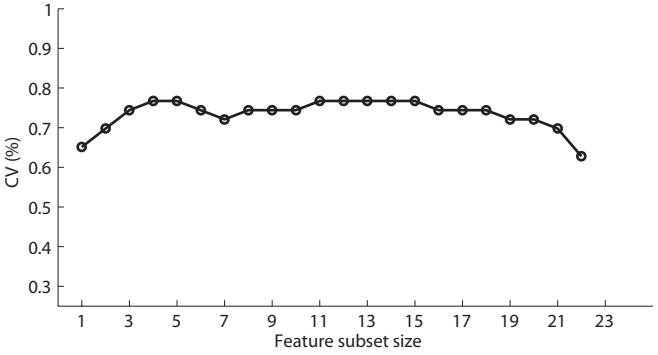

Figure 3.21: Siphon shape classification: Cross-validation (CV) classification rates for sequential forward selection of geometric features.

the anterior and the posterior bends.

3.8 Discussion

We presented a pipeline for extensive geometric characterization of carotid siphon. Starting from angiographic image the pipeline identifies and extracts the centerline and radius of the ICA. On the extracted centerline we automatically detect anatomical landmarks of the region of interest corresponding to carotid siphon, which are prerequisites for the proposed geometric characterization. Landmarks as points of anatomical correspondence are used for computing both: geometric features and LDDMCM shape similarity.

The method to identify ICA from a vascular tree by detecting ICA-TB had a high classification success rate (99%). Looking at the two most discriminative features: *ratio of mean radii between the smaller and the larger daughter branches* and *axial component of the smaller branch vector*, the classifier learned that ICA-TB branches into two similarly big vessels as opposed to a narrow side vessel and also that the smaller branch vector (corresponding to ACA) is pointing towards the top of the head.

One of the main elements of this work was automated landmark detection as it is essential for later characterization. Landmarks were associated to the four bend model of the carotid siphon. Apart from the superior bend, the other three bends were modeled as planar. An alternative would be to split the superior bend into two smaller quasi-planar bends, but we observed that those two bends are not consistently present between subjects. Direct application of the bend detection method by [158], which uses curvature and torsion centerline profiles, was not suitable as it does not assure bend correspondences and the results are sensitive to the applied centerline smoothing scale. Thus, a more robust method, based on the curvature vector expressed in the parallel transport frame is proposed.

Landmarks are essential for geometric features as they define, in an automated and consistent manner, the corresponding regions of interest for local and global features. They are crucial for computing LDDMCM as they assure anatomically

correct registrations. The validation study showed that the automatically obtained landmarks are in agreement with the ones selected manually and that they do not affect the obtained geometric quantities or LDDMCM distances with respect to manual landmarking. Using automated approach avoids observer variability and enables high reproducibility among a set of individuals, which is imperative in performing robust population studies.

The presented set of geometric features were selected from typical geometric quantities used in the literature, known to affect hemodynamics. In general, they should be defined and selected in accordance to the hypothesis one is testing. Characterization based on geometric features and LDDMCM are two complementary approaches. The former has the advantage that any observed associations or variabilities of features are straightforward to interpret. The later quantifies shape differences directly hence is more effective in capturing subtle changes in geometry but its interpretation is more abstract. Both approaches avoid the need for any point correspondences, apart from the sparse set of anatomical landmarks.

The explanatory power of the characterization was evaluated by observing the discrimination of siphon shape classes in the submanifold coordinates, seen as modes of anatomical variation of population. The characterization based on LDDMCM proved better in classifying the carotid siphon shape classes than the one based on geometric features. These shape classes already have direct clinical relevance in selecting the endovascular treatment strategy, but they could be replaced by any other clinical condition of interest, e.g. presence of aneurysm or its rupture status. Then, insights about the relation of the geometry of carotid siphon with its clinical condition could be obtained and automatically quantified in a large population.

The proposed methodology has limitations. As we assume all carotid siphons can be modeled with the four bends, the landmarking fails when two neighboring bends are perceived as one large bend. In our database, this assumption was rarely violated (3%). In general, the method could be extended to learn the geometric properties of the bends, to detect unrealistic (unprobable) solutions. Regarding the computation of LDDMCM similarities, the drawback of the registration metric is that it is not symmetric with respect to the source and target curves. Thus, the resulting shape distance was taken as the mean value from the two registrations. In addition, adding a new case requires registering it with all the cases from the database. For a limited size database, like ours, this is not a problem, as the registration of spatial curves is generally much faster than the registration of volumetric images. In the case of larger datasets, a low-dimensional manifold could be first learned from a set of curves used as a training set. Then, each new centerline curve would be projected directly on the manifold, as similarly presented for brain images in [178].

3.8.1 Conclusions and outlook

Geometry of carotid siphon has a large variability across subjects, which makes it a good candidate to be a potential risk factor for the onset of vascular pathologies on and off the ICA. We have presented a complete and automated pipeline for geometric characterization of the carotid siphon. The proposed approach, based

on anatomical landmarks, enables the analysis through a set of geometric features and LDDMCM shape similarities.

Some elements of the proposed pipeline are new and represent contributions in themselves. In this sense, the main contributions of developed in this chapter are the following:

- Algorithm for the automated identification of ICA-TB and its discriminating features.
- Algorithm for the automated detection of vessel bends based on the curvature vector expressed in the parallel transport frame and its application to anatomical landmarking of carotid siphon.
- Definition and computation of geometric quantities like angles of rotation between osculating planes of consecutive bends, having a known influence on hemodynamics.
- The use of LDDMCM similarity metric for vessels and the importance of using the inexact landmark matching to obtain anatomically valid deformations.

Although the methodology is tuned to carotid siphons, it is applicable to other vessels. The classifier used for the identification of ICA can be extended to detect more bifurcations for the purpose of anatomical labeling of the vascular tree and this is currently under study. The bend identification algorithm and the geometric quantities defined on them are generic and can be applied to any vessel (e.g. aorta, coronaries or peripheral arteries) or tubular structure. However, the number and the type of bends might not be as consistent along the population as they are for the carotid siphon. In that case, classical LDDMCM, without the landmarks, can be used as a shape similarity metric and the number of bends can then become a geometric feature in itself.

The presented characterization is the first step in the pursuit of geometric risk factors of carotid siphon. Identifying these factors was not the aim of this work, but will form part of the future one. In addition, the techniques used here will be extended to a more distal level, in an effort to characterize the complete Circle of Willis.

4

Anatomical Labeling of the Circle of Willis using Maximum A Posteriori Probability Estimation

This chapter presents anatomical labeling of the cerebral arteries forming the CoW. This enables inter-subject comparison, which is required for geometric characterization and discovering risk factors associated to cerebrovascular pathologies. We present a method for automated anatomical labeling of the CoW by detecting its main bifurcations. The CoW is modeled as rooted attributed relational graph, with bifurcations as its vertices, whose attributes are characterized as points on a Riemannian manifold. The method is first trained on a set of pre-labeled examples, where it learns the variability of local bifurcation features as well as the variability in the topology. Then, the labeling of the target vasculature is formulated as maximum a posteriori probability (MAP) estimate where the likelihood of labeling individual bifurcations is regularized by the prior structural knowledge of the graph they span. The labeling method is able to handle graphs with a cycle and multiple roots. It was evaluated by cross-validation on 50 subjects, imaged with magnetic resonance angiography, which showed that 95% of bifurcations were correctly identified. In addition, besides providing MAP, the method ranks the labelings. The proposed method can naturally handle anatomical structural variability and is demonstrated to be suitable for labeling arterial segments of the CoW.

The content of this chapter is adapted from the following publication:

H. Bogunović, J.M. Pozo, R. Cárdenes, L. San Román, and A.F. Frangi. Anatomical Labeling of the Circle of Willis using Maximum A Posteriori Probability Estimation. *submitted*.

4.1 Introduction

The Circle of Willis (CoW) is a ring of cerebral arteries, located at the base of the brain, that connects the left and right anterior circulation with each other and with the posterior one, enabling a source of collateral flow in case of vascular occlusions [5]. It is also known to be a common site of pathologies, in particular of cerebral aneurysms (pathological dilations of blood vessels) [9] whose rupture can result in a subarachnoid hemorrhagic stroke, which is fatal in up to half of all the cases [3].

Many variants of CoW configuration exist, in which certain arteries are hypoplastic (very thin), missing, or duplicated [179, 180]. The standard, complete and symmetric CoW is estimated to be present in only $40 - 50\%$ of the healthy population [7, 8]. These anatomical variations in the CoW affect the volume flow rates in the feeding arteries [32]. In [34], the incidence of CoW variations was found to be significantly higher in the aneurysm series than in the control circles without aneurysm. Specifically, the asymmetry of the circle was found to be correlated with the presence of aneurysms. This led to the hypothesis that geometric variation of the CoW, by altering the hemodynamic forces, plays a role in the development and rupture risk of cerebral aneurysms [34, 181].

Understanding what constitutes the normal geometric variability of CoW and what are the deviations associated with cerebrovascular pathologies is hence important and is currently still not clear. Analyzing the statistical variation of the geometry of the arteries and bifurcations constituting the CoW can lead to the identification of *geometric risk factors* [21, 31] for the onset and progress of vascular pathologies in general. To be able to register and compare CoW of different subjects, the anatomical correspondence between vascular segments, known as *anatomical labeling*, has to be established. Manual anatomical labeling is a tedious and time consuming task. Thus, automating it becomes crucial for streamlining the geometric characterization of a large number of cases.

In particular, we are interested in anatomical labeling of the main arteries of CoW and the bifurcations connecting them (Fig. 4.1), where 90% of all the cerebral aneurysms occur [9]. These are the following. Internal carotid artery (ICA) which branches into anterior cerebral artery (ACA) and middle cerebral artery (MCA). MCA is of interest up to its principal bifurcation, which divides it into the M1 and M2 segments. Two anterior trees are connected with anterior communicating artery (AcoA), which splits the ACA into A1 and A2 segments. The anterior trees are connected to the posterior tree via posterior communicating arteries (PcoA). The posterior tree is formed by the basilar artery (BA) from which left and right posterior cerebral arteries (PCA) branch, and are further split into P1 and P2 segments by PcoA. To the set of eleven bifurcations that connect these arteries, throughout the text, we will refer to as *bifurcations of interest* (BoI).

In this work, we present a method for automated and robust classification of blood vessel bifurcations, which we applied to the task of anatomical labeling the CoW. The proposed method formulates the labeling of bifurcations as maximum a posteriori probability where:

- Likelihood term is based on local geometric characterization of bifurcations.

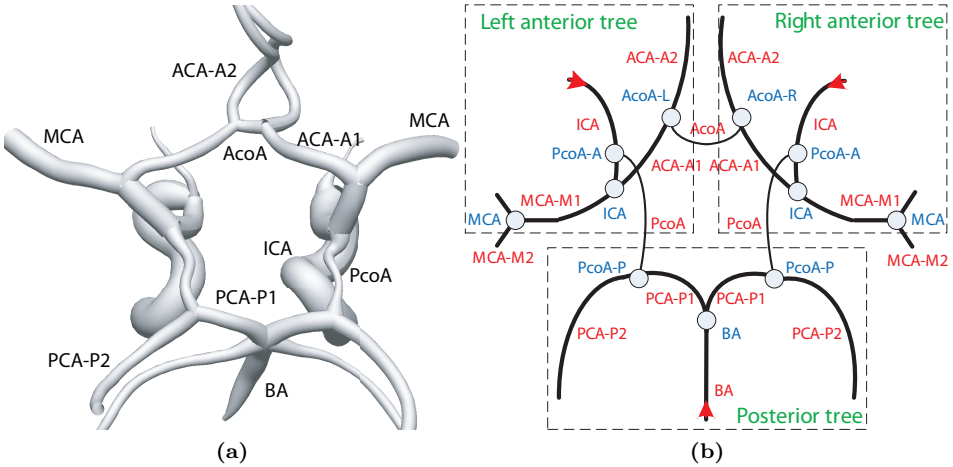

Figure 4.1: Anatomy of the Circle of Willis. (a) Surface rendering. (b) Schematic representation: The arteries (in red), the inflow (arrows), and the bifurcations of interest (in blue). Notation: '-A' denotes anterior, '-P' posterior, '-L' left and '-R' right. (See color insert)

- Prior term accounts for their connectivity and topological relationship.

The method was designed to satisfy the following main requirements: 1) handle inter-subject variability in the topology and the number of BoI present; 2) be robust to the presence of spurious branches coming from small side-branches and segmentation imperfections; 3) be able to identify BoI as part of higher order furcations; and 4) learn from newly labeled examples and improve with time. This represents an extension to the complete CoW of our previous work [182], which was focused on the anatomical labeling of the single anterior circulation trees only, hence avoiding the presence of circle and multiple roots.

The rest of the chapter is organized as follows. In section 4.2, we overview the related work in anatomical labeling of 3D tubular structures. Section 4.3 presents the workflow of the proposed methodology. Evaluation on a set of 50 magnetic resonance angiography (MRA) images is presented in section 4.4. Finally, section 4.5 discusses the advantages and limitations of the proposed method and concludes the chapter.

4.2 Related work

Anatomical labeling and anatomical matching are two related but different problems. In anatomical matching, the correspondence is sought between a pair of anatomical structures. It is normally designed for intra-patient comparison, and it assumes that the structure and/or geometry is relatively stable between the two acquisitions. Examples are the anatomies obtained from intra-patient follow-up [183–185], before and after treatment [186], from different modalities [185, 187] or different phases of the breathing cycle [188, 189].

Anatomical labeling is a broader problem, where emphasis is on establishing correspondences across a population. It can be seen as a matching of an unlabeled case to an *atlas*, represented by a knowledge base of population average and the geometric and structural variability. One labeling approach is to use a pair-wise matching algorithm to match the unlabeled case with one or multiple labeled examples and then transfer the labels from the corresponding points of the best match or combine the matches in a voting scheme. Such approaches were applied for human airway tree data labeling [190–192]. However, the reported success rates were generally lower than the atlas-based ones, described next.

Automated anatomical labeling of 3D tubular structures in general has already attracted interest in the past. Especially the labeling of airway trees [94, 193, 194] as its geometry is linked to a progression of a variety of respiratory diseases. The seminal work was done by Tschirren et al. [94]. They match branchpoints of a target airway tree to the labeled reference tree, representing population atlas. Atlas is built from a training set of airway trees and is represented by the mean and standard deviation values of geometric and topological features. The two trees are matched using weighted association graph where the weights are probability-like estimates of single and inter-branch features. The maximum weighted clique then corresponds to the best match.

Van Ginneken et al. [193], studied the distributions of several branch characteristics in a population of airway trees: orientation, average radius, and angle with the parent segment. Assuming independent normal distributions they obtain probabilities for assigning particular label to a branch. Labels are then assigned in a recursive manner, starting from the root (trachea), where the final probability that a particular label should be assigned is conditioned on those of its children and grand children. No further methodological details are given and it does not handle the main anatomical variations.

Mori et al. in a series of works [194–196] developed knowledge-based framework for anatomical labeling of airway tree branches based on machine learning and combination optimization. Each branch is modeled as a straight line and described with a set of geometric features to train the AdaBoost classifier. Thus, for each branch of the target tree the classifier provides the likelihood of having a certain label. Then, the combination of branch labels yielding the maximum total likelihood is selected. However, their method uses rigid topological constraints and does not seem to be robust to large anatomical variations in the topology.

In general, airway trees are characterized by many similar bifurcations connected by short straight branches. Furthermore, one branch bifurcates into two branches of approximately the same size and anatomical name changes at every bifurcation. This makes the methods designed for them difficult to apply directly to the task of labeling blood vessels which are long and tortuous and can span over many bifurcations with smaller side branches.

Mori et al. [197] tuned their approach to a specific task of labeling abdominal arteries, where many thin arteries branch from the thick ones. They describe a branch with six geometric features. Each branch is modeled with multivariate Gaussian distribution which is then used to obtain label likelihood for a given test branch. The branch-label combination that gives maximal likelihood (ML) under anatomical constraints is selected. Unfortunately, the method is anatomy

Table 4.1: Overview of the state of the art methods in anatomical labeling of 3D tubular structures.

Reference	*Anatomy*	*Modality*	*# cases*	*# anat. labels*	*Accuracy rate*
Tschirren et al. (2005) [94]	Airways	CT	17	32	97%
Bulow et al. (2006) [190]	Airways	CT	6	34	40-69%
van Ginneken et al. (2008) [193]	Airways	CT	36	32	90%
Mori et al. (2009) [194]	Airways	CT	90	≈ 30	86.9%
Mori et al. (2010) [197]	Abdominal arteries	CTA	89	11	84.2-88.8%
Feragen et al. (2011) [191]	Airways	CT	20	34	83%
This work	Circle of Willis	MRA	50	11	95%

specific as it divides the tree into four specific regions and for each region different geometric features of abdominal arteries are used.

To the best of our knowledge, automated anatomical labeling of the complete CoW has not been attempted in the past. The closest works related to matching or labeling cerebral arteries, besides our previous effort [182], are the ones of Tang and Chung [198], and Uchiyama et al. [199]. In [198], they propose a pair-wise matching algorithm that is based on combinatorial optimization strategy to compute the approximated tree edit distance (node delete and insert costs) between two anterior circulation trees obtained with 3D rotational angiography (3DRA). Their results are verified only qualitatively on a pair of synthetic structures and a pair of 3DRA data. In [199], they first rigidly register a target MRA image to the labeled reference image. Then the target arterial regions were classified into eight classes by assigning the closest label from the reference image. They label entire artery regions rather than individual arteries. Furthemore, the method's sensitivity to the choice of the reference image is not clear.

Table 4.1 summarizes the results of the above methods. Typical evaluation method used was leave-one-out cross-validation, where in an iterative scheme, one case is used for testing, and the others are used as the training set. All of the methods were designed to label structures which have a topology of a tree. In that respect, the problem of labeling CoW is special, since the arteries form a graph containing a cycle and there are multiple roots.

4.3 Methodology

4.3.1 Preprocessing: from angiographic image to vascular model

As a preprocessing step for labeling, a vascular model needs to be extracted from an angiographic image. As arteries have near-circular cross-section they can effectively be modeled (represented) with their centerline and a local radius at each point [93]. Segmentation and skeletonization of the vasculature can, in principle, be done with a variety of methods, as reviewed in [72, 73]. We used the following approach.

Vessel centerlines are extracted as intensity ridges in MRA images using the method of [90], available within the open-source TubeTK toolkit [200]. From a set of points distributed on the image, the method is able to locate the nearby ridges and track them. This results in a series of centerlines, but with many being disconnected. In order to connect the centerlines, from each centerline end-point we start a fast marching with underlying image intensity as a speed function, until another centerline object is reached. We then backtrack using local gradient direction to obtain the minimal cost path that connects the two centerlines [201]. This provides us with a skeleton representation of the underlying vasculature.

To obtain the blood vessel radii, from the skeleton we start automated lumen segmentation using the level set based on geodesic active regions [78], which was demonstrated to be accurate for 3DRA and time-of-flight (ToF) MRA images [164]. Potential problem of two nearby blood vessels merging into one is avoided by using topology preserving evolution [202]. As in the level set method the segmented surface (lumen) is implicitly represented with a distance map, at the end of the evolution (Fig. 4.2(a)), the distance value at every skeleton point corresponds to the radius of the maximal inscribed sphere.

The skeleton represents a graph, where edges correspond to the individual blood vessels, while the vertices to the bifurcations and the loose vessel ends (vertices of degree one) (Fig. 4.2(b)). The edges describe vessels with a sequence of points (x_i, y_i, z_i, r_i), where x_i,y_i,z_i are the coronal, sagittal and axial coordinates of the centerline, respectively, and r_i is the radius.

The CoW can be viewed as three separate rooted trees: anterior left and right, and the posterior one; mutually connected by communicating arteries (Fig. 4.1(b)). The three root vertices that correspond to the points where the blood flow enters the imaged field of view are identified as the vertices (of degree one) on the lowest axial plane, with a sufficiently large radius ($r > 1$ mm). Ordering them by the sagittal component, posterior root of BA is positioned in between the left and right anterior roots of ICAs.

The anatomical variability of CoW is related to the presence/absence of the three communicating paths between the trees. Based on that, we define eight different high level structure types $\{\mathrm{ST1}, \ldots, \mathrm{ST8}\}$ (Table 4.2 and Fig. 4.6). To obtain insight into this underlying structure type of the extracted graph, we observe the mutual reachability of the three roots. If all the roots are mutually reachable, to additionally detect whether the CoW is complete, we search for the cyclic paths in the graph. To discriminate potentially erroneous cycles due to

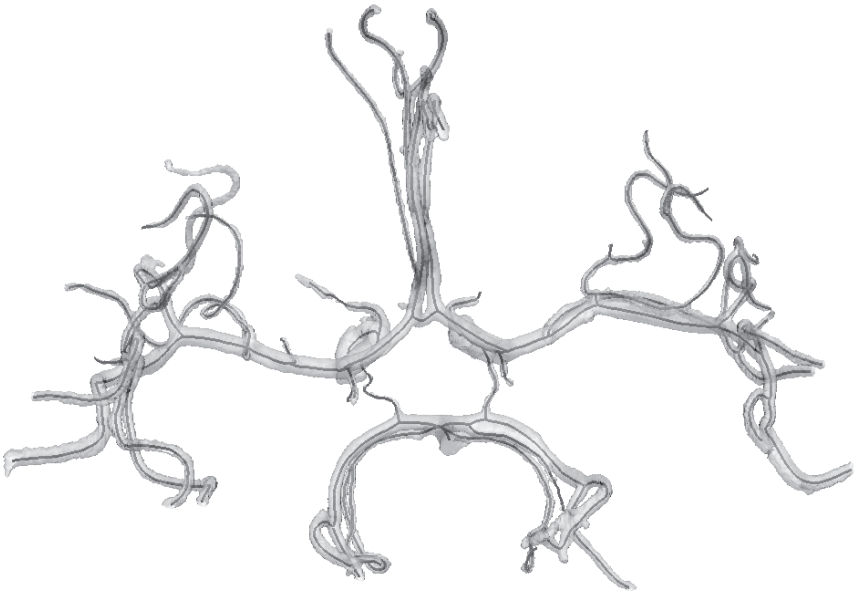

(a)

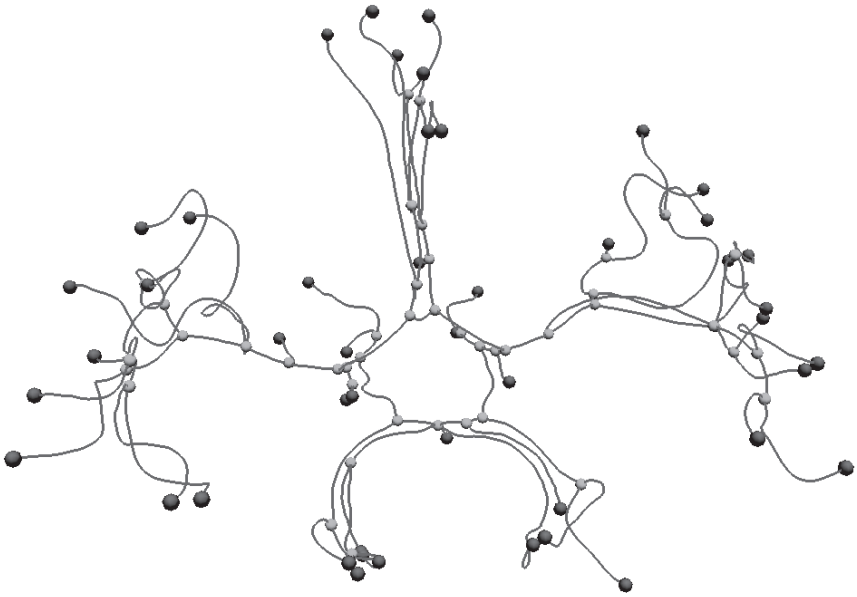

(b)

Figure 4.2: (a) Skeleton and segmentation of region of the Circle of Willis. (b) Skeleton represented as a graph with edges and vertices (bifurcations in light gray, loose ends in dark).

connectivity error, to qualify as the CoW cycle the three roots have to connect to the cycle at three different vertices (Fig. 4.1). If more such cycles are found, the shortest length one is selected, as erroneous connections are more likely to appear

Table 4.2: Graph structure types and their following properties. The presence of communicating paths between the trees: anterior communicating path (AcoP), left posterior communicating path (LPcoP) and right posterior communicating path (RPcoP); the mutual reachability of the three roots: left-right (LR), left-posterior (LP), and right-posterior (RP); the presence of the CoW cycle.

Type	*Description*	*Communicating Paths*			*Root Reachability*			Cycle
		AcoP	LPcoP	RPcoP	LR	LP	RP	
ST1	Three isolated trees	0	0	0	0	0	0	0
ST2	Left ant. tree isolated	0	0	1	0	0	1	0
ST3	Right ant. tree isolated	0	1	0	0	1	0	0
ST4	Post. tree isolated	1	0	0	1	0	0	0
ST5	Connected via post. tree	0	1	1	1	1	1	0
ST6	Connected via right ant. tree	1	0	1	1	1	1	0
ST7	Connected via left ant. tree	1	1	0	1	1	1	0
ST8	CoW complete	1	1	1	1	1	1	1

deeper in the vasculature. From such observations we can then identify directly 5 out of 8 structure types, with ambiguity remaining between ST5, ST6, and ST7.

4.3.2 Labeling as maximum a posteriori probability

The task of anatomical labeling is posed as identifying the BoI (defined in section 4.1), on the extracted vascular model. The paths connecting the BoI then identify the blood vessels of interest. Identifying bifurcations, rather than vessels directly, has several advantages. First, as a vessel can have several side-branches, finding its start and end bifurcations makes the method robust to the presence and the number of such real or artifact side-branches. Second, geometric features of bifurcations synthesize better the underlying vasculature since they contain information of several branches at a specific location.

Extracted vascular model is formally considered as rooted Attributed Relational Graph (rARG).

Definition *Rooted Attributed Relational Graph* is a quadruple $\hat{G} = (V, E, A, R)$, where $G = (V, E)$ is an undirected graph with the vertex set V and the edge set E, R is the set of root vertices, and A is the set of unary vertex attributes $A : V \to F$, with F being the space of vertex features.

In the case of G containing the CoW cycle, the three vertices where the roots connect define the cycle's *joining vertices* o_k for $k \in \{1, 2, 3\}$. In addition, each root $r_k \in R, k \in \{1, 2, 3\}$ defines an orientation within the set of ordered vertex pairs $S(r_k) \subset V \times V$, where $(v_i, v_j) \in S(r_k)$ iff there exists a simple path from

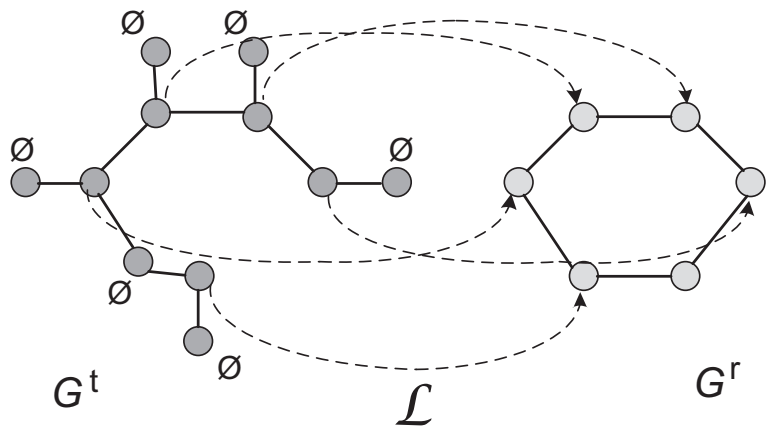

Figure 4.3: Example of a labeling $\mathcal{L}$ (dotted arrows) of a target graph G^{t} (dark gray) based on a reference graph G^{r} (light gray) with the bifurcations of interest. Vertices of both graphs can be left unmatched (denoted by ø on target graph).

r_k to v_j, passing through v_i, but not through any of its non-corresponding joining vertices $o_{k'}$ for $k' \neq k$. This associates to each root a directed graph (digraph) $G_k = (V, S(r_k))$. We create such digraph by starting from the root a breadth-first order vertex traversal, preventing the traversal beyond its non-corresponding joining vertices, in the case of the complete CoW (examples shown in Fig. 4.6). Any artifact cycles are afterwards made bidirectional, hence the orientation for vertices on such cycles will be noninformative. We can then always complement rARG with this derived structure $\bar{G} = (V, E, A, R, \{S(r_k)\})$.

The labeling, in the form of a classification of bifurcations, is based on the availability of a knowledge base (KB) which consists of several elements. First, it contains a set of predefined reference graphs $\{G^{\mathrm{r}}\}$, one for each structure type (Table 4.2 and Fig. 4.6), having BoI as its vertices $V^{\mathrm{r}} = \{v_i^{\mathrm{r}} : 1 \leq i \leq M\}$. Second, from a representative sample of prelabeled graphs as a training set, it extracts the set of sample's vertex attributes $\{A^{\mathrm{r}}\}$ together with the sample's set of joint BoI configurations appearing $\{V^{\mathrm{r}}\}$ for each structure type. The target rARG $\bar{G}^{\mathrm{t}}$ corresponds to the extracted vasculature, having its bifurcations as vertices $V^{\mathrm{t}} = \{v_j^{\mathrm{t}} : 1 \leq j \leq N\}$, vessels as edges E^{t}, root vertices as R^{t}, and the bifurcation attributes as $A^{\mathrm{t}} = \{a_j^{\mathrm{t}}\}$.

Then, on the target graph we define a labeling process as a mapping $\mathcal{L} : V^{\mathrm{t}} \to V^{\mathrm{r}} \cup \{\emptyset\}$, where by the null label ø we denote a bifurcation which is *not of interest*, and is not part of a reference G^{r} (Fig. 4.3). Mapping to the ø can be many-to-one, while the mapping $\mathcal{L}$ restricted to the codomain V^{r} is injective. Due to anatomical variability in topology, $\mathcal{L}$ is not always a surjection and the actual topology (set of BoI) detected, will be denoted with $V_{\mathcal{L}}^{\mathrm{r}} = \mathcal{L}(V^{\mathrm{t}}) \cap V^{\mathrm{r}}$.

Our goal is to estimate the probability $P(\mathcal{L}|\hat{G}^{\mathrm{t}}, \mathrm{KB})$ of $\mathcal{L}$ being correct. There is only one correct labeling and $\sum_{\mathcal{L}} P(\mathcal{L}|\hat{G}^{\mathrm{t}}, \mathrm{KB}) = 1$. We are then interested in finding the mode of this posterior distribution. Thus, the problem is formulated

as finding a labeling $\mathcal{L}^*$ with the maximum a posteriori (MAP) probability

$$\mathcal{L}^* = \arg\max_{\mathcal{L}} P(\mathcal{L}|\hat{G}^{\mathrm{t}}, \mathrm{KB}) \tag{4.1}$$

where by the Bayes theorem

$$P(\mathcal{L}|G^{\mathrm{t}}, A^{\mathrm{t}}, R^{\mathrm{t}}, \mathrm{KB}) \propto p(A^{\mathrm{t}}|\mathcal{L}, G^{\mathrm{t}}, R^{\mathrm{t}}, \mathrm{KB}) P(\mathcal{L}|G^{\mathrm{t}}, R^{\mathrm{t}}, \mathrm{KB}) \tag{4.2}$$

In such MAP estimate, the *prior* term $P(\mathcal{L}|G^{\mathrm{t}}, R^{\mathrm{t}}, \mathrm{KB})$ presents our knowledge-based expectations about the topology of the labeled target graph, where connectivities are considered but local bifurcation features are ignored. This prior regularizes the *likelihood* estimate $p(A^{\mathrm{t}}|\mathcal{L}, G^{\mathrm{t}}, R^{\mathrm{t}}, \mathrm{KB})$, which will be considered to depend only on the local attributes. The dependence on KB will be further omitted for brevity as it is always given.

4.3.3 Likelihood term

To estimate the likelihood term, we assume that the distribution of attributes A^{t} only depend locally on the bifurcation label and are independent of their connectivity E^{t}. Furthermore the attributes are assumed to be statistically independent between bifurcations. Thus, the likelihood term can be written and factorized as

$$p(A^{\mathrm{t}}|\mathcal{L}, G^{\mathrm{t}}, R^{\mathrm{t}}) = p(A^{\mathrm{t}}|\mathcal{L}, V^{\mathrm{t}}) = \prod_{i=1}^{N} p(a_i^{\mathrm{t}}|\mathcal{L}(v_i^{\mathrm{t}})). \tag{4.3}$$

Following the work of Antiga et al. [56,57], each bifurcation is characterized by objective criteria for defining the origin of a bifurcation and bifurcation vectors of the parent branch and the two daughter branches (Fig. 4.4 (a)). The individual bifurcation is modeled by its spatial position and with its three unit vectors pointing away from its center, in the direction the vessels branch off. Furthermore, each vector has a radius associated, obtained as the median cross-section radius of the branching vessel (Fig. 4.4 (b)). Thus, each bifurcation is defined as a 7-tuple

$$a = (\mathbf{x}, \mathbf{n}_0, r_0, \mathbf{n}_1, r_1, \mathbf{n}_2, r_2) \in \mathcal{M} = \mathbb{R}^3 \times S^2 \times \mathbb{R}^+ \times S^2 \times \mathbb{R}^+ \times S^2 \times \mathbb{R}^+. \tag{4.4}$$

The space $\mathcal{M}$ is a manifold endowed with the natural internal operations in each of its factors (vector addition in R^3, rotations in S^2 and multiplication in R^+), which makes it a Riemannian symmetric space.

The estimate $p(a_i^{\mathrm{t}}|\mathcal{L}(v_i^{\mathrm{t}}))$, i.e. the likelihood that a bifurcation with the label $\mathcal{L}(v_i^{\mathrm{t}})$ has the unary attribute a_i^{t}, had been computed using nonlinear statistics on the manifold $\mathcal{M}$ as done similarly by Fletcher et al. [176]. To linearise the operations on the manifold Riemannian log and exponential maps are used, which map the elements of $\mathcal{M}$ to its tangent space $T_p\mathcal{M}$ at a base point $p \in \mathcal{M}$. The maps of $\mathcal{M}$ are the direct product maps of each components. For $\mathbb{R}^3$ this is the identity map. For $\mathbb{R}^+$, these are the standard logarithm and exponential functions on real variables, while for S^2 this is the spherical log and exponential map (defined in [176]). The Riemannian log map to the tangent space for the whole feature space is defined as

$$\mathrm{Log}_p(a) = (\mathbf{x}, \mathrm{Log}_{p_0}(\mathbf{n_0}), \log(r_0), \mathrm{Log}_{p_1}(\mathbf{n_1}), \log(r_1), \mathrm{Log}_{p_2}(\mathbf{n_2}), \log(r_2)). \tag{4.5}$$

This tangent space is a linear space R^{12}, which will be considered Euclidean. We will denote the tangent vectors as $\mathbf{u} = (\mathbf{x}, \mathbf{v}_0, \rho_0, \mathbf{v}_1, \rho_1, \mathbf{v}_2, \rho_2)$, where $\mathbf{x} \in \mathbb{R}^3$ is the positional tangent component, $\rho \in \mathbb{R}$ is the radius tangent component ($\rho = \log(r)$), and $\mathbf{v} \in \mathbb{R}^2$ is the spherical tangent component. The Riemannian exponential map is analogously

$$\mathrm{Exp}_p(\mathbf{u}) = (\mathbf{x}, \mathrm{Exp}_{p_0}(\mathbf{v_0}), \exp(\rho_0), \mathrm{Exp}_{p_1}(\mathbf{v_1}), \exp(\rho_1), \mathrm{Exp}_{p_2}(\mathbf{v_2}), \exp(\rho_2)). \tag{4.6}$$

To estimate variability, second order statistics are computed from the vectors $\mathbf{u_i} = \mathrm{Log}_\mu(a_i), \mathbf{u} \in T_\mu\mathcal{M}$, in the tangent space of the intrinsic mean μ. Intrinsic (Fréchet) mean μ on a manifold is defined as

$$\mu = \arg\min_{p \in \mathcal{M}} \sum_{i=1}^{N} d(p, a_i)^2, \tag{4.7}$$

which can be found using gradient descent. The norm of the tangent vector $\mathbf{u} \in T_p\mathcal{M}$ is defined as

$$\|\mathbf{u}\| = (\|\mathbf{x}\|^2 + \rho_0^2 + \|\mathbf{v_0}\|^2 + \rho_1^2 + \|\mathbf{v_1}\|^2 + \rho_2^2 + \|\mathbf{v_2}\|^2)^{\frac{1}{2}}. \tag{4.8}$$

Then the geodesic distance between two bifurcation feature vectors $a_1, a_2 \in \mathcal{M}$ is given by

$$d(a_1, a_2) = \|\mathrm{Log}_{a_1}(a_2)\|. \tag{4.9}$$

Data is assumed to be localized around the mean and is verified that the spherical tangent components $\mathbf{v_0}, \mathbf{v_1}, \mathbf{v_2}$ are lying within the distance of $\pi/2$ from the mean. Equivalently, it is visually confirmed that individual bifurcation vectors of the population are distributed within one hemisphere (Fig. 4.4 (c)).

The likelihood is then estimated from multivariate normal distribution as

$$p(a_i^{\mathrm{t}}|\mathcal{L}(v_i^{\mathrm{t}})) = \frac{1}{\sqrt{(2\pi)^k\,|\mathbf{S}|}} \exp(-\frac{1}{2}D^2), \tag{4.10}$$

where k is the dimension of the space, D is the Mahalanobis distance $D = \mathbf{u}^T\mathbf{S}^{-1}\mathbf{u}$, and $\mathbf{S}$ is the covariance matrix of the label $\mathcal{L}(v_i^{\mathrm{t}})$, estimated from the sample as $\mathbf{S} = \frac{1}{N-1}\sum_{i=1}^{N} \mathbf{u_i}\mathbf{u_i}^T$. The covariance matrix $\mathbf{S}$ is specific to each label, as different reference bifurcations will have different variabilities. The proposed representation is especially suitable when BoI appears as part of higher order furcations (Fig. 4.4(d)), which is handled by selecting the combination of three branches that minimize the Mahalanobis distance to the corresponding mean feature element.

Ideally, given a large amount of training data, the above Eq. 4.10 would be computed for the full $k = 12$ dimensional space. However, for a more limited data, due to the *curse of the dimensionality* problem, such a large number of parameters affects the generalization capability of the Bayes estimator. Thus, we split the likelihood as a product of three separate likelihood estimates for: 3D space of positions, 6D tangent space of bifurcation vectors and 3D tangent space of radii. This implies the reasonable assumption that the three types of features are independent.

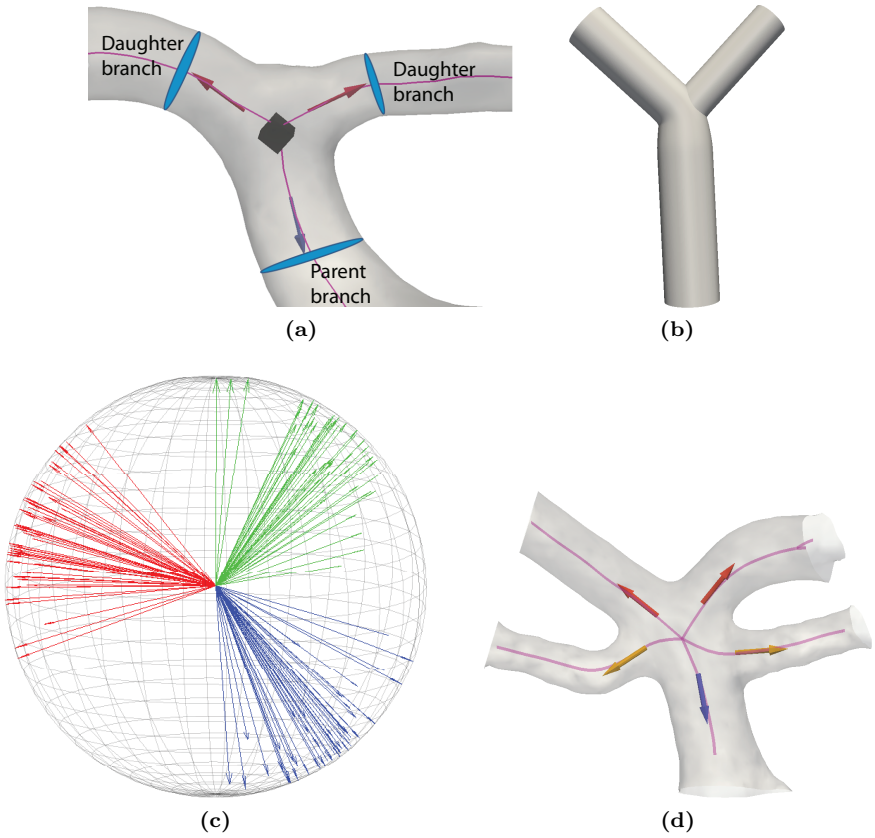

Figure 4.4: Unary attributes: (a) Bifurcation characterization, (b) general cylindrical model of a bifurcation, (c) distribution of bifurcation vectors (example for a terminal ICA bifurcation), (d) example of BA bifurcation (parent in blue and daughters in red) forming part of a quadfurcation. (See color insert)

Finally, it is necessary to define the likelihood for assigning a null label ø to a vertex, i.e. $p(a_i^{\mathrm{t}}|\text{ø})$. In the absence of any other information, we assume that the bifurcations corresponding to ø are uniformly distributed on the reachable finite region of the manifold $\mathcal{M}$. For positional $\mathbb{R}^3$, the uniform distribution in a fixed cuboid region of interest (ROI), defined by expected BoI position range, with volume V_{ROI} has a constant value of $1/V_{\mathrm{ROI}}$. The space $\mathbb{R}^+$ is limited to the expected range of radii values, producing $\frac{1}{\log r_{\max} - \log r_{\min}}$. Uniform distribution on the whole unit sphere S^2 has a value of $\frac{1}{4\pi}$. Thus, we obtain:

$$p(a_i^{\mathrm{t}}|\text{ø}) = \frac{1}{V_{\mathrm{ROI}}} \left(\frac{1}{4\pi}\right)^3 \left(\frac{1}{\log r_{\max} - \log r_{\min}}\right)^3, \tag{4.11}$$

where the expected ranges are obtained from the training set.

4.3.4 Prior term

As mentioned in section 4.1, vasculature of CoW exhibits big variability in its topology. Thus, for many subjects not all BoI are present, i.e. some of the nodes of the reference graph do not have a match on the target graph. Furthermore, some BoI are more probable to be missing than others and absence of one bifurcation can imply that some others further downstream of the flow cannot be present either. In addition, bifurcations can only appear in certain ordering, starting from the roots. Thus, the use of the prior term has a double role. First, it assures that the labels assigned to the target graph follow the ordering they have on the reference graph. Second, it models the probability distribution of topologies $\{V^{\mathrm{r}}_{\mathcal{L}_j}\}$, i.e. the presence of the detected BoI combination.

The ordering of BoI is defined by the root-specific digraphs G_k. Thus, each root r_k induces a partial order on vertices through digraph reachability relationship specified by $S(r_k)$. The labeling of the target graph will be considered compatible with the reference graph if labels on the target digraphs G^{t}_k preserve the partial order of the reference digraphs G^{r}_k. More formally, if for all pairs of the assigned labels which are in $S^{\mathrm{r}}(r_k)$ their corresponding pair of target vertices is in $S^{\mathrm{t}}(r_k)$, for all roots:

$$(V^{\mathrm{r}}_{\mathcal{L}} \times V^{\mathrm{r}}_{\mathcal{L}}) \cap S^{\mathrm{r}}(r_k) \subseteq \mathcal{L}(S^{\mathrm{t}}(r_k)), \quad \forall r_k. \tag{4.12}$$

Prior term then restricts the set L^{t} of all possible labelings of the target only to the compatible ones $\mathcal{L} \in L^{\mathrm{t}}_{\mathrm{c}} \equiv \{\mathcal{L}_1, \ldots, \mathcal{L}_Q\}$, each labeling with its corresponding set of involved BoI $\mathbf{V}^{\mathrm{r}}_c \equiv \{V^{\mathrm{r}}_{\mathcal{L}_1}, \ldots, V^{\mathrm{r}}_{\mathcal{L}_Q}\}$. Then we can write:

$$P(\mathcal{L}|G^{\mathrm{t}}, R^{\mathrm{t}}) = \begin{cases} 0 & \text{if } \mathcal{L} \notin L^{\mathrm{t}}_{\mathrm{c}} \\ P(i|V^{\mathrm{t}}, E^{\mathrm{t}}, R^{\mathrm{t}}, L^{\mathrm{t}}_{\mathrm{c}}) & \text{if } \mathcal{L} \in L^{\mathrm{t}}_{\mathrm{c}}; \mathcal{L} = L^{\mathrm{t}}_{\mathrm{c}}(i) \end{cases} \tag{4.13}$$

where $P(i)$ denotes the probability that the correct labeling is at the i^{th} indexed position in the set of compatible labelings.

The probability distribution of the non-zero prior $P(i|V^{\mathrm{t}}, E^{\mathrm{t}}, R^{\mathrm{t}}, L^{\mathrm{t}}_{\mathrm{c}}, \mathbf{V}^{\mathrm{r}}_c)$, can then be obtained under certain assumptions. It is first assumed that the probability of a particular labeling from the set $L^{\mathrm{t}}_{\mathrm{c}}$ will be independent on the particular E^{t} and R^{t}:

$$P(i|V^{\mathrm{t}}, E^{\mathrm{t}}, R^{\mathrm{t}}, L^{\mathrm{t}}_{\mathrm{c}}, \mathbf{V}^{\mathrm{r}}_c) = P(i|V^{\mathrm{t}}, L^{\mathrm{t}}_{\mathrm{c}}, \mathbf{V}^{\mathrm{r}}_c). \tag{4.14}$$

Thus, the locations of ø do not affect the prior probability. We further assume that the prior probability only depends on the detected topology $V^{\mathrm{r}}_{\mathcal{L}}$ and is independent of the particular vertices of V^{t} that map to the $V^{\mathrm{r}}_{\mathcal{L}}$, as long as $\mathcal{L} \in L^{\mathrm{t}}_{\mathrm{c}}$. Thus,

$$P(i|V^{\mathrm{t}}, L^{\mathrm{t}}_{\mathrm{c}}, \mathbf{V}^{\mathrm{r}}_c) = P(i|\mathbf{V}^{\mathrm{r}}_c) \propto P(\mathbf{V}^{\mathrm{r}}_c|i)P(i) \propto P(\mathbf{V}^{\mathrm{r}}_c|i), \tag{4.15}$$

where we have considered that $P(i)$ is constant, i.e. the order of the labelings in the set $L^{\mathrm{t}}_{\mathrm{c}}$ is arbitrary. Lastly, given that the correct labeling $\mathcal{L}$ is in the position i ($\mathcal{L} = \mathcal{L}_i$) we assume that the prior only depend on $V^{\mathrm{r}}_{\mathcal{L}_i}$ and that the presence of any other set of compatible topologies in the set $L^{\mathrm{t}}_{\mathrm{c}}$ is equally probable and independent of $\mathcal{L}_i$:

$$P(\mathbf{V}^{\mathrm{r}}_c|i) \propto P(V^{\mathrm{r}}_{\mathcal{L}_i}|i) = P(V^{\mathrm{r}}_{\mathcal{L}}) \tag{4.16}$$

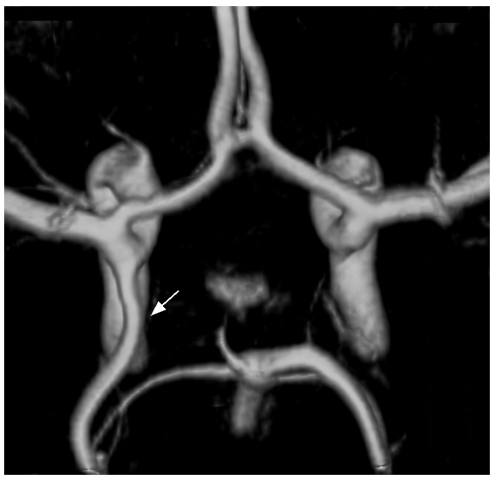

Figure 4.5: Volume rendering of a subject with P1 segment missing, where the left PcoA (denoted with arrow) takes the role of the left PCA. Thus, PcoA-A bifurcation is present but not PcoA-P.

Finally, the prior term can then be summarized as

$$P(\mathcal{L}|G^{\mathrm{t}}, R^{\mathrm{t}}) = \begin{cases} 0 & \text{if } \mathcal{L} \notin L_{\mathrm{c}}^{\mathrm{t}} \\ P(V_{\mathcal{L}}^{\mathrm{r}}) & \text{if } \mathcal{L} \in L_{\mathrm{c}}^{\mathrm{t}}; \end{cases} \tag{4.17}$$

4.3.5 Reference graphs and their selection

For every structure type (Table 4.2), we created a reference graph (Fig. 4.6), which forms part of KB. All reference graphs have all the BoI present. This is because the communicating paths do not necessarily have to be cut at the communicating arteries, as A1 or P1 segments could also be missing and the communicating arteries AcoA and PcoA would connect directly to A2 and P2 segments, respectively (example shown in Fig 4.5). Thus, we cannot deduce beforehand which of the BoI are missing and such lower scale ambiguities and the actual topology have to be resolved later by the labeling method.

The labeling method requires that the target and the reference graphs induce compatible partial orders from their roots. As different topologies of CoW will induce different partial orders, we need to select the appropriate reference graph from KB. The selection is based on the observed target structure type. As mentioned in subsection 4.3.1, we can uniquely identify the target structure type, except when only one communicating path is missing (ST5, ST6, and ST7), as there all roots are mutually reachable. Thus, in such cases, we perform three separate labelings with each of the three possibly corresponding reference graphs, having the same prior $P(G^{\mathrm{r}})$. We then combine all the resulting labelings, expecting that those based on incompatible reference graphs will produce very low posterior probabilities.

Lastly, the reference graph used in the labeling adapts the prior term of the posterior probability estimate (Eq. 4.2). In particular, the presence of the three communicating paths affects the prior probability of detecting BoI on them. Their

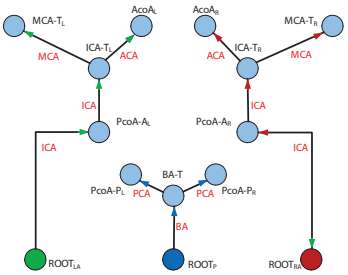

(a) ST1: Three isolated trees

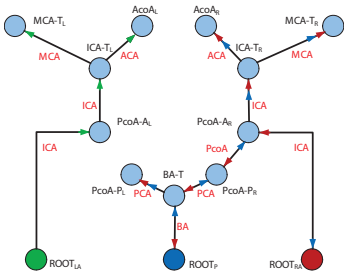

(b) ST2: Left ant. tree isolated

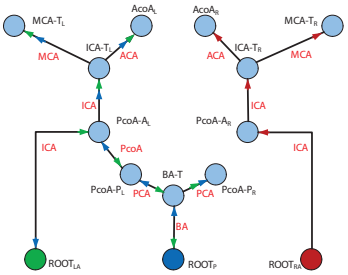

(c) ST3: Right ant. tree isolated

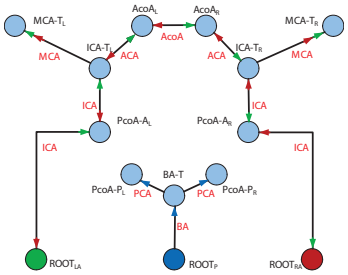

(d) ST4: Post. tree isolated

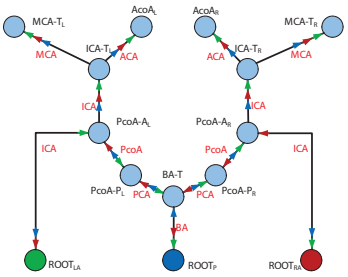

(e) ST5: Conn. via post. tree

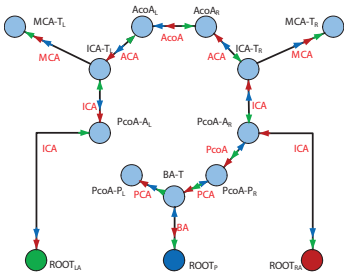

(f) ST6: Conn. via right ant. tree

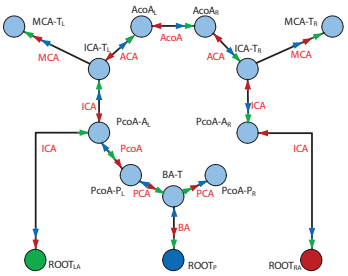

(g) ST7: Conn. via left ant. tree

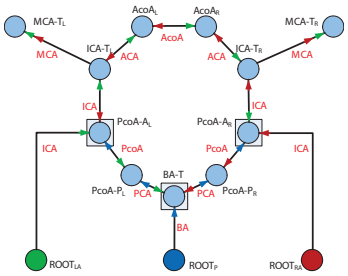

(h) ST8: Complete CoW

Figure 4.6: The eight reference graphs with overlayed digraphs, induced by each root of the graph. In (h), the *joining vertices* are denoted with square. Bifurcation and artery names correspond to the Fig. 4.1. (See color insert)

presence status is uniquely determined by the structure of the reference graph. Considering the probability of presence of BoI belonging to different paths to be independent, we obtain:

$$\begin{aligned} &P(V^{\mathrm{r}}_{\mathcal{L}}|G^{\mathrm{r}}) = P(V^{\mathrm{r}}_{\mathcal{L}}|\mathrm{AcoP}, \mathrm{LPcoP}, \mathrm{RPcoP}) = \\ &= P(\mathrm{ICA_L}, \mathrm{AcoA_L}, \mathrm{AcoA_R}, \mathrm{ICA_R}|\mathrm{AcoP})\cdot \\ &\cdot P(\mathrm{PcoA\text{-}A_L}, \mathrm{PcoA\text{-}P_L}|\mathrm{LPcoP})\cdot \\ &\cdot P(\mathrm{PcoA\text{-}A_R}, \mathrm{PcoA\text{-}P_R}|\mathrm{RPcoP})\cdot \\ &\cdot P(\mathrm{MCA}_L)P(\mathrm{MCA}_R)P(\mathrm{BA}), \end{aligned} \tag{4.18}$$

where the BoI and path names (from Table 4.2) denote their presence status.

4.3.6 Optimization

MAP estimation, in general, is very computationally expensive. Exhaustive testing for all possible labelings $\mathcal{L} \in L^{\mathrm{t}}$ is not feasible. However, many vertex-label pairings can be automatically discarded based on either zero prior probability or low likelihood. In fact, the *prior* probability $P(\mathcal{L}|G^{\mathrm{t}}, G^{\mathrm{r}})$ is non-zero only for a small subset of all combinations ($\mathcal{L} \in L^{\mathrm{t}}_{\mathrm{c}}$) i.e. only for those which are compatible with the reference graph. To avoid labelings involving very low probable attributes, we exclude outliers based on their Mahalanobis square distance D^2. Under multivariate normal distribution assumption, it is a χ^2 distribution. We then detect the outliers at 99.99% cutoff level.

The labeling is a morphism $\mathcal{L} \subseteq V^{\mathrm{t}} \times (V^{\mathrm{r}} \cup \emptyset)$. A standard algorithm for mapping between two graphs is based on building their association graph and then finding *maximal cliques* of such an undirected graph [203, 204]. Association graph $G = (V^{\mathrm{a}}, E^{\mathrm{a}})$ is built from G^{t} and G^{r}, where nodes are denoted with a pair of indices $V^{\mathrm{a}} = \{v^{\mathrm{a}}_{i,j} \equiv (v^{\mathrm{t}}_i, v^{\mathrm{r}}_j)\} \subset V^{\mathrm{t}} \times (V^{\mathrm{r}} \cup \{\emptyset\})$. The following rules are applied. Node is created only if unary attribute of v^{t}_i with the label of v^{r}_j is not considered an outlier. Edge $(v^{\mathrm{a}}_{i,j}, v^{\mathrm{a}}_{k,l})$ is created for $i \neq k$ and $j \neq l$, unless $(v^{\mathrm{r}}_j, v^{\mathrm{r}}_l) \in S^{\mathrm{r}}(r_k)$ and $(v^{\mathrm{t}}_i, v^{\mathrm{t}}_k) \notin S^{\mathrm{t}}(r_k)$ for any r_k, ensuring ordering compatibility. Edges pairing with the $\emptyset$ are always created.

Finding maximal cliques, which in our case will always be of the size N of the target graph, in an undirected graph is in general a NP-complete problem. However, removing the nodes of the association graph detected as outliers, cuts down the computational effort to a manageable size. Here any clique finding algorithm can be used [205]. We used the algorithm of Tomita el a. [206], in which pruning methods are employed to reduce the size of search space, and where benchmarks showed to run fast in practice.

4.4 Results

We evaluated the proposed methodology on a set of 50 images of healthy volunteers (25 male, 25 female, age range: 19-66, mean age: 39), acquired with ToF-MRA on a 3T unit under standardized protocols. Images were reconstructed with 448 ×

448×128 matrix, having a voxel size of $0.5 \times 0.5 \times 0.8$ mm^3. The images come from the dataset that was used in [50] and is freely available as open data[1].

In a preprocessing step, the images were first resampled in axial direction by a bicubic interpolation to obtain isotropic resolution. As the graph attributes are position and pose dependant, all images were registered with similarity transformations, using mutual information metric, to the one chosen as the reference (first image in the dataset). To evaluate the influence, we have repeated the later experiments with two other, randomly chosen, reference images and the mean performance values have remained the same, showing robustness to the actual reference choice. Influence was observed in three cases when two best labelings had similar posterior probabilities, causing them to exchange places.

In addition, region of interest (ROI) around CoW was defined on the reference image and all the registered images were cropped for the purpose of processing speed-up and preventing potential connectivity errors deep in the vascular network. The ROI is visible in Fig. 4.2, and was chosen with a large margin around BoI positions. The images were then segmented and vascular models constructed. The root vertices and the presence of CoW cycle have been correctly determined in all cases. The number of branching nodes (BoI candidates) present in the graphs was 38 ± 7 (mean $\pm$ std).

The performance of anatomical labeling method was evaluated using cross-validation of BoI classification. One expert clinician manually labeled the BoI on each vascular model. All the other bifurcations were assigned the ø label. Leave-one-out cross-validation was then run. In the performance analysis we evaluate detection accuracy, precision, sensitivity and specificity rates (Table 4.3). Examples of anatomical labeling results are shown in Fig. 4.7, where the surface of each corresponding vessel segment is color labeled. We separately evaluated per case rate of correctly labeling all the BoI and the topology detection: whether the set of BoI determined to be present is correct.

From the table, it can be observed that the BoI detection rates are high, but unfortunately the errors are evenly spread across cases so 60% are labeled entirely correctly. Most of the detection errors (Fig. 4.7(e)&(f)) are in locating the MCA terminal bifurcation (excluding MCA, 84% of cases would be correctly labeled), which is always present ($P(\text{MCA}) = 1.00$ in Eq. 4.18). The difficulty in locating this bifurcation is not unexpected as the MCA has the most complex branching pattern of any of the major cerebral arteries [207, 208]. Furthermore, MCA is outside the cycle forming CoW and no BoI is located further away, hence the connectivity and prior term are not contributing strongly to its localization. In general, the result shows that the method favors sensitivity over specificity, i.e. it finds false BoI rather than miss one. This can be attributed to the conservative size of the finite reachable region of the feature space used in estimating the ø-label likelihood (Eq. 4.11). The region was guaranteed to include any bifurcation, with the risk of being too large. Of the false positives, most appeared due to mistaking a small side branch for a communicating artery (PcoA or AcoA), when the latter was actually missing. In particular, anterior choroidal artery, which is located just next to PcoA and branches in the same direction, can be mistaken for a PcoA branching from the anterior side and not connecting with the posterior root.

[1] http://hdl.handle.net/1926/594

Table 4.3: Performance analysis of the proposed method. For detection rate: accuracy, precision, sensitivity and specificity are given (N/A denotes "not available" when 0/0). The mean values are weighted across BoI.

Bifurcation of interest	*Detection*			
	Accuracy	Precision	Sensitivity	Specificity
ICA_L	0.98	1.00	0.98	N/A
ICA_R	1.00	1.00	1.00	1.00
$PcoA_{FL}$	0.98	1.00	0.97	1.00
$PcoA_{FR}$	0.98	0.97	1.00	0.93
$AcoA_L$	0.96	0.98	0.98	0.89
$AcoA_R$	0.98	1.00	0.97	1.00
$PcoA_{BL}$	0.96	0.95	1.00	0.87
$PcoA_{BR}$	1.00	1.00	1.00	1.00
BA	0.96	0.98	0.98	N/A
MCA_L	0.80	0.80	1.00	N/A
MCA_R	0.84	0.84	1.00	N/A
Mean	0.95	0.95	0.99	0.95
Per case	Labeling all correct: 60%, Topology correct: 88%			

Table 4.4: Comparison of mean performance values between different method variants.

Method	*Detection mean rates*				*Topology*
	Accuracy	Precision	Sensitivity	Specificity	
AT $\sim$ [167, 199]	0.91	0.91	0.98	0.76	64%
AT+G$\sim$ [94, 197]	0.92	0.93	0.98	0.81	62%
AT+G+AP	0.93	0.93	0.98	0.85	76%
AT+G+AP+R	0.95	0.95	0.99	0.95	88%

To evaluate the contribution of different elements of the method we repeated the above evaluation for different method variants. The first variant (AT) is based just on the unary attributes without taking the graph and its node connectivity, nor prior term into account. Such variant can be seen as an adaptation of the labeling presented in [167, 199]. The second variant (AT+G) is using the unary attributes and the graph preserving ordering, but without the prior term. This can be considered as an adaptation of the approaches of [94, 197]. Finally, the last two variants, are the proposed method with two different prior terms. One prior term (AT+G+AP) contains overall population appearance probabilities independent of the reference graph used, while the other (AT+G+AP+R) further adapts them based on the structure type of the chosen reference graph (Eq. 4.18). Their performance values are shown in Table 4.4.

Gradually adding the regularization terms improved the performance across the rates. In particular, adding the prior term clearly improved the specificity and topology detection. With it, some bifurcations with side branches are prevented from assigning a BoI label as otherwise they would form configurations which are uncommon in a population. In particular the reference graph based prior was shown effective and improved specificity and topology by $\sim 10\%$. With just AP prior, the false positives appeared when assigning communicating arteries while

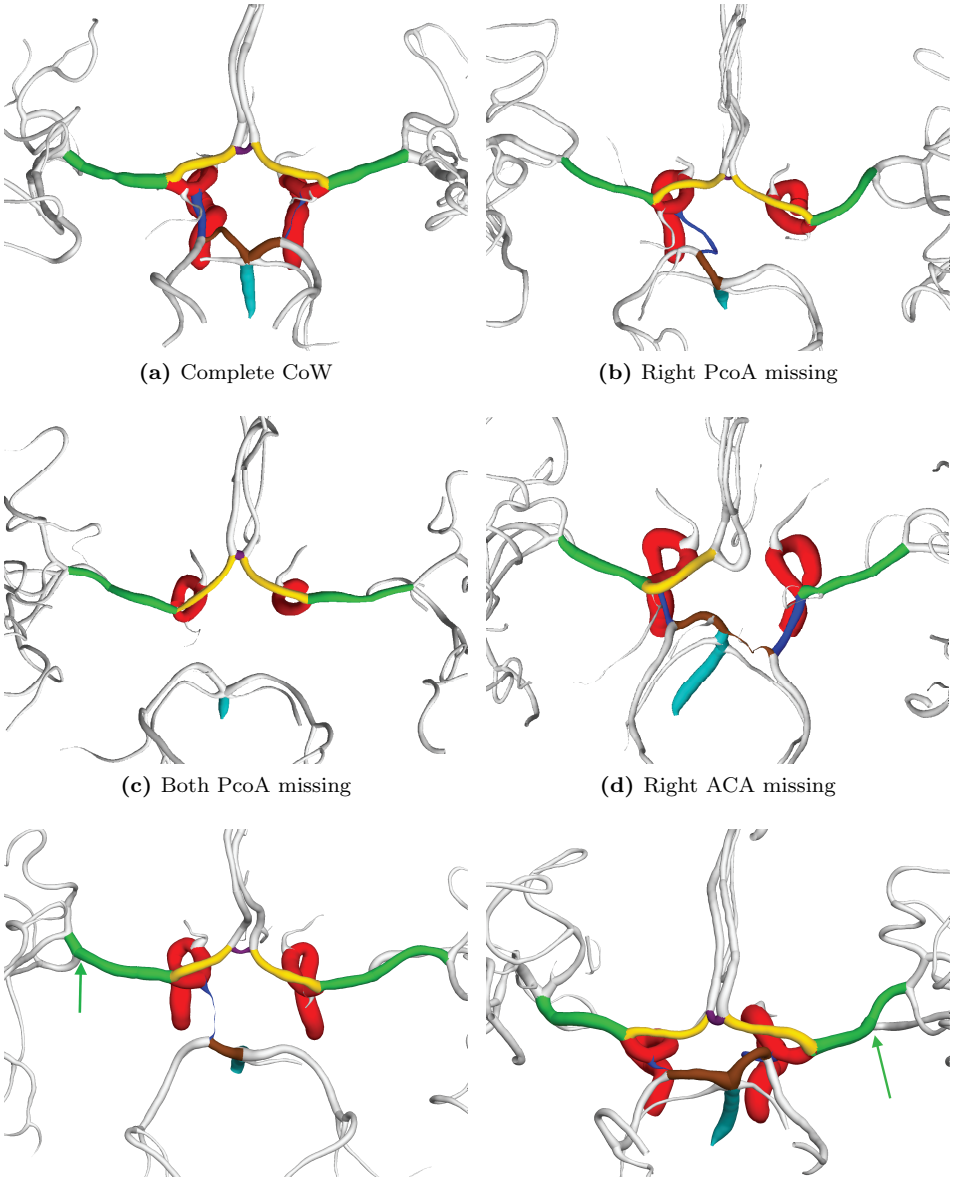

(a) Complete CoW **(b)** Right PcoA missing

(c) Both PcoA missing **(d)** Right ACA missing

(e) Error in left MCA bifurcation **(f)** Error in right MCA bifurcation

Figure 4.7: Anatomically labeled Circle of Willis. Denoted vessels: ICA (red), BA (turquoise), ACA (yellow), PCA (brown), PcoA (blue), AcoA (purple), MCA (green). Correct labeling is shown in (a-d). Examples of incorrect MCA labeling are shown in (e,f), where the arrow denotes the true terminal bifurcation. (See color insert)

they were missing. By using AP+R prior, these errors are avoided as they would be contradictory with the property of having disconnected roots.

As the method is formulated in a probabilistic framework the candidate label-

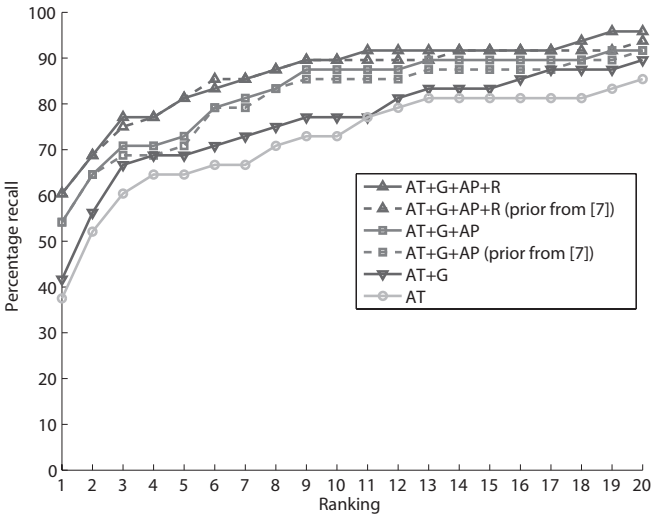

Figure 4.8: Percentage of cases with the correct labeling appearing ahead or equal the given rank, for the three method variants: AT+G, AT+G+AP, and AT+G+AP+R.

ings can be ranked by their estimated posterior probabilities. The method always selects the most probable one (the highest ranked one). However, in the case that selected labeling is visually observed to be incorrect, this enables a user to select the next most probable candidate in the ranked list. Thus, for the erroneously labeled cases, we searched for the correct labeling in the ranked list (Fig. 4.8). From the figure it is evident that using the prior term helps to position correct labelings higher in the ranking list, and for 90% of cases the correct labeling is within the first ten positions.

The prior term was shown above to have a positive effect on the classification and ranking success. To evaluate whether the learned prior was data specific, we first compared (Table 4.5) the prevalence of anatomical variants learned from this data with the one reported in [8], where they visually inspected 150 ToF-MRA images of healthy volunteers. Overall, the obtained values were similar and none of the differences were statistically significant ($p > 0.05$). Second, we formed the prior term exclusively based on [8] and rerun the labelings (Fig. 4.8). The obtained rankings were also similar, which shows that the learned prior and the data used could be representative of the normal healthy population.

4.5 Discussion

In this work we developed a method for labeling main arteries of the CoW, known to exhibit large anatomical variability. In the dataset used for evaluation, the complete CoW was present in one third of the cases (34%), hence encountering missing arteries was the norm, not the exception. The task of anatomical labeling was posed as the classification of the BoI to make the method insensitive to the number of side branches that an artery might have.

Table 4.5: Prevalence of the main anatomical variants. Comparison between the reference study [8] (150 subjects) and the values learned from this data (50 subjects). Numbers represent percentage of subjects with the given topological property.

	Hartkamp et al. [8]	Learned data
Complete CoW	42%	34%
Complete anterior part	74%	80%
AcoA missing	19%	16%
A1 segment missing	7%	4%
Complete posterior part	52%	48%
Both PcoA missing	11%	12%
Unilateral PcoA missing	33%	30%
P1 segment missing	4%	10%

Bifurcations are characterized as points in a Riemannian manifold, and statistics computed in tangent space, inspired by the work on medial representation atoms [209, 210]. This is especially suitable when BoI appears as part of higher order furcations. Although in cerebral vasculature trifurcations are rare, BoI having other, side bifurcations in close vicinity can appear as part of a higher order furcation due to limit in skeletonization reconstruction resolution. Bifurcations not of interest (ø label) are modeled as uniformly distributed on the finite region of the feature space. Being able to estimate likelihood for assigning ø is crucial for comparing labelings containing different number of BoI detected. Both the BoI feature distributions and the prior probabilities of appearance are learned from the training set of prelabeled examples. We tested substituting prior probabilities with the ones from [8], which showed that the method could integrate the values from other, future studies, which analyze anatomical variability of CoW of a large population, in sufficient detail.

The method supports graphs that contain a cycle and have multiple roots, as long as each root is attached to the cycle at a different node, which allows to split the graph into multiple digraphs. Each digraph induces partial order on its nodes and enables finding reference topology preserving labelings. Such labelings are obtained by computing maximal cliques of the association graph, which is a standard method for graph matching [203]. Although finding maximal cliques is known to be NP-hard, it is a well studied problem and powerful heuristics exist which efficiently find good approximate solutions. In our application, it was computationally feasible to find all maximal cliques, as the association graph could be substantially pruned by removing outlier pairing nodes based on local features.With the pruned association graph having ≈ 50 nodes, maximal cliques were found in a couple of seconds, using the implementation in C programming language.

A limitation of our method is that BoI merging is not supported. There is a known anatomical variability where AcoA's length reduces to a point ($\mathrm{AcoA_L}$ and $\mathrm{AcoA_R}$ bifurcations merge), but it is rare (1.3% prevalence in [8]) and is not taken into account in this work. In general this could be handled in a labeling post-processing step, by analyzing a bifurcation that has a high likelihood of being two neighboring BoI. In addition, the chosen BoI of CoW never switch their ordering, otherwise a separate reference graph for each ordering variant is required.

Finally, we do not make use of any binary (edge) attributes. They might further improve the robustness of the method, but also introduce difficulty in modeling the likelihood of ø assignments, and the treatment of spurious side branches.

The closest related works are the ones of Tschirren et al. [94] and Mori et al. [197], designed to label airway and abdominal vascular trees, respectively. Their and our approach is in the essence combination optimization regularized by digraph. They both model branch or branchpoint feature variability also with normal distribution. The main difference from our work is that they did not face the problem of missing branches, and comparing labelings having different reference graphs and labels present. Thus, their approach can be seen as maximal likelihood (ML) estimate, as opposed to our MAP. Furthermore their anatomical structures had a simpler topology: a rooted tree.

The performance comparison with the related work is difficult, as none are directly applicable to the CoW. Thus, we created variants of the proposed method which are adaptations of the concepts used elsewhere. The results showed that the proposed MAP method outperformed the ML-based one. The method has been evaluated on open data, which should facilitate future comparisons with other methods and studies. In addition, the statistical values reported in Table 4.5 could be of value to future users of the same dataset.

Overall, the BoI were detected with high (95%) accuracy and precision. These rates are comparable to the ones obtained by the state of the art methods designed for other anatomies (Table 4.1). However, it had a relatively low success rate (60%) of completely labeling the entire CoW. Errors were focused mostly around the location of MCA terminal bifurcation which is known to be hard to identify. As a comparison, other related works unfortunately avoided reporting the per case labeling success. It can be read only from the results of [94], where it would correspond to the per case labeling success of 47% (8/18). This hints that similar, low overall performances, are expected to be present in other works, and shows the difficulty and future challenges in designing a successful labeling method. That is why we proposed to find all topologically valid labelings and rank them by their posterior probability. This has a practical value in the scenario of minimally interactive labeling. If the MAP solution is not found to be correct after visual inspection by the user, the method can quickly provide other promising candidates. For erroneously labeled cases, the evaluation showed that the correct solution was most frequently ranked second. Finally, the corrected solution can then be used to increase the training set and improve future performance.

4.5.1 Conclusions and outlook

The proposed labeling method is based on combining local BoI attributes and their graph connectivity with the prior probability of encountering the global topology they form. From a set of prelabeled examples, the method is able to learn bifurcation feature variability as well as variation in topology and their probabilities of occurrence. It does not require any parameter setting, besides the one used for outlier removal in the optimization step, which has intuitive interpretation and can remain fixed. The main contributions of the presented work are the following:

- Characterizing the bifurcations as points on Riemannian manifold, where

spherical components facilitate comparison of bifurcations with general n-furcations.

- Modeling the likelihood for ∅ assignment, hence enabling comparison between labelings detecting different number of labels.
- Introduction of a priori probabilities of label configuration appearance.
- Method for defining partial order on graphs with a cycle and multiple roots.

The methodology (section 4.3), is posed general and can find application in labeling other tubular or vascular structures, apart from CoW. Structures where the underlying graph has cycles, can be observed at the level of capillary networks. In addition, in many organs, arteries can directly fuse (anastomose) with each other, forming collateral circulation, which can appear naturally or as a result of pathology remodeling.

The method developed in this work is a step toward the extensive geometric characterization of the CoW. Apart from topology and bifurcations geometry, the geometry of individual vessels can further be characterized using the technique proposed in [58]. Having such complete characterization of CoW in a population is of value in the pursuit of identifying geometric risk factors, a goal of the future work.

5

General Conclusions

This thesis has focussed on the development and validation of a method for image-based geometric characterization of the Circle of Willis (CoW), covering the entire processing pipeline from a medical image to the extraction of geometric descriptors allowing comparison and dissimilarity measure between subjects. This goal has been achieved by solving sequentially the following tasks:

- Achieve automated segmentation of the cerebral vasculature from images obtained with different modalities, across the clinical centers (Chapter 2).
- Once segmented, characterize individual vessels (Chapter 3) and bifurcations (Chapter 4), accounting for the full complexity of their shape.
- Identify from the segmentation the principal vessels (arteries) and bifurcations of CoW, to be able to compare their characteristics in a population of subjects (Chapter 4).

The ordering presented in the thesis does not necessarily coincide with the positions of the developed methods in the characterization pipeline. In particular, anatomical labeling of the CoW (Chapter 4) can immediately follow the vascular segmentation (Chapter 2). Then, although not explicitly done, each identified vessel could be characterized using the approach developed for the internal carotid artery (ICA) (Chapter 3), which is the vessel of the CoW with the most complex geometry.

5.1 Overview

We next summarize the advances presented in previous chapters and discuss the problems encountered, and promising topics for the future work.

5.1.1 Vascular segmentation

As reported in Chapter 2, few methods are able to achieve fully automated segmentation, as majority of them require certain amount of user-interactivity to guide the segmentation, especially in the initialization phase. Relying on the training set of pre-segmented images and the image intensity standardization filter, our automated improved geodesic active regions method was shown to be able to generalize well on images coming from different clinical centers. The method was selected and extensively used for segmenting angiographic images within the large scale integrated project @neurIST [11, 211]. There, the vessel segmentation was the first step in a processing pipeline for estimating aneurysm rupture risk, based on computational fluid dynamics (CFD) studies. To obtain sufficiently large number of images, typically, multiple clinical centers have to be recruited. Thus, the robustness of segmentation methods to different image acquisition protocols and devices, in addition to automation, was of high importance.

In general, the success of the segmentation is tightly linked with the angiographic image quality (spatial resolution and signal-to-noise ratio). We found particularly difficult the task of accurately segmenting the aneurysms from ToF-MRA images, as that modality is prone to artifacts coming from slow and disturbed blood flow, especially present inside large aneurysms. Similarly due to its

low spatial resolution, it was difficult to avoid merging of nearby structures (vessels touching each other or nearby aneurysm). This could be prevented by using prior knowledge of the underlying skeleton structure to constrain a topology preserving level set evolution, an *inverse skeletonization* approach we pursued in Chapter 4.

5.1.2 Geometric characterization

In Chapter 3, we presented the methodology for characterization of carotid siphon part of the ICA. As a first step toward the characterization we developed a novel method for identification of its constituent four bends. Achieving good robustness to the varying levels of centerline smoothness was one of the main advantages of the proposed approach. Although the choice of bends was specific to ICA anatomy, the method developed is applicable to other vessels. Identifying the bend transitions as points of correspondence across subjects is also part of *anatomical labeling*, a task we took on for the entire CoW in Chapter 4. There, we also proposed a characterization of bifurcations.

Characterization of the siphon was performed by two different approaches. First, more traditionally, as a set of local and global geometric features known to have an effect on hemodynamics. Second, establishing novel dissimilarity measure between ICAs, based on the LDDMCM energy of registering one ICA to another. Geometry of ICA is especially interesting to characterize due to its importance as one of the main afferent arteries of CoW and due to its large geometric variability. Although performing clinically oriented studies was not part of the thesis objective, the developed characterization methodology opens the path for the search of geometric risk factors and predicting treatment difficulty and success. Due to its complex shape and being a frequent site of diseases, ICA is a very suitable case-study vessel for obtaining insight and knowledge of the interplay between geometry, hemodynamics and pathology [212].

5.1.3 Anatomical labeling

The identification of the main cerebral arteries by detecting the bifurcations forming CoW was approached in Chapter 4. In general, the labeling task is tightly linked with the one of the characterization of bifurcations, which is used to differentiate between them. A novel bifurcation characterization was developed where they are described as points on a Riemannian manifold. The bifurcations of interest are modeled as normally distributed, while the rest, spurious or not of interest, as uniformly spread on a finite region of the feature space. The main challenge of the labeling method was handling the large anatomical variability present in both geometry and topology of the CoW. For that, we proposed a solution within the maximum a posteriori probability framework, where the prior knowledge of possible topologies regularizes the estimated labeling likelihood based on local geometric properties only. Furthermore, we showed how to benefit from the graph connectivity of bifurcations, even in the presence of a cycle and multiple roots.

5.2 Outlook and further research directions

The characterization pipeline developed in the thesis is a step toward building a generative statistical model of the CoW, which would ultimately capture its full complexity from the variability in geometry of its vessels and bifurcations to the one in topology. Capturing the joint variability requires having a large number of CoW examples, hence enabling high-throughput processing is essential.

Furthermore, it would be of interest to know how does this variability affect blood circulation and to understand the sensitivity of cerebral perfusion on CoW geometry. An estimate of the blood flow within the CoW can be obtained by using CFD, which approximately solves Navier-Stokes equations, as done in [213–215]. However, CFD is very computationally demanding and currently modeling the flow in the arteries of the entire brain takes $\approx$ 40 hours [216]. Alternatively, it could be substituted by time-resolved PC-MRA acquisitions, sacrificing the spatial and temporal resolution offered by CFD [217]. Ideally a statistical model should also include the CoW hemodynamics. Building such combined models is part of an exciting, emerging field of computational functional anatomy [218].

Building a statistical model of the CoW still requires finding solutions to several basic problems. In particular the problem of defining suitable metric in the shape space of CoW. For example, it is not clear how to encode or weigh the changes in topology and those in geometry to obtain CoW (dis)similarity measure or how to do statistics on such graph-structured data [219, 220]. Only recently, efforts have been made in that direction for the case of simpler, tree-like structures, where the first techniques properly defining an average structure [221] and the principal modes of variation [222] in a non-Euclidean shape space are being proposed.

Such models could find their use in answering several basic but still open questions, some of which are [48]:

- How does the average CoW looks like and what are its principal variations?
- Is there any difference in CoW geometry and topology between men and women? Given that prevalence of aneurysms is larger in women, it would be interesting to know if this can be partly attributed to the different CoW geometry between them.
- Is the difference in handedness reflected in the CoW?
- Does the CoW change with aging and how?
- What would be considered normal variability of the CoW and what would be deviations associated with the risk of developing a pathology?
- Can we predict or estimate a risk of aneurysm rupture, from the CoW? A question of prime clinical importance for the treatment selection.

None of these questions have a proper answer yet, which is partly due to the lack of techniques able to process the data and characterize the CoW, the gap this thesis has tried to close.

References

[1] G. A. Donnan, M. Fisher, M. Macleod, and S. M. Davis, "Stroke," *The Lancet*, vol. 371, pp. 1612–1623, May 2008.

[2] "World Health Organization (WHO), The top ten causes of death - Fact sheet N310." http://www.who.int/mediacentre/factsheets/fs310/en/index.html, 2011.

[3] J. van Gijn, R. S. Kerr, and G. J. E. Rinkel, "Subarachnoid haemorrhage," *The Lancet*, vol. 369, pp. 306–318, Jan. 2007.

[4] C. Ustun, "Dr. Thomas Willis' famous eponym: The Circle of Willis," *Turkish Journal of Medical Sciences*, vol. 34, pp. 271–274, 2004.

[5] A. G. Osborn and J. M. Jacobs, *Diagnostic cerebral angiography*. Lippincott Williams & Wilkins, second ed., 1999.

[6] http://www.anatomyatlases.org/AnatomicVariants/Cardiovascular/Text/Arteries/CircleofWillis.shtml.

[7] B. J. Alpers, R. G. Berry, and R. M. Paddison, "Anatomical studies of the circle of Willis in normal brain," *A.M.A. Archives of Neurology and Psychiatry*, vol. 81, pp. 409–418, Apr. 1959.

[8] M. J. Krabbe-Hartkamp, J. van der Grond, F. E. de Leeuw, J. C. de Groot, A. Algra, B. Hillen, M. M. Breteler, and W. P. Mali, "Circle of Willis: morphologic variation on three-dimensional time-of-flight MR angiograms," *Radiology*, vol. 207, pp. 103–111, Apr. 1998.

[9] J. L. Brisman, J. K. Song, and D. W. Newell, "Cerebral aneurysms," *New England Journal of Medicine*, vol. 355, pp. 928–939, Aug. 2006.

[10] M. C. Villa-Uriol, I. Larrabide, J. M. Pozo, M. Kim, O. Camara, M. De Craene, C. Zhang, A. J. Geers, H. Morales, H. Bogunovic, R. Cardenes, and A. F. Frangi, "Toward integrated management of cerebral aneurysms," *Philosophical Transactions of the Royal Society A: Mathematical, Physical and Engineering Sciences*, vol. 368, pp. 2961–2982, June 2010.

[11] M. C. Villa-Uriol, G. Berti, D. R. Hose, A. Marzo, A. Chiarini, J. Penrose, J. Pozo, J. G. Schmidt, P. Singh, R. Lycett, I. Larrabide, and A. F. Frangi, "@neurIST complex information processing toolchain for the integrated management of cerebral aneurysms," *Interface Focus*, vol. 1, pp. 308–319, Apr. 2011.

[12] J. B. Thomas, L. Antiga, S. L. Che, J. S. Milner, D. A. H. Steinman, J. D. Spence, B. K. Rutt, and D. A. Steinman, "Variation in the carotid bifurcation geometry of young versus older adults: Implications for geometric risk of atherosclerosis," *Stroke*, vol. 36, no. 11, pp. 2450–2456, 2005.

[13] S. G. Frangos, V. Gahtan, and B. Sumpio, "Localization of atherosclerosis: Role of hemodynamics," *Archives of Surgery*, vol. 134, pp. 1142–1149, Oct. 1999.

[14] J. R. Cebral, M. A. Castro, S. Appanaboyina, C. M. Putman, D. Millan, and A. F. Frangi, "Efficient pipeline for image-based patient-specific analysis of cerebral aneurysm hemodynamics: Technique and sensitivity," *IEEE Transactions on Medical Imaging*, vol. 24, pp. 457–467, Apr. 2005.

[15] J. R. Cebral, F. Mut, J. Weir, and C. M. Putman, "Association of hemodynamic characteristics and cerebral aneurysm rupture," *American Journal of Neuroradiology*, vol. 32, pp. 264–270, Feb. 2011.

[16] L.-D. Jou, D. H. Lee, H. Morsi, and M. E. Mawad, "Wall shear stress on ruptured and unruptured intracranial aneurysms at the internal carotid artery," *American Journal of Neuroradiology*, vol. 29, pp. 1761–1767, Oct. 2008.

[17] M. Castro, C. Putman, A. Radaelli, A. F. Frangi, and J. Cebral, "Hemodynamics and rupture of terminal cerebral aneurysms," *Academic Radiology*, vol. 16, pp. 1201–1207, Oct. 2009.

[18] H. Zhu, Z. Ding, R. N. Piana, T. R. Gehrig, and M. H. Friedman, "Cataloguing the geometry of the human coronary arteries: A potential tool for predicting risk of coronary artery disease," *International Journal of Cardiology*, vol. 135, pp. 43–52, June 2009.

[19] S. A. Berger, L. Talbot, and L. S. Yao, "Flow in curved pipes," *Annual Review of Fluid Mechanics*, vol. 15, pp. 461–512, Jan. 1983.

[20] S.-W. Lee, L. Antiga, J. D. Spence, and D. A. Steinman, "Geometry of the carotid bifurcation predicts its exposure to disturbed flow," *Stroke*, vol. 39, no. 8, pp. 2341–2347, 2008.

[21] M. H. Friedman, O. J. Deters, F. F. Mark, C. B. Bargeron, and G. M. Hutchins, "Arterial geometry affects hemodynamics: A potential risk factor for atherosclerosis," *Atherosclerosis*, vol. 46, pp. 225–231, Feb. 1983.

[22] D. A. Steinman, "Image-based computational fluid dynamics modeling in realistic arterial geometries," *Annals of Biomedical Engineering*, vol. 30, pp. 483–497, Apr. 2002.

[23] T. Ingebrigtsen, M. K. Morgan, K. Faulder, L. Ingebrigtsen, T. Sparr, and H. Schirmer, "Bifurcation geometry and the presence of cerebral artery aneurysms," *Journal of Neurosurgery*, vol. 101, pp. 108–113, Jul 2004.

[24] Y. Hoi, M. Hui, S. H. Woodward, B. R. Bendok, R. A. Hanel, L. R. Guterman, and L. N. Hopkins, "Effects of arterial geometry on aneurysm growth: Three-dimensional computational fluid dynamics study," *Journal of Neurosurgery*, vol. 101, no. 4, pp. 676–681, 2004.

[25] T. Hassan, E. V. Timofeev, T. Saito, H. Shimizu, M. Ezura, Y. Matsumoto, K. Takayama, T. Tominaga, and A. Takashi, "A proposed parent vessel geometry-based categorization of saccular intracranial aneurysms: Computational flow dynamics analysis of the risk factors for lesion rupture," *Journal of Neurosurgery*, vol. 103, no. 4, pp. 662–680, 2005.

[26] H. Meng, Z. Wang, M. Kim, R. D. Ecker, and L. N. Hopkins, "Saccular aneurysms on straight and curved vessels are subject to different hemodynamics: Implications of intravascular stenting," *American Journal of Neuroradiology*, vol. 27, pp. 1861–1865, Oct. 2006.

[27] H. Meng, D. D. Swartz, Z. Wang, Y. Hoi, J. Kolega, E. M. Metaxa, M. P. Szymanski, J. Yamamoto, E. Sauvageau, and E. I. Levy, "A model system for mapping vascular responses to complex hemodynamics at arterial bifurcations in vivo," *Neurosurgery*, vol. 59, pp. 1094–1100, Nov. 2006.

[28] T. Hashimoto, H. Meng, and W. L. Young, "Intracranial aneurysms: Links among inflammation, hemodynamics and vascular remodeling," *Neurological Research*, vol. 28, pp. 372–380, June 2006.

[29] L. Gao, Y. Hoi, D. D. Swartz, J. Kolega, A. Siddiqui, and H. Meng, "Nascent aneurysm formation at the basilar terminus induced by hemodynamics," *Stroke*, vol. 39, pp. 2085–2090, July 2008.

[30] J. R. Cebral, F. Mut, J. Weir, and C. Putman, "Quantitative characterization of the hemodynamic environment in ruptured and unruptured brain aneurysms," *American Journal of Neuroradiology*, vol. 32, pp. 145–151, Jan. 2011.

[31] M. H. Friedman, "Variability of 3D arterial geometry and dynamics, and its pathologic implications," *Biorheology*, vol. 39, no. 3-4, pp. 513–517, 2002.

[32] J. Hendrikse, A. F. van Raamt, Y. van der Graaf, W. P. T. M. Mali, and J. van der Grond, "Distribution of cerebral blood flow in the circle of Willis," *Radiology*, vol. 235, pp. 184–189, Apr. 2005.

[33] H. Tanaka, N. Fujita, T. Enoki, K. Matsumoto, Y. Watanabe, K. Murase, and H. Nakamura, "Relationship between variations in the circle of Willis and flow rates in internal carotid and basilar arteries determined by means of magnetic resonance imaging with semi-automated lumen segmentation: Reference data from 125 healthy volunteers," *American Journal of Neuroradiology*, vol. 27, pp. 1770–1775, Sept. 2006.

[34] K. N. Kayembe, M. Sasahara, and F. Hazama, "Cerebral aneurysms and variations in the circle of Willis," *Stroke*, vol. 15, pp. 846–850, Sept. 1984.

[35] W. C. K. Wong and A. C. S. Chung, "Augmented vessels for quantitative analysis of vascular abnormalities and endovascular treatment planning," *IEEE Transactions on Medical Imaging*, vol. 25, pp. 665–684, June 2006.

[36] P. M. O'Flynn, G. O'Sullivan, and A. S. Pandit, "Methods for three-dimensional geometric characterization of the arterial vasculature," *Annals of Biomedical Engineering*, vol. 35, pp. 1368–1381, Aug. 2007.

[37] J. S. Kim, L. R. Caplan, and K. S. L. Wong, *Intracranial Atherosclerosis*. Wiley-Blackwell, 2008.

[38] N. Subramanian, T. Kesavadas, and K. Hoffmann, "Geometry-based metrics for planning of neuroendovascular therapy," in *Proc. 18th Int. Congress and Exhibition on Computer Assisted Radiology and Surgery (CARS), Chicago, USA* (H. U. Lemke, K. Inamura, K. Doi, M. W. Vannier, A. G. Farman, and J. H. C. Reiber, eds.), vol. 1268 of *Internationl Congress Series*, pp. 718–723, 2004.

[39] T. Kesavadas, "Configuration-space technique for calculating stent-fitness measures for the planning of neuro-endovascular interventions," in *Proc. SPIE Medical Imaging, San Diego, CA, USA* (R. L. Galloway jr. and K. R. Cleary, eds.), vol. 5744, pp. 191–199, SPIE Press, 2005.

[40] T. Abe, M. Hirohata, N. Tanaka, Y. Uchiyama, K. Fujimoto, N. Fujimura, A. M. Norbash, and N. Hayabuchi, "Distal-tip shape-consistency testing of steam-shaped microcatheters suitable for cerebral aneurysm coil placement," *American Journal of Neuroradiology*, vol. 25, pp. 1058–1061, June 2004.

[41] R. S. Pakbaz and C. W. Kerber, "Complex curve microcatheters for berry aneurysm endovascular therapy," *American Journal of Neuroradiology*, vol. 28, no. 1, pp. 179–180, 2007.

[42] S. Toyota, Y. Fujimoto, F. Iwamoto, A. Wakayama, and T. Yoshimine, "Technique for shaping microcatheter tips in coil embolization of paraclinoid aneurysms using full-scale volume rendering images of 3D rotational angiography," *Minimally Invasive Neurosurgery*, vol. 52, pp. 201–203, Aug. 2009.

[43] J. Y. Chueh, A. K. Wakhloo, and M. J. Gounis, "Neurovascular modeling: Small-batch manufacturing of silicone vascular replicas," *American Journal of Neuroradiology*, vol. 30, no. 6, pp. 1159–1164, 2009.

[44] M. K. Kole, D. M. Pelz, P. Kalapos, D. H. Lee, I. B. Gulka, and S. P. Lownie, "Endovascular coil embolization of intracranial aneurysms: Important factors related to rates and outcomes of incomplete occlusion," *Journal of Neurosurgery*, vol. 102, pp. 607–615, Apr. 2005.

[45] E. Bullitt, K. E. Muller, I. Jung, W. Lin, and S. Aylward, "Analyzing attributes of vessel populations," *Medical Image Analysis*, vol. 9, pp. 39–49, Feb. 2005.

[46] E. Bullitt, D. Zeng, B. Mortamet, A. Ghosh, S. R. Aylward, W. Lin, B. L. Marks, and K. Smith, "The effects of healthy aging on intracerebral blood vessels visualized by magnetic resonance angiography," *Neurobiology of Aging*, vol. 31, pp. 290–300, Feb. 2010.

[47] E. Bullitt, F. N. Rahman, J. K. Smith, E. Kim, D. Zeng, L. M. Katz, and B. L. Marks, "The effect of exercise on the cerebral vasculature of healthy aged subjects as visualized by MR angiography," *American Journal of Neuroradiology*, vol. 30, pp. 1857–1863, Nov. 2009.

[48] S. R. Aylward, J. Jomier, C. Vivert, V. LeDigarcher, and E. Bullitt, "Spatial graphs for intra-cranial vascular network characterization, generation, and discrimination," in *Proc. 8th Int. Conf. Medical Image Computing and Computer Assisted Intervention (MICCAI), Palm Springs, CA, USA* (J. S. Duncan and G. Gerig, eds.), vol. 3749 of *Lecture Notes in Computer Science*, pp. 59–66, Springer, 2005.

[49] A. H. Parikh, J. K. Smith, M. G. Ewend, and E. Bullitt, "Correlation of MR perfusion imaging and vessel tortuosity parameters in assessment of intracranial neoplasms," *Technology in Cancer Research Treatment*, vol. 3, pp. 585–590, Dec. 2004.

[50] E. Bullitt, D. Zeng, G. Gerig, S. Aylward, S. Joshi, J. K. Smith, W. Lin, and M. G. Ewend, "Vessel tortuosity and brain tumor malignancy: A blinded study," *Academic Radiology*, vol. 12, pp. 1232–1240, Oct. 2005.

[51] E. Bullitt, M. G. Ewend, S. Aylward, W. Lin, G. Gerig, S. Joshi, I. Jung, K. Muller, and K. Smith, "Abnormal vessel tortuosity as a marker of treatment response of malignant gliomas: Preliminary report," *Technology in Cancer Research Treatment*, vol. 3, pp. 577–584, Dec. 2004.

[52] E. Bullitt, N. U. Lin, J. K. Smith, D. Zeng, E. P. Winer, L. A. Carey, W. Lin, and M. G. Ewend, "Blood vessel morphologic changes depicted with MR angiography during treatment of brain metastases: A feasibility study," *Radiology*, vol. 245, pp. 824–830, Dec. 2007.

[53] J. Yang, L. X. Yu, M. Y. Rennie, J. G. Sled, and R. M. Henkelman, "Comparative structural and hemodynamic analysis of vascular trees," *American Journal of Physiology. Heart and Circulatory Physiology*, vol. 298, pp. H1249–H1259, Apr. 2010.

[54] E. Storkebaum and P. Carmeliet, "VEGF: a critical player in neurodegeneration," *The Journal of Clinical Investigation*, vol. 113, pp. 14–18, Jan. 2004.

[55] R. Del Bo, S. Ghezzi, E. Scarpini, N. Bresolin, and G. P. Comi, "VEGF genetic variability is associated with increased risk of developing Alzheimer's disease," *Journal of the Neurological Sciences*, vol. 283, pp. 66–68, Aug. 2009.

[56] L. Antiga and D. A. Steinman, "Robust and objective decomposition and mapping of bifurcating vessels," *IEEE Transactions on Medical Imaging*, vol. 23, pp. 704–713, June 2004.

[57] M. Piccinelli, A. Veneziani, D. A. Steinman, A. Remuzzi, and L. Antiga, "A framework for geometric analysis of vascular structures: Application to cerebral aneurysms," *IEEE Transactions on Medical Imaging*, vol. 28, pp. 1141–1155, Aug. 2009.

[58] H. Bogunovic, J. M. Pozo, R. Cardenes, M. C. Villa-Uriol, R. Blanc, M. Piotin, and A. F. Frangi, "Automated landmarking and geometric characterization of the carotid siphon," *Medical Image Analysis*, vol. 16, no. 4, pp. 889–903, 2012.

[59] B. A. Schueler, D. F. Kallmes, and H. J. Cloft, "3D cerebral angiography: Radiation dose comparison with digital subtraction angiography," *American Journal of Neuroradiology*, vol. 26, pp. 1898–1901, Sept. 2005.

[60] U. U. Ernemann, E. Gronewaller, F. B. Duffner, O. Guervit, J. Claassen, and M. D. Skalej, "Influence of geometric and hemodynamic parameters on aneurysm visualization during three-dimensional rotational angiography: An in vitro study," *American Journal of Neuroradiology*, vol. 24, pp. 597–603, Apr. 2003.

[61] T. Hirai, Y. Korogi, K. Ono, M. Yamura, S. Uemura, and Y. Yamashita, "Pseudostenosis phenomenon at volume-rendered three-dimensional digital angiography of intracranial arteries: Frequency, location, and effect on image evaluation," *Radiology*, vol. 232, pp. 882–887, Sept. 2004.

[62] L.-D. Jou, A. Mohamed, D. H. Lee, and M. E. Mawad, "3D rotational digital subtraction angiography may underestimate intracranial aneurysms: Findings from two basilar aneurysms," *American Journal of Neuroradiology*, vol. 28, pp. 1690–1692, Oct. 2007.

[63] M. M. Lell, K. Anders, M. Uder, E. Klotz, H. Ditt, F. Vega-Higuera, T. Boskamp, W. A. Bautz, and B. F. Tomandl, "New techniques in CT angiography," *RadioGraphics*, vol. 26, pp. S45–562, Oct. 2006.

[64] M. van Straten, H. W. Venema, G. J. Streekstra, C. B. L. M. Majoie, G. J. den Heeten, and C. A. Grimbergen, "Removal of bone in CT angiography of the cervical arteries by piecewise matched mask bone elimination," *Medical Physics*, vol. 31, pp. 2924–2933, Oct. 2004.

[65] H. A. F. Gratama van Andel, H. W. Venema, G. J. Streekstra, M. van Straten, C. B. L. M. Majoie, G. J. den Heeten, and C. A. Grimbergen, "Removal of bone in CT angiography by multiscale matched mask bone elimination," *Medical Physics*, vol. 34, p. 3711, Aug. 2007.

[66] M. Miyazaki and M. Akahane, "Non-contrast enhanced MR angiography: Established techniques," *Journal of Magnetic Resonance Imaging*, vol. 35, pp. 1–19, Jan. 2012.

[67] http://www.mr-tip.com.

[68] C. F. G. C. Geraldes and S. Laurent, "Classification and basic properties of contrast agents for magnetic resonance imaging," *Contrast Media & Molecular Imaging*, vol. 4, no. 1, pp. 1–23, 2009.

[69] E. Moser, F. Stahlberg, M. E. Ladd, and S. Trattnig, "7-T MR-from research to clinical applications?," *NMR in Biomedicine*, vol. 25, pp. 695–716, Nov. 2011.

[70] K. P. Pruessmann, M. Weiger, M. B. Scheidegger, and P. Boesiger, "SENSE: sensitivity encoding for fast MRI," *Magnetic Resonance in Medicine*, vol. 42, pp. 952–962, Nov. 1999.

[71] M. A. Griswold, P. M. Jakob, R. M. Heidemann, M. Nittka, V. Jellus, J. Wang, B. Kiefer, and A. Haase, "Generalized autocalibrating partially parallel acquisitions (GRAPPA)," *Magnetic Resonance in Medicine*, vol. 47, pp. 1202–1210, June 2002.

[72] C. Kirbas and F. Quek, "A review of vessel extraction techniques and algorithms," *ACM Computing Surveys*, vol. 36, pp. 81–121, June 2004.

[73] D. Lesage, E. D. Angelini, I. Bloch, and G. Funka-Lea, "A review of 3D vessel lumen segmentation techniques: Models, features and extraction schemes," *Medical Image Analysis*, vol. 13, no. 6, pp. 819–845, 2009.

[74] A. F. Frangi, W. J. Niessen, K. L. Vincken, and M. A. Viergever, "Multiscale vessel enhancement filtering," in *Proc. 1st Int. Conf. Medical Image Computing and Computer Assisted Intervention (MICCAI), Boston, MA, USA* (W. M. Wells, A. C. F. Colchester, and S. L. Delp, eds.), vol. 1496 of *Lecture Notes in Computer Science*, pp. 130–137, Springer, 1998.

[75] Y. Sato, S. Nakajima, N. Shiraga, H. Atsumi, S. Yoshida, T. Koller, G. Gerig, and R. Kikinis, "Three-dimensional multi-scale line filter for segmentation and visualization of curvilinear structures in medical images," *Medical Image Analysis*, vol. 2, pp. 143–168, June 1998.

[76] R. Manniesing, M. A. Viergever, and W. J. Niessen, "Vessel enhancing diffusion: A scale space representation of vessel structures," *Medical Image Analysis*, vol. 10, pp. 815–825, Dec. 2006.

[77] A. M. Mendrik, E.-J. Vonken, A. Rutten, M. A. Viergever, and B. van Ginneken, "Noise reduction in computed tomography scans using 3-D anisotropic hybrid diffusion with continuous switch," *IEEE Transactions on Medical Imaging*, vol. 28, pp. 1585–1594, Oct. 2009.

[78] M. Hernandez and A. F. Frangi, "Non-parametric geodesic active regions: Method and evaluation for cerebral aneurysms segmentation in 3DRA and CTA," *Medical Image Analysis*, vol. 11, pp. 224–241, June 2007.

[79] J. A. Sethian, *Level Set Methods and Fast Marching Methods*. Cambridge University Press, 1999.

[80] V. Caselles, R. Kimmel, and G. Sapiro, "Geodesic Active Contours," *International Journal of Computer Vision*, vol. 22, pp. 61–79, 1995.

[81] L. M. Lorigo, O. D. Faugeras, W. E. Grimson, R. Keriven, R. Kikinis, A. Nabavi, and C. F. Westin, "CURVES: curve evolution for vessel segmentation," *Medical Image Analysis*, vol. 5, pp. 195–206, Sept. 2001.

[82] R. Manniesing, B. K. Velthuis, M. S. van Leeuwen, I. C. van der Schaaf, P. J. van Laar, and W. J. Niessen, "Level set based cerebral vasculature segmentation and diameter quantification in CT angiography," *Medical Image Analysis*, vol. 10, pp. 200–214, Apr. 2006.

[83] K. Buhler, P. Felkel, and A. L. Cruz, "Geometric methods for vessel visualization and quantification – a survey," *Geometric Modelling for Scientific Visualization*, pp. 399–420, 2002.

[84] T. C. Lee, R. L. Kashyap, and C. N. Chu, "Building skeleton models via 3-D medial surface axis thinning algorithms," *CVGIP: Graphical Models and Image Processing*, vol. 56, pp. 462–478, Nov. 1994.

[85] S. Bouix, K. Siddiqi, and A. Tannenbaum, "Flux driven automatic centerline extraction," *Medical Image Analysis*, vol. 9, no. 3, pp. 209–221, 2005.

[86] M. S. Hassouna and A. A. Farag, "Variational curve skeletons using gradient vector flow," *IEEE Transactions on Pattern Analysis and Machine Intelligence*, vol. 31, pp. 2257–2274, Dec. 2009.

[87] H. Blum, "A transformation for extracting new descriptors of shape," *Models for the Perception of Speech and Visual Form*, vol. 19, no. 5, pp. 362–380, 1967.

[88] L. Antiga, B. Ene-Iordache, and A. Remuzzi, "Computational geometry for patient-specific reconstruction and meshing of blood vessels from MR and CT angiography," *IEEE Transactions on Medical Imaging*, vol. 22, pp. 674–684, May 2003.

[89] O. Wink, W. J. Niessen, and M. A. Viergever, "Fast delineation and visualization of vessels in 3-D angiographic images," *IEEE Transactions on Medical Imaging*, vol. 19, pp. 337–346, Apr. 2000.

[90] S. R. Aylward and E. Bullitt, "Initialization, noise, singularities, and scale in height ridge traversal for tubular object centerline extraction," *IEEE Transactions on Medical Imaging*, vol. 21, pp. 61–75, Feb. 2002.

[91] E. Bullitt, S. Aylward, K. Smith, S. Mukherji, M. Jiroutek, and K. Muller, "Symbolic description of intracerebral vessels segmented from magnetic resonance angiograms and evaluation by comparison with X-ray angiograms," *Medical Image Analysis*, vol. 5, pp. 157–169, June 2001.

[92] L. Risser, F. Plouraboue, and X. Descombes, "Gap filling of 3-D microvascular networks by tensor voting," *IEEE Transactions on Medical Imaging*, vol. 27, pp. 674–687, May 2008.

[93] I. Volkau, W. Zheng, R. Baimouratov, A. Aziz, and W. L. Nowinski, "Geometric modeling of the human normal cerebral arterial system," *IEEE Transactions on Medical Imaging*, vol. 24, pp. 529–539, Apr. 2005.

[94] J. Tschirren, G. McLennan, K. Palagyi, E. A. Hoffman, and M. Sonka, "Matching and anatomical labeling of human airway tree," *IEEE Transactions on Medical Imaging*, vol. 24, pp. 1540–1547, Dec. 2005.

[95] E. Bullitt, G. Gerig, S. M. Pizer, W. Lin, and S. R. Aylward, "Measuring tortuosity of the intracerebral vasculature from MRA images," *IEEE Transactions on Medical Imaging*, vol. 22, pp. 1163–1171, Sept. 2003.

[96] J. S. Gielecki, A. Zurada, G. Gajda, D. Nowak, and J. Sienkiewicz-Zawilinska, "The description of vascular variations in three-dimensional space: A novel method of spatial cerebral arteries evaluation," *Medical Science Monitor*, vol. 14, no. 9, p. MT36, 2008.

[97] A. Zurada, J. Gielecki, R. S. Tubbs, M. Loukas, W. Maksymowicz, A. A. Cohen-Gadol, M. Michalak, M. Chlebiej, and A. Zurada-Zielinska, "Three-dimensional morphometrical analysis of the M1 segment of the middle cerebral artery: Potential clinical and neurosurgical implications," *Clinical Anatomy*, vol. 24, pp. 34–46, Jan. 2011.

[98] G. Choi, C. P. Cheng, N. M. Wilson, and C. A. Taylor, "Methods for quantifying three-dimensional deformation of arteries due to pulsatile and nonpulsatile forces: Implications for the design of stents and stent grafts," *Annals of Biomedical Engineering*, vol. 37, pp. 14–33, Jan. 2009.

[99] K. E. Lee, K. H. Parker, C. G. Caro, and S. J. Sherwin, "The spectral/ hp element modelling of steady flow in non-planar double bends," *International Journal for Numerical Methods in Fluids*, vol. 57, no. 5, pp. 519–529, 2008.

[100] S. Meng, L. d. F. Costa, S. H. Geyer, M. P. Viana, C. Reiter, G. B. Muller, and W. J. Weninger, "Three-dimensional description and mathematical characterization of the parasellar internal carotid artery in human infants," *Journal of Anatomy*, vol. 212, pp. 636–644, May 2008.

[101] S. Meng, S. H. Geyer, L. d. F. Costa, M. P. Viana, and W. J. Weninger, "Objective characterization of the course of the parasellar internal carotid artery using mathematical tools," *Surgical and Radiologic Anatomy*, vol. 30, pp. 519–526, Aug. 2008.

[102] T. Boskamp, D. Rinck, F. Link, B. Kümmerlen, G. Stamm, and P. Mildenberger, "New vessel analysis tool for morphometric quantification and visualization of vessels in CT and MR imaging data sets," *RadioGraphics*, vol. 24, no. 1, pp. 287–297, 2004.

[103] J. Tschirren, E. A. Hoffman, G. McLennan, and M. Sonka, "Intrathoracic airway trees: Segmentation and airway morphology analysis from low-dose CT scans," *IEEE Transactions on Medical Imaging*, vol. 24, pp. 1529–1539, Dec. 2005.

[104] P. M. O'Flynn, G. O'Sullivan, and A. S. Pandit, "Geometric variability of the abdominal aorta and its major peripheral branches," *Annals of Biomedical Engineering*, vol. 38, pp. 824–840, Mar. 2010.

[105] A. Zurada and J. S. Gielecki, "A novel formula for the classification of blood vessels according to symmetry, asymmetry and hypoplasia," *Folia Morphologica*, vol. 66, pp. 339–345, Nov. 2007.

[106] A. Zurada, J. St Gielecki, R. S. Tubbs, M. Loukas, A. Zurada-Zielinska, W. Maksymowicz, D. Nowak, and A. A. Cohen-Gadol, "Three-dimensional morphometry of the A1 segment of the anterior cerebral artery with neurosurgical relevance," *Neurosurgery*, vol. 67, pp. 1768–1782, Dec. 2010.

[107] S. Giordana, S. J. Sherwin, J. Peiró, D. J. Doorly, Y. Papaharilaou, C. G. Caro, N. Watkins, N. Cheshire, M. Jackson, C. Bicknall, and V. Zervas, "Automated classification of peripheral distal by-pass geometries reconstructed from medical data," *Journal of Biomechanics*, vol. 38, pp. 47–62, Jan. 2005.

[108] P. Wang, C. Kelly, A. Harvey, N. Qayum, R. J. Muschel, and M. Brady, "Quantitative analysis of tumor vascular structure after drug treatment," *Proc. 32nd Ann. Int. Conf. IEEE Engineering in Medicine and Biology Society (EMBC), Buenos Aires, Argentina*, pp. 726–729, 2010.

[109] C. G. Caro, D. J. Doorly, M. Tarnawski, K. T. Scott, Q. Long, and C. L. Dumoulin, "Non-planar curvature and branching of arteries and non-planar-type flow," *Philosophical Transactions of the Royal Society A: Mathematical, Physical and Engineering Sciences*, vol. 452, pp. 185–197, Jan. 1996.

[110] M. E. Martinez-Perez, A. D. Hughes, A. V. Stanton, S. A. Thom, N. Chapman, A. A. Bharath, and K. H. Parker, "Retinal vascular tree morphology: A semi-automatic quantification," *IEEE Transactions on Biomedical Engineering*, vol. 49, pp. 912–917, Aug. 2002.

[111] D. Selle, B. Preim, A. Schenk, and H.-O. Peitgen, "Analysis of vasculature for liver surgical planning," *IEEE Transactions on Medical Imaging*, vol. 21, pp. 1344–1357, Nov. 2002.

[112] K. Palagyi, J. Tschirren, E. A. Hoffman, and M. Sonka, "Quantitative analysis of pulmonary airway tree structures," *Computers in Biology and Medicine*, vol. 36, pp. 974–996, Sept. 2006.

[113] U. Grenander and M. I. Miller, "Computational anatomy: An emerging discipline," *Quarterly of Applied Mathematics*, vol. 56, no. 4, pp. 617–694, 1998.

[114] G. E. Christensen, R. D. Rabbitt, and M. I. Miller, "Deformable templates using large deformation kinematics," *IEEE Transactions on Image Processing*, vol. 5, pp. 1435–1447, Jan. 1996.

[115] M. I. Miller, A. Trouve, and L. Younes, "On the metrics and Euler-Lagrange equations of computational anatomy," *Annual Review of Biomedical Engineering*, vol. 4, pp. 375–405, Jan. 2002.

[116] M. F. Beg, M. I. Miller, A. Trouve, and L. Younes, "Computing large deformation metric mappings via geodesic flows of diffeomorphisms," *International Journal of Computer Vision*, vol. 61, pp. 139–157, Feb. 2005.

[117] S. Sommer, M. Nielsen, F. Lauze, , and X. Pennec, "A multi-scale kernel bundle for LDDMM: Towards sparse deformation description across space and scales," in *Proc. 22st Int. Conf. Information Processing in Medical Imaging (IPMI), Kloster Irsee, Germany* (G. Szekely and H. K. Hahn, eds.), vol. 6801 of *Lecture Notes in Computer Science*, pp. 624–635, Springer, 2011.

[118] S. Durrleman, X. Pennec, A. Trouve, and N. Ayache, "Statistical models of sets of curves and surfaces based on currents," *Medical Image Analysis*, vol. 13, pp. 793–808, Oct. 2009.

[119] R. C. Eaves and A. J. Guarino, "Dunn's multiple comparison test," in *Encyclopedia of Measurement and Statistics* (N. J. Salkind and K. Rasmussen, eds.), SAGE Publications, Inc., 2007.

[120] J. Ashburner and S. Kloppel, "Multivariate models of inter-subject anatomical variability," *NeuroImage*, vol. 56, pp. 422–439, May 2011.

[121] C. M. Bishop, *Pattern Recognition and Machine Learning*. Springer, 2006.

[122] V. N. Vapnik, "An overview of statistical learning theory," *IEEE Transactions on Neural Networks*, vol. 10, pp. 988–999, Jan. 1999.

[123] P. Golland, W. Grimson, and R. Kikinis, "Statistical shape analysis using fixed topology skeletons: Corpus callosum study," in *Proc. 16th Int. Conf. Information Processing in Medical Imaging (IPMI), Visegrád, Hungary* (A. Kuba, M. Šáamal, and A. Todd-Pokropek, eds.), vol. 1613 of *Lecture Notes in Computer Science*, pp. 382–387, Springer, June 1999.

[124] P. Golland, W. E. L. Grimson, M. E. Shenton, and R. Kikinis, "Detection and analysis of statistical differences in anatomical shape," *Medical Image Analysis*, vol. 9, pp. 69–86, Feb. 2005.

[125] A. M. McKinney, C. S. Palmer, C. L. Truwit, A. Karagulle, and M. Teksam, "Detection of aneurysms by 64-section multidetector CT angiography in patients acutely suspected of having an intracranial aneurysm and comparison with digital subtraction and 3D rotational angiography," *American Journal of Neuroradiology*, vol. 29, pp. 594–602, Mar. 2008.

[126] W. J. van Rooij, M. E. Sprengers, A. N. de Gast, J. P. P. Peluso, and M. Sluzewski, "3D rotational angiography: The new gold standard in the detection of additional intracranial aneurysms," *American Journal of Neuroradiology*, vol. 29, pp. 976–979, May 2008.

[127] Y. Hiratsuka, H. Miki, I. Kiriyama, K. Kikuchi, S. Takahashi, I. Matsubara, K. Sadamoto, and T. Mochizuki, "Diagnosis of unruptured intracranial aneurysms: 3T MR angiography versus 64-channel multi-detector row CT angiography," *Magnetic Resonance in Medical Sciences*, vol. 7, no. 4, pp. 169–178, 2008.

[128] M. L. Raghavan, B. Ma, and R. E. Harbaugh, "Quantified aneurysm shape and rupture risk," *Journal of Neurosurgery*, vol. 102, pp. 355–362, Feb. 2005.

[129] R. D. Millan, L. Dempere-Marco, J. M. Pozo, J. R. Cebral, and A. F. Frangi, "Morphological characterization of intracranial aneurysms using 3-D moment invariants," *IEEE Transactions on Medical Imaging*, vol. 26, pp. 1270–1282, Sept. 2007.

[130] L. Antiga, M. Piccinelli, L. Botti, B. Ene-Iordache, A. Remuzzi, and D. A. Steinman, "An image-based modeling framework for patient-specific computational hemodynamics," *Medical and Biological Engineering and Computing*, vol. 46, pp. 1097–1112, Nov. 2008.

[131] R. Manniesing, M. A. Viergever, A. van der Lugt, and W. J. Niessen, "Cerebral arteries: Fully automated segmentation from CT angiography – a feasibility study," *Radiology*, vol. 247, no. 3, pp. 841–846, 2008.

[132] H. Bogunovic, A. G. Radaelli, M. De Craene, D. Delgado, and A. F. Frangi, "Image intensity standardization in 3D rotational angiography and its application to vascular segmentation," in *Proc. SPIE Medical Imaging, San Diego, CA, USA* (J. M. Reinhardt and J. P. W. Pluim, eds.), vol. 6914, SPIE Press, 2008. Article 691419.

[133] S. J. Osher and R. P. Fedkiw, *Level Set Methods and Dynamic Implicit Surfaces*. Springer-Verlag, 2002.

[134] I. Aizenberg, N. Aizenberg, and J. Vandewalle, *Multi-Valued and Universal Binary Neurons: Theory, Learning, Applications*. Kluwer Academic, 2000.

[135] L. G. Nyul and J. K. Udupa, "On standardizing the MR image intensity scale," *Magnetic Resonance in Medicine*, vol. 42, pp. 1072–1081, Dec. 1999.

[136] R. H. Byrd, P. Lu, J. Nocedal, and C. Zhu, "A limited memory algorithm for bound constrained optimization," *SIAM Journal on Scientific Computing*, vol. 16, no. 5, pp. 1190–1208, 1995.

[137] D. Rueckert, P. Aljabar, R. A. Heckemann, J. V. Hajnal, and A. Hammers, "Diffeomorphic registration using B-splines," in *Proc. 9th Int. Conf. Medical Image Computing and Computer Assisted Intervention (MICCAI), Copenhagen, Denmark* (R. Larsen, M. Nielsen, and J. Sporring, eds.), vol. 4191 of *Lecture Notes in Computer Science*, pp. 702–709, Springer, 2006.

[138] W. E. Lorensen and H. E. Cline, "Marching cubes: A high resolution 3D surface construction algorithm," *Computer Graphics*, vol. 21, pp. 163–169, July 1987.

[139] P. J. Besl and H. D. McKay, "A method for registration of 3-D shapes," *IEEE Transactions on Pattern Analysis and Machine Intelligence*, vol. 14, no. 2, pp. 239–256, 1992.

[140] J. K. Udupa, V. R. Leblanc, Y. Zhuge, C. Imielinska, H. Schmidt, L. M. Currie, B. E. Hirsch, and J. Woodburn, "A framework for evaluating image segmentation algorithms," *Computerized Medical Imaging and Graphics*, vol. 30, pp. 75–87, Mar. 2006.

[141] H.-H. Chang, G. R. Duckwiler, D. J. Valentino, and W. C. Chu, "Computer-assisted extraction of intracranial aneurysms on 3D rotational angiograms for computational fluid dynamics modeling," *Medical Physics*, vol. 36, no. 12, pp. 5612–5621, 2009.

[142] A. Firouzian, R. Manniesing, H. Z. Flach, R. Risselada, F. van Kooten, M. C. Sturkenboom, A. van der Lugt, and W. J. Niessen, "Intracranial aneurysm segmentation in 3D CT angiography: Method and quantitative validation with and without prior noise filtering," *European Journal of Radiology*, 2010. Article in Press.

[143] L. R. Dice, "Measures of the amount of ecologic association between species," *Ecology*, vol. 26, pp. 297–302, July 1945.

[144] H.-H. Chang, A. H. Zhuang, D. J. Valentino, and W.-C. Chu, "Performance measure characterization for evaluating neuroimage segmentation algorithms," *NeuroImage*, vol. 47, pp. 122–35, Aug. 2009.

[145] B. Carstensen, J. Simpson, and L. C. Gurrin, "Statistical models for assessing agreement in method comparison studies with replicate measurements," *The International Journal of Biostatistics*, vol. 4, no. 1, 2008. Article 16.

[146] V. Chalana and Y. Kim, "A methodology for evaluation of boundary detection algorithms on medical images," *IEEE Transactions on Medical Imaging*, vol. 16, pp. 642–652, Oct. 1997.

[147] M. Attene and B. Falcidieno, "ReMESH: an interactive environment to edit and repair triangle meshes," in *Proc. IEEE Int. Conf. on Shape Modeling and Applications (SMI), Matsushima, Japan*, pp. 271–276, IEEE Press, 2006.

[148] "MeshLab: an open source, portable, and extensible system for the processing and editing of unstructured 3D triangular meshes." `http://meshlab.sourceforge.net`, 2010.

[149] I. Larrabide, P. Omedas, Y. Martelli, X. Planes, M. Nieber, J. A. Moya, C. Butakoff, R. Sebastian, O. Camara, M. De Craene, B. H. Bijnens, and A. F. Frangi, "GIMIAS: an open source framework for efficient development of research tools and clinical prototypes," in *Proc. 5th Int. Workshop on Functional Imaging and Modeling of the Heart (FIMH), Nice, France* (N. Ayache, H. Delingette, and M. Sermesant, eds.), vol. 5528 of *Lecture Notes in Computer Science*, pp. 417–426, Springer, 2009.

[150] M. Piotin, P. Gailloud, L. Bidaut, S. Mandai, M. Muster, J. Moret, and D. A. Rufenacht, "CT angiography, MR angiography and rotational digital subtraction angiography for volumetric assessment of intracranial aneurysms. An experimental study," *Neuroradiology*, vol. 45, pp. 404–409, June 2003.

[151] M. A. Castro, C. M. Putman, and J. R. Cebral, "Patient-specific computational modeling of cerebral aneurysms with multiple avenues of flow from 3D rotational angiography images," *Academic Radiology*, vol. 13, pp. 811–821, July 2006.

[152] M. E. S. Sprengers, J. D. Schaafsma, W. J. van Rooij, R. van den Berg, G. J. E. Rinkel, E. M. Akkerman, S. P. Ferns, and C. B. L. M. Majoie, "Evaluation of the occlusion status of coiled intracranial aneurysms with MR angiography at 3T: Is contrast enhancement necessary?," *American Journal of Neuroradiology*, vol. 30, pp. 1665–1671, July 2009.

[153] L. M. J. Florack, B. M. ter Haar Romeny, J. J. Koenderink, and M. A. Viergever, "General intensity transformations and differential invariants," *Journal of Mathematical Imaging and Vision*, vol. 4, pp. 171–187, May 1994.

[154] C. Schmid and R. Mohr, "Local grayvalue invariants for image retrieval," *IEEE Transactions on Pattern Analysis and Machine Intelligence*, vol. 19, pp. 530–535, May 1997.

[155] R. M. Hoogeveen, C. J. Bakker, and M. A. Viergever, "Limits to the accuracy of vessel diameter measurement in MR angiography," *Journal of Magnetic Resonance Imaging*, vol. 8, no. 6, pp. 1228–1235, 1998.

[156] D. A. Halon, D. Sapoznikov, B. S. Lewis, and M. S. Gotsman, "Localization of lesions in the coronary circulation," *American Journal of Cardiology*, vol. 52, pp. 921–926, Nov. 1983.

[157] H. Krayenbuehl, M. G. Yasargil, and P. Huber, *Cerebral Angiography.* Thieme, 2nd edition ed., 1982.

[158] M. Piccinelli, S. Bacigaluppi, E. Boccardi, B. Ene-Iordache, A. Remuzzi, A. Veneziani, and L. Antiga, "Geometry of the ICA and recurrent patterns in location, orientation and rupture status of lateral aneurysms: An image-based computational study," *Neurosurgery*, vol. 68, pp. 1270–1285, May 2011.

[159] D.-W. Kim and S.-D. Kang, "Association between internal carotid artery morphometry and posterior communicating artery aneurysm," *Yonsei Medical Journal*, vol. 48, pp. 634–638, Aug. 2007.

[160] W.-J. Jiang, Y.-J. Wang, B. Du, S.-X. Wang, G.-H. Wang, M. Jin, and J.-P. Dai, "Stenting of symptomatic M1 stenosis of middle cerebral artery: An initial experience of 40 patients," *Stroke*, vol. 35, pp. 1375–1380, June 2004.

[161] S. Y. J. Chen, J. D. Carroll, and J. C. Messenger, "Quantitative analysis of reconstructed 3-D coronary arterial tree and intracoronary devices," *IEEE Transactions on Medical Imaging*, vol. 21, pp. 724–740, July 2002.

[162] L. M. Sangalli, P. Secchi, S. Vantini, and A. Veneziani, "A case study in exploratory functional data analysis: Geometrical features of the internal carotid artery," *Journal of the American Statistical Association*, vol. 104, no. 485, pp. 37–48, 2009.

[163] L. M. Sangalli, P. Secchi, S. Vantini, and V. Vitelli, "K-mean alignment for curve clustering," *Computational Statistics and Data Analysis*, vol. 54, pp. 1219–1233, May 2010.

[164] H. Bogunovic, J. M. Pozo, M. C. Villa-Uriol, C. B. L. M. Majoie, R. van den Berg, H. A. F. Gratama van Andel, J. M. Macho, J. Blasco, L. San Roman, and A. F. Frangi, "Automated segmentation of cerebral vasculature with aneurysms in 3DRA and TOF-MRA using geodesic active regions: An evaluation study," *Medical Physics*, vol. 38, pp. 210–222, Jan. 2011.

[165] R. Cardenes, H. Bogunovic, and A. F. Frangi, "Fast 3D centerline computation for tubular structures by front collapsing and fast marching," in *Proc. IEEE Int. Conf. on Image Processing (ICIP), Hong Kong*, pp. 4109–4112, IEEE Press, 2010.

[166] L. Antiga and D. A. Steinman, "VMTK: the Vascular Modeling Toolkit." `http://www.vmtk.org`, 2011.

[167] H. Bogunovic, J. M. Pozo, R. Cardenes, and A. F. Frangi, "Automatic identification of internal carotid artery from 3DRA images," in *Proc. 32nd Ann. Int. Conf. IEEE Engineering in Medicine and Biology Society (EMBC), Buenos Aires, Argentina*, pp. 5343–5346, IEEE Press, 2010.

[168] C.-C. Chang and C.-J. Lin, "LIBSVM: a library for support vector machines." http://www.csie.ntu.edu.tw/~cjlin/libsvm, 2011.

[169] R. L. Bishop, "There is more than one way to frame a curve," *The American Mathematical Monthly*, vol. 82, pp. 246–251, Mar. 1975.

[170] A. J. Hanson and H. Ma, "Quaternion frame approach to streamline visualization," *IEEE Transactions on Visualization and Computer Graphics*, vol. 1, pp. 164–174, June 1995.

[171] D. G. Kendall, D. Barden, T. K. Carne, and H. Le, *Shape and Shape Theory*. Wiley, 1999.

[172] L. Formaggia, A. Quarteroni, and A. Veneziani, *Cardiovascular Mathematics: Modeling and simulation of the circulatory system*. Springer, 2009.

[173] J. Glaunes, A. Qiu, M. I. Miller, and L. Younes, "Large deformation diffeomorphic metric curve mapping," *International Journal of Computer Vision*, vol. 80, pp. 317–336, Dec. 2008.

[174] S. C. Joshi and M. I. Miller, "Landmark matching via large deformation diffeomorphisms," *IEEE Transactions on Image Processing*, vol. 9, pp. 1357–70, Jan. 2000.

[175] J. M. Bland and D. G. Altman, "Statistical methods for assessing agreement between two methods of clinical measurement," *The Lancet*, vol. 327, pp. 307–310, Feb. 1986.

[176] P. T. Fletcher, C. Lu, S. M. Pizer, and S. Joshi, "Principal geodesic analysis for the study of nonlinear statistics of shape," *IEEE Transactions on Medical Imaging*, vol. 23, pp. 995–1005, Aug. 2004.

[177] E. Pekalska and R. P. W. Duin, *The Dissimilarity Representation for Pattern Recognition: Foundations and Applications*. World Scientific Publishing Company, 2005.

[178] S. Gerber, T. Tasdizen, P. T. Fletcher, S. Joshi, and R. Whitaker, "Manifold modeling for brain population analysis," *Medical Image Analysis*, vol. 14, pp. 643–653, Oct. 2010.

[179] M. J. Hartkamp and J. van der Grond, "Investigation of the circle of Willis using MR angiography," *Medicamundi*, vol. 44, pp. 20–27, Mar. 2000.

[180] S. J. Dimmick and K. C. Faulder, "Normal variants of the cerebral circulation at multidetector CT angiography," *RadioGraphics*, vol. 29, pp. 1027–1043, Jan. 2009.

[181] J. R. Cebral, M. A. Castro, J. E. Burgess, R. S. Pergolizzi, M. J. Sheridan, and C. M. Putman, "Characterization of cerebral aneurysms for assessing risk of rupture by using patient-specific computational hemodynamics models," *American Journal of Neuroradiology*, vol. 26, no. 10, pp. 2550–2559, 2005.

[182] H. Bogunovic, J. M. Pozo, R. Cardenes, and A. F. Frangi, "Anatomical labeling of the anterior circulation of the circle of Willis using maximum a posteriori classification," in *Proc. 14th Int. Conf. Medical Image Computing and Computer Assisted Intervention (MICCAI), Toronto, ON, Canada* (G. Fichtinger, A. Martel, and T. Peters, eds.), vol. 6893 of *Lecture Notes in Computer Science*, pp. 330–337, Springer, 2011.

[183] A. Charnoz, V. Agnus, G. Malandain, L. Soler, and M. Tajine, "Tree matching applied to vascular system," in *Proc. 5th IAPR Int. Workshop on Graph-based Representations (GbRPR), Poitiers, France* (L. Brun and M. Vento, eds.), vol. 3434 of *Lecture Notes in Computer Science*, pp. 183–192, Springer, 2005.

[184] J. N. Kaftan, "A novel multipurpose tree and path matching algorithm with application to airway trees," in *Proc. SPIE Medical Imaging, San Diego, CA, USA* (A. Manduca and A. A. Amini, eds.), vol. 6143, pp. 215–224, SPIE Press, 2006. Article 61430N.

[185] J. H. Metzen, T. Kröger, A. Schenk, S. Zidowitz, H.-O. Peitgen, and X. Jiang, "Matching of anatomical tree structures for registration of medical images," *Image & Vision Computing*, vol. 27, pp. 923–933, June 2009.

[186] C. Oyarzun Laura and K. Drechsler, "Computer assisted matching of anatomical vessel trees," *Computers & Graphics*, vol. 35, pp. 299–311, Apr. 2011.

[187] T. Lohe, T. Kroger, S. Zidowitz, H. Peitgen, and X. Jiang, "Hierarchical matching of anatomical trees for medical image registration," in *Proc. Int. Conf. Medical Biometrics*, vol. 4901 of *Lecture Notes in Computer Science*, pp. 224–231, Springer, 2007.

[188] M. W. Graham and W. E. Higgins, "Optimal graph-theoretic approach to 3D anatomical tree matching," in *Proc. IEEE Int. Symp. on Biomedical Imaging (ISBI), Arlington, VA, USA*, pp. 109–112, IEEE Press, 2006.

[189] D. Smeets, P. Bruyninckx, J. Keustermans, D. Vandermeulen, and P. Suetens, "Robust matching of 3D lung vessel trees," in *Third International Workshop on Pulmonary Image Analysis*, pp. 61–70, 2010.

[190] T. Bülow, C. Lorenz, R. Wiemker, and J. Honko, "Point based methods for automatic bronchial tree matching and labeling," in *Proc. SPIE Medical Imaging, San Diego, CA, USA* (A. Manduca and A. A. Amini, eds.), vol. 6143, SPIE Press, 2006. Article 61430O.

[191] A. Feragen, P. Lo, V. Gorbunova, M. Nielsen, A. Dirksen, J. Reinhardt, F. Lauze, and M. de Bruijne, "An airway tree-shape model for geodesic airway branch labeling," in *Proc. 3rd Workshop on Mathematical Foundations of Computational Anatomy (MFCA), Toronto, Canada*, pp. 123–134, 2011.

[192] M. W. Graham, *Robust Graph-Theoretic Methods for Matching and Labeling Anatomical Trees*. PhD thesis, The Pennsylvania State University, 2006.

[193] B. van Ginneken, W. Baggerman, and E. M. van Rikxoort, "Robust segmentation and anatomical labeling of the airway tree from thoracic CT scans," in *Proc. 11th Int. Conf. Medical Image Computing and Computer Assisted Intervention (MICCAI), New York, NY, USA* (D. Metaxas, L. Axel, G. Fichtinger, and G. Szekely, eds.), vol. 5241 of *Lecture Notes in Computer Science*, pp. 219–226, Springer, 2008.

[194] K. Mori, S. Ota, D. Deguchi, T. Kitasaka, Y. Suenaga, S. Iwano, Y. Hasegawa, H. Takabatake, M. Mori, and H. Natori, "Automated anatomical labeling of bronchial branches extracted from CT datasets based on machine learning and combination optimization and its application to bronchoscope guidance.," in *Proc. 12th Int. Conf. Medical Image Computing and Computer Assisted Intervention (MICCAI), London, United Kingdom* (G.-Z. Yang, D. Hawkes, D. Rueckert, A. Noble, and C. Taylor, eds.), vol. 5762 of *Lecture Notes in Computer Science*, pp. 707–714, Springer, 2009.

[195] K. Mori, J. Hasegawa, Y. Suenaga, and J. Toriwaki, "Automated anatomical labeling of the bronchial branch and its application to the virtual bronchoscopy system," *IEEE Transactions on Medical Imaging*, vol. 19, pp. 103–114, Feb. 2000.

[196] S. Ota, D. Deguchi, T. Kitasaka, K. Mori, Y. Suenaga, Y. Hasegawa, K. Imaizumi, H. Takabatake, M. Mori, and H. Natori, "Augmented display of anatomical names of bronchial branches for bronchoscopy assistance," in *Proc. 4th Int. Workshop on Medical Imaging and Augmented Reality (MIAR), Tokyo, Japan* (T. Dohi, I. Sakuma, and H. Liao, eds.), vol. 5128 of *Lecture Notes in Computer Science*, pp. 377–384, Springer, 2008.

[197] K. Mori, M. Oda, T. Egusa, Z. Jiang, T. Kitasaka, M. Fujiwara, and K. Misawa, "Automated nomenclature of upper abdominal arteries for displaying anatomical names on virtual laparoscopic images," in *Proc. 5th Int. Workshop on Medical Imaging and Augmented Reality (MIAR), Beijing, China* (H. Liao, E. Edwards, X. Pan, Y. Fan, and G.-Z. Yang, eds.), vol. 6326 of *Lecture Notes in Computer Science*, pp. 353–362, Springer, 2010.

[198] W. Tang and A. Chung, "Cerebral vascular tree matching of 3D-RA data based on tree edit distance," in *Proc. 3rd Int. Workshop on Medical Imaging and Augmented Reality (MIAR), Shanghai, China* (G.-Z. Yang, T. Jiang, D. Shen, L. Gu, and J. Yang, eds.), vol. 4091 of *Lecture Notes in Computer Science*, pp. 116–123, Springer, 2006.

[199] Y. Uchiyama, M. Yamauchi, H. Ando, R. Yokoyama, T. Hara, H. Fujita, T. Iwama, and H. Hoshi, "Automated classification of cerebral arteries in MRA images and its application to maximum intensity projection," in *Proc. 28th Ann. Int. Conf. IEEE Engineering in Medicine and Biology Society (EMBC), New York, NY, USA*, pp. 4865–4868, IEEE press, 2006.

[200] "TubeTK: Segmentation, registration, and analysis of tubular strucutres in images." `http://public.kitware.com/Wiki/TubeTK`, 2011.

[201] R. Cardenes, J. L. Diez, H. Bogunovic, I. Larrabide, and A. F. Frangi, "3D modeling coronary artery bifurcations from CTA and conventional coronary angiography," in *Proc. 14th Int. Conf. Medical Image Computing and Computer Assisted Intervention (MICCAI), Toronto, ON, Canada* (G. Fichtinger, A. Martel, and T. Peters, eds.), vol. 6893 of *Lecture Notes in Computer Science*, pp. 395–402, Springer, 2011.

[202] X. Han, C. Xu, and J. L. Prince, "A topology preserving level set method for geometric deformable models," *IEEE Transactions on Pattern Analysis and Machine Intelligence*, vol. 25, pp. 755–768, June 2003.

[203] D. H. Ballard and C. M. Brown, *Computer Vision*. Prentice Hall, 1982.

[204] M. Pelillo, K. Siddiqi, and S. W. Zucker, "Matching hierarchical structures using association graphs," *IEEE Transactions on Pattern Analysis and Machine Intelligence*, vol. 21, pp. 1105–1120, Nov. 1999.

[205] I. M. Bomze, M. Budinich, P. M. Pardalos, and M. Pelillo, "The maximum clique problem," in *Handbook of Combinatorial Optimization* (D.-Z. Du and P. M. Pardalos, eds.), vol. 4, pp. 1–74, Kluwer Academic, 1999.

[206] E. Tomita, A. Tanaka, and H. Takahashi, "The worst-case time complexity for generating all maximal cliques and computational experiments," *Theoretical Computer Science*, vol. 363, pp. 28–42, Oct. 2006.

[207] N. Tanriover, M. Kawashima, A. L. Rhoton, A. J. Ulm, and R. A. Mericle, "Microsurgical anatomy of the early branches of the middle cerebral artery: morphometric analysis and classification with angiographic correlation," *Journal of Neurosurgery*, vol. 98, pp. 1277–1290, June 2003.

[208] A. J. Ulm, G. L. Fautheree, N. Tanriover, A. Russo, E. Albanese, A. L. Rhoton, R. A. Mericle, and S. B. Lewis, "Microsurgical and angiographic anatomy of middle cerebral artery aneurysms: prevalence and significance of early branch aneurysms," *Neurosurgery*, vol. 62, pp. 344–352, May 2008.

[209] S. M. Pizer, P. T. Fletcher, S. Joshi, A. Thall, J. Z. Chen, Y. Fridman, D. S. Fritsch, A. G. Gash, J. M. Glotzer, M. R. Jiroutek, C. Lu, K. E. Muller, G. Tracton, P. Yushkevich, and E. L. Chaney, "Deformable M-Reps for 3D medical image segmentation," *International Journal of Computer Vision*, vol. 55, pp. 85–106, Nov. 2003.

[210] K. Siddiqi and S. Pizer, *Medial Representations: Mathematics, Algorithms and Applications*. Springer, 2008.

[211] "@neurIST - Integrated biomedical informatics for the management of cerebral aneurysms. european union's 6th framework program (FP6). Project Identifier: FP6-IST-027703." `http://www.aneurist.org`.

[212] T. Passerini, L. M. Sangalli, S. Vantini, M. Piccinelli, S. Bacigaluppi, L. Antiga, E. Boccardi, P. Secchi, and A. Veneziani, "An integrated statistical investigation of the internal carotid arteries hosting cerebral aneurysms," Tech. Rep. TR-2011-009, Emory University, 2011.

[213] J. R. Cebral, M. A. Castro, O. Soto, R. Löhner, and N. Alperin, "Blood-flow models of the circle of Willis from magnetic resonance data," *Journal of Engineering Mathematics*, vol. 47, pp. 369–386, 2003.

[214] S. Moore, T. David, J. G. Chase, J. Arnold, and J. Fink, "3D models of blood flow in the cerebral vasculature," *Journal of Biomechanics*, vol. 39, no. 8, pp. 1454–1463, 2006.

[215] M. S. Alnaes, J. Isaksen, K.-A. Mardal, B. Romner, M. K. Morgan, and T. Ingebrigtsen, "Computation of hemodynamics in the circle of Willis," *Stroke*, vol. 38, pp. 2500–2505, Sept. 2007.

[216] F. Mut, S. Wright, G. Ascoli, and J. Cebral, "Characterization of the morphometry and hemodynamics of cerebral arterial trees in humans: A preliminary study," in *Proc. 2nd Int. Conf. on Computational and Mathematical Biomedical Engineering (CMBE)* (P. Nithiarasu and R. Lohner, eds.), pp. 87–90, 2011.

[217] J. R. Cebral, C. M. Putman, M. T. Alley, T. Hope, R. Bammer, and F. Calamante, "Hemodynamics in normal cerebral arteries: Qualitative comparison of 4D phase-contrast magnetic resonance and image-based computational fluid dynamics," *Journal of Engineering Mathematics*, vol. 64, pp. 367–378, Jan. 2009.

[218] M. I. Miller and A. Qiu, "The emerging discipline of Computational Functional Anatomy," *NeuroImage*, vol. 45, pp. S16–539, Mar. 2009.

[219] H. Wang and J. S. Marron, "Object oriented data analysis: Sets of trees," *Annals of Statistics*, vol. 35, pp. 1849–1873, Oct. 2007.

[220] A. Feragen, F. Lauze, P. Lo, M. de Bruijne, and M. Nielsen, "Geometries on spaces of treelike shapes," in *Proc. Asian Conference on Computer Vision (ACCV)*, pp. 160–173, Nov. 2010.

[221] A. Feragen, S. Hauberg, M. Nielsen, and F. Lauze, "Means in spaces of treelike shapes," in *Proc. 13th IEEE Int. Conf. on Computer Vision (ICCV), Barcelona, Spain*, pp. 736–746, IEEE Press, 2011.

[222] B. Aydin, G. Pataki, H. Wang, E. Bullitt, and J. S. Marron, "A principal component analysis for trees," *The Annals of Applied Statistics*, vol. 3, pp. 1597–1615, Dec. 2009.

List of Thesis Publications

Journal articles

1. **H. Bogunović**, J.M. Pozo, R. Cárdenes, L. San Román, and A.F. Frangi: Anatomical labeling of the Circle of Willis using maximum a posteriori estimation. *Submitted*.
2. I. Larrabide, M.C. Villa-Uriol, R. Cárdenes, V. Barbarito, L. Carotenuto, A. J. Geers, H. G. Morales, J. M. Pozo, M. D. Mazzeo, **H. Bogunović**, P. Omedas, C. Riccobene, J. M. Macho, A. F. Frangi: AngioLab - a software tool for morphological analysis and endovascular treatment planning of intracranial aneurysms. *Computer Methods and Programs in Biomedicine*, accepted.
3. **H. Bogunović**, J. M. Pozo, R. Cárdenes, M. C. Villa-Uriol, R. Blanc, M. Piotin, and A. F. Frangi: Automated landmarking and geometric characterization of the carotid siphon. *Medical Image Analysis*, vol. 16(4), May 2012, pp. 889-903.
4. R. Cárdenes, J. Pozo, **H. Bogunović**, I Larrabide, A.F. Frangi: Automatic aneurysm neck detection using surface Voronoi diagrams. *IEEE Transactions on Medical Imaging*, vol. 30(10), Oct. 2011, pp. 1863-1876.
5. A.J. Geers, I. Larrabide, A.G. Radaelli, **H. Bogunović**, M. Kim, H.A.F. Gratama van Andel, C.B. Majoie, E. VanBavel, A.F. Frangi: Patient-specific computational hemodynamics of intracranial aneurysms from 3DRA and CTA: an in vivo reproducibility study. *AJNR American Journal of Neuroradiology*, vol. 32(3), Mar. 2011, pp. 581-586.
6. **H. Bogunović**, J.M. Pozo, M.C. Villa-Uriol, C.B.L.M. Majoie, R. Van Den Berg, H.A.F. Gratama Van Andel, J.M. Macho, J. Blasco, L. San Román, A.F. Frangi: Automated segmentation of cerebral vasculature with aneurysms in 3DRA and TOF-MRA using geodesic active regions: an evaluation study. *Medical Physics*, vol. 38(1), Jan. 2011, pp. 210-222.
7. M.C. Villa-Uriol, I. Larrabide, J.M. Pozo, M. Kim, O. Cámara, M. De Craene, C. Zhang, A.J. Geers, H. Morales, **H. Bogunović**, R. Cárdenes and A.F. Frangi: Toward integrated management of cerebral aneurysms. *Philosophical Transactions of the Royal Society A*, vol. 368(1921), June 2010, pp. 2961-2982.
8. M. Schaap, C.T. Metz, T. van Walsum, A.G. van der Giessen, A.C. Weustink, N.R. Mollet, C. Bauer, **H. Bogunović**, C. Castro, X. Deng, E. Dikici, T. O'Donnell, M. Frenay, O. Friman, M. Hernandez Hoyos, P.H. Kitslaar, K. Krissian, C. Kuhnel, M.A. Luengo-Oroz, M. Orkisz, O. Smedby, M. Styner, A. Szymczak, H. Tek, C. Wang, S.K. Warfield, S. Zambal, Y. Zhang, G.P. Krestin, W.J. Niessen: Standardized evaluation methodology and reference database for evaluating coronary artery centerline extraction algorithms. *Medical Image Analysis*, vol. 13(5), Oct. 2009, pp. 701-714.

Book chapters

1. M.C. Villa-Uriol, I. Larrabide, J.M. Pozo, M. Kim, M. De Craene, O. Cámara, C. Zhang, A. J. Geers, **H. Bogunović**, H. Morales and A.F. Frangi: Cerebral aneurysms: a patient-dpecific and image-based management pipeline. In *Computational Vision and Medical Image Processing* (João Manuel R.S. Tavares and R.M. Natal Jorge, eds.), Springer, 2011, pp. 327-349.

Conference articles

1. **H. Bogunović**, J. M. Pozo, R. Cárdenes and A.F. Frangi: Anatomical labeling of the anterior circulation of the Circle of Willis using maximum a posteriori classification. *14th International Conference on Medical Image Computing and Computer Assisted Intervention (MICCAI)*, volume 6892 of Lecture Notes in Computer Science, part II (G. Fichtinger, A.L. Martel, T.M. Peters, eds.), pp. 330-337, Toronto, Canada, 2011.
2. R. Cárdenes, J.L. Diez, **H. Bogunović**, I. Larrabide, A.F. Frangi: 3D modeling coronary artery bifurcations from CTA and conventional coronary angiography. *14th International Conference on Medical Image Computing and Computer Assisted Intervention (MICCAI)*, volume 6893 of Lecture Notes in Computer Science, part III (G. Fichtinger, A.L. Martel, T.M. Peters, eds.), pp. 395-402, Toronto, Canada, 2011.
3. R. Cárdenes, **H. Bogunović**, A.F. Frangi: Fast 3D centerline computation for tubular structures by front collapsing and fast marching. *IEEE International Conference on Image Processing (ICIP)*, Hong Kong, China, 2010.
4. **H. Bogunović**, J.M. Pozo, R. Cárdenes, A.F. Frangi: Automatic identification of internal carotid artery from 3DRA images. *32nd International Conference of the IEEE Engineering in Medicine and Biology Society (EMBC)*, Buenos Aires, Argentina, 2010.
5. M.C. Villa-Uriol, I. Larrabide, J. Pozo, **H. Bogunović**, P. Omedas, V. Barbarito, L. Carotenuto, C. Riccobene, X. Planes, Y. Martelli, A.J. Geers, A.F. Frangi: AngioLab: integrated technology for patient-specific management of intracranial aneurysms. *32nd International Conference of the IEEE Engineering in Medicine and Biology Society (EMBC)*, Buenos Aires, Argentina, 2010.
6. V. Barbarito, L. Carotenuto, I. Larrabide, M.C. Villa-Uriol, C. Riccobene, X. Planes, Y. Martelli, P. Omedas, J.M. Pozo, M.D. Mazzeo, R. Cárdenes, **H. Bogunović**, A.F Frangi: A software framework for research on intracranial aneurysm management and treatment risk assessment. *VPH Conference*, Brussels, Belgium, 2010.
7. A.J. Geers, I. Larrabide, A.G. Radaelli, **H. Bogunović**, H.A.F. Gratama van Andel, C.B. Majoie, A.F. Frangi: Reproducibility of image-based computational hemodynamics in intracranial aneurysms: comparison of CTA and 3DRA. *IEEE International Symposium on Biomedical Imaging (ISBI)*, Boston, USA, 2009.
8. K. Krissian, **H. Bogunović**, J.M. Pozo, M.C. Villa-Uriol, A.F. Frangi: Minimally interactive knowledge-based coronary tracking in CTA using a minimal cost path. *The Midas Journal - Grand Challenge Coronary Artery Tracking (MICCAI Workshop)*, New York, USA, 2008, `http://hdl.handle.net/10380/1435`.
9. **H. Bogunović**, A. Radaelli, M. De Craene, D. Delgado and A.F. Frangi: Image intensity standardization in 3D rotational angiography and its application to vascular segmentation. *SPIE Medical Imaging 2008: Image Processing*, article 691419, San Diego, USA, 2008.

Conference abstracts

1. R. Blanc, **H. Bogunović**, S. Pistocchi, J.M. Pozo, M.C. Villa-Uriol, A.F. Frangi, M. Piotin: Automated geometrical characterization of the carotid siphon based on 3D rotational angiogram. *49th Annual Meeting & the Foundation of the ASNR Symposium*, Seattle, USA, 2011.

Biography

Hrvoje Bogunović graduated with the Diploma of Engineering degree in Computing from the Faculty of Electrical Engineering and Computing (FER) at the University of Zagreb in 2001. After graduation he stayed as a research and teaching assistant at the University of Zagreb where he received the Master of Science degree in Computing in 2005. In 2006, he joined the Center for Computational Imaging and Simulation Technologies in Biomedicine (CISTIB) at the Universitat Pompeu Fabra (UPF), as a PhD student and teaching assistant, where he worked in the field of segmentation and geometric characterization of the cerebral vasculature. His research interests are in medical image and shape analysis, machine learning and computer vision.

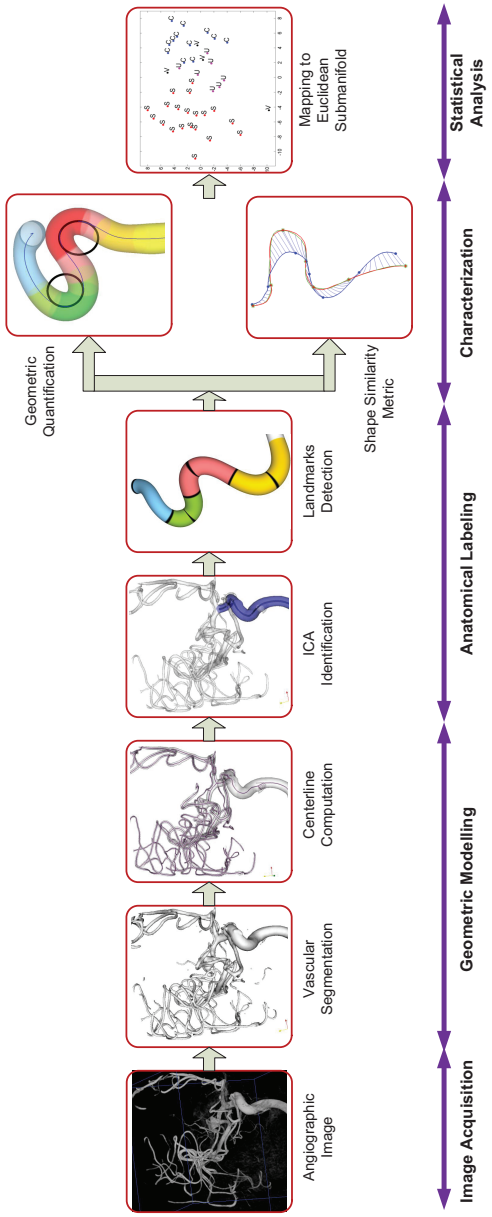

Figure 1.2, page 7: Pipeline for geometric characterization of internal carotid artery.

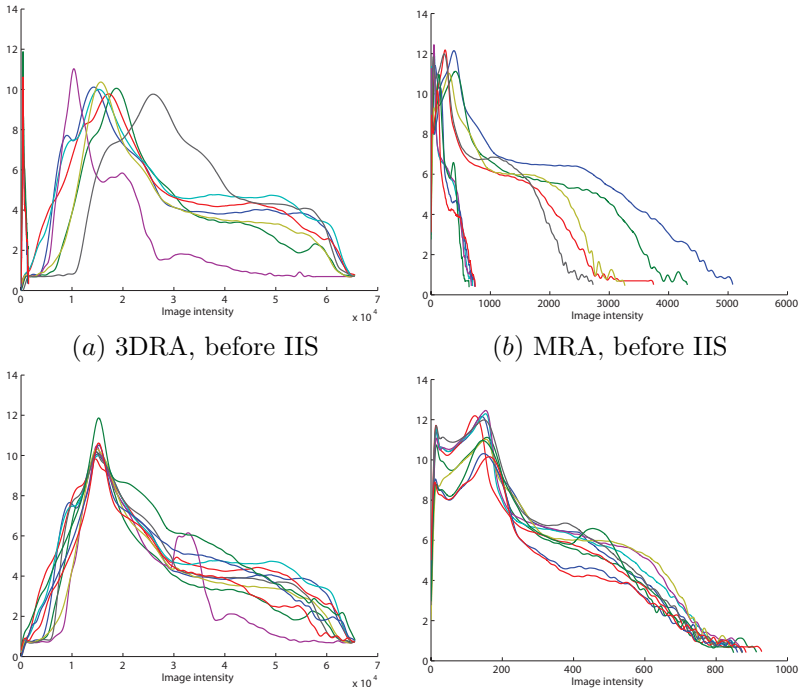

(*a*) 3DRA, before IIS (*b*) MRA, before IIS

(*c*) 3DRA, after IIS (*d*) MRA, after IIS

Figure 2.2, page 23: Image histograms of the 10 patients before (a, b) and after (c, d) image intensity standardization of 3DRA (a, c) and MRA (b, d) images. The logarithm of histogram values is displayed.

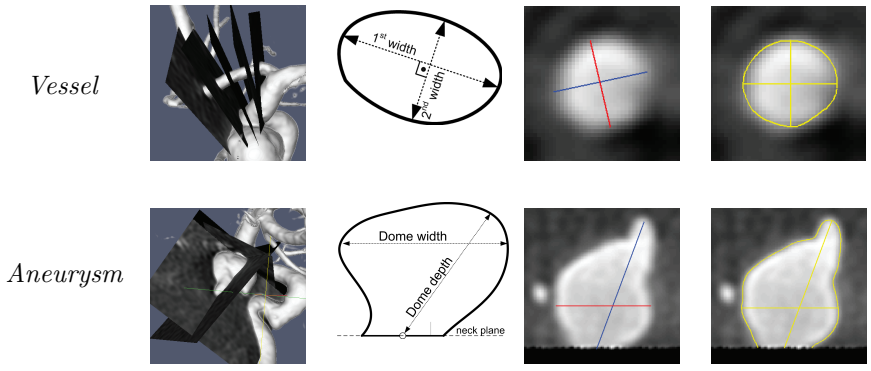

(*a*) (*b*) (*c*) (*d*)

Figure 2.3, page 24: (a) Positioning of cutting planes. (b) For measuring vessels and aneurysm neck the two measuring segments need to be orthogonal to each other (1^{st} width is chosen first) and located where the width is maximum. Dome depth is the distance from the neck center to the farthest point on the dome, while dome width is the length of the longest chord of the dome parallel to the neck plane. (c) Example of manual measurements. (d) Example of automated measurements.

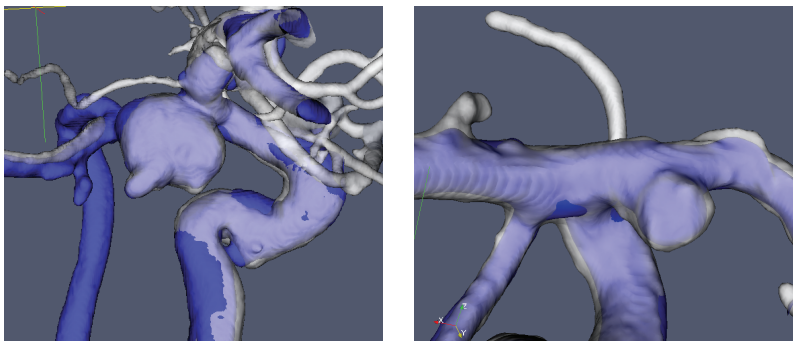

(a) (b)

Figure 2.4, page 25: Examples of the registered surfaces from the two modalities 3DRA (in white) and MRA (in blue).

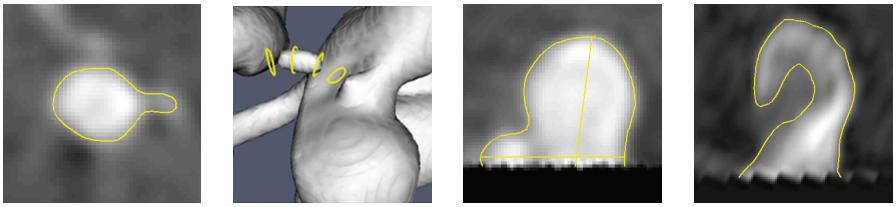

(a) (b) (c) (d)

Figure 2.5, page 28: Examples of qualitative errors: Touching vessel effect (a), missing vessel effect (b), wide aneurysm neck (c) and indented aneurysm (d).

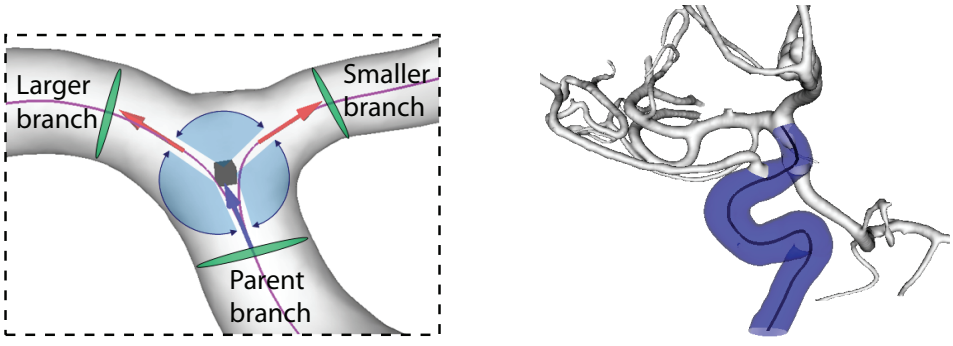

(a) **(b)**

Figure 3.4, page 45: (a) Bifurcation characterization: Origin (black cube) and associated bifurcation vectors. (b) Example of identified ICA and its centerline.

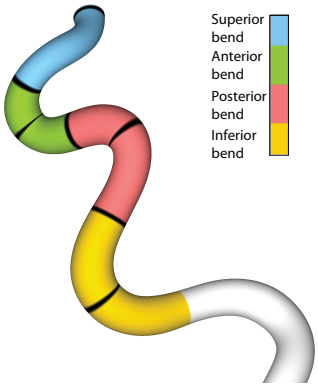

Figure 3.5, page 46: Carotid siphon with the four bends (in color) and the seven landmarks (in black). White area denotes: outside the region of interest.

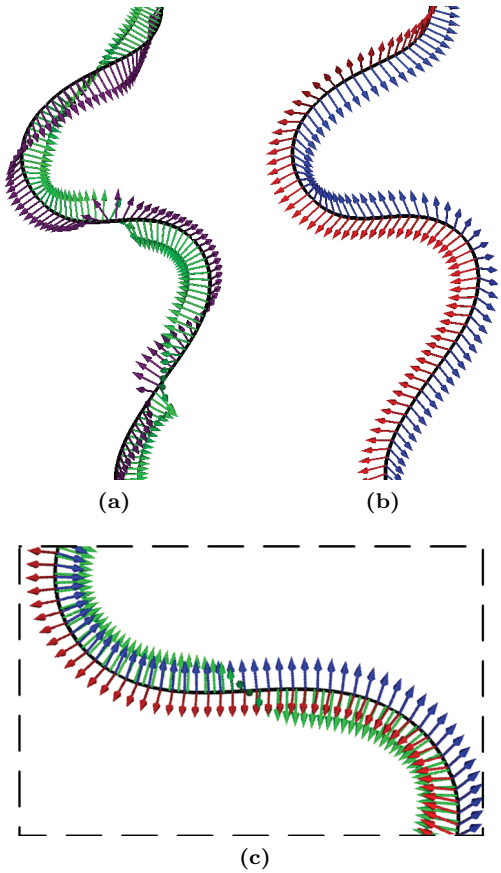

Figure 3.6, page 47: Centerline spatial curve with: (a) Frenet-Serret frame with normal $\vec{N}$ (green) and binormal $\vec{B}$ (purple) vectors. (b) Parallel transport frame with $\vec{E_1}$ and $\vec{E_2}$ (red and blue). (c) Normal vector $\vec{N}$ in the region of bend transition changes the orientation with respect to $\vec{E_1}$ and $\vec{E_2}$.

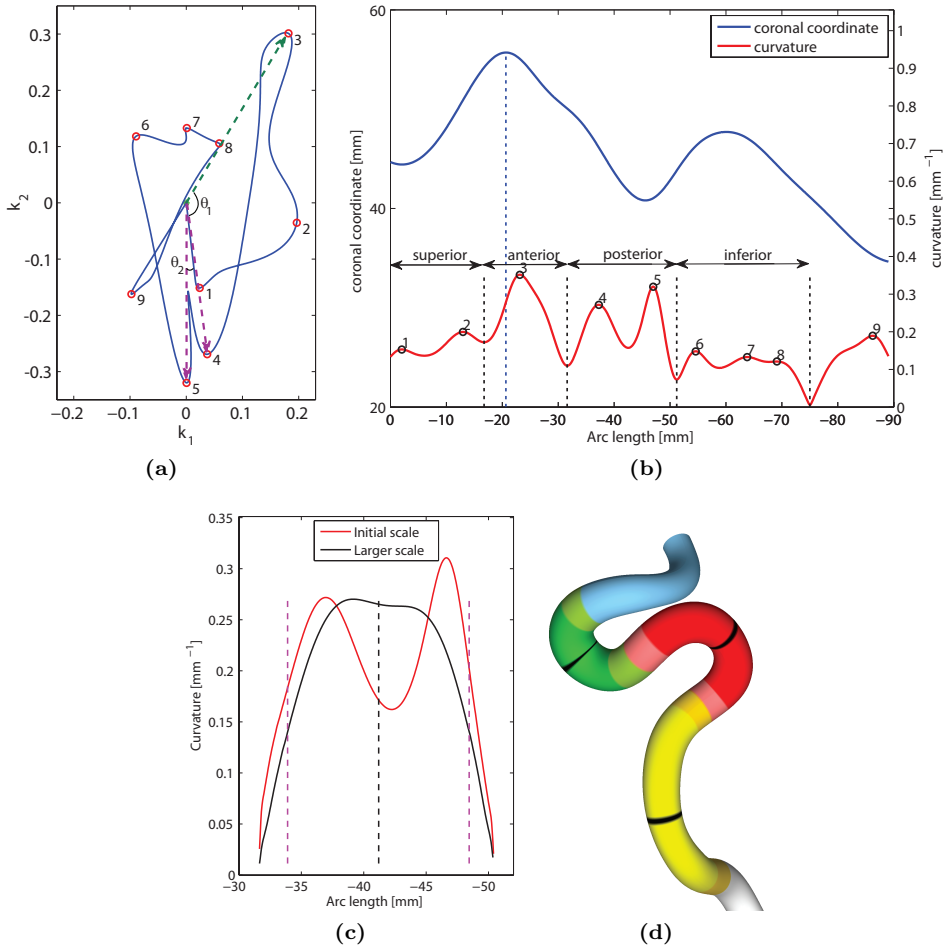

Figure 3.8, page 50: Bends and landmarks detection: (a) (k_1, k_2) space of the centerline. Numbers denote the curvature peaks sequentially starting from ICA-TB. Between points 3 and 4 ($\theta_1 \approx 120°$) there is a transition of bends. Points 4 and 5 ($\theta_2 \approx 20°$) belong to the same bend (posterior). (b) Coronal coordinate and the curvature of the centerline. The global coronal coordinate maximum is denoted with vertical blue line. The interface landmarks between the four bends are denoted with vertical black lines. (c) Estimation of central segment (bounded with two vertical magenta lines) and central landmark (vertical black line) of the posterior bend, using scale space. (d) The four bends with their central segments (in more saturated color: green, red, yellow) and central landmarks (black).

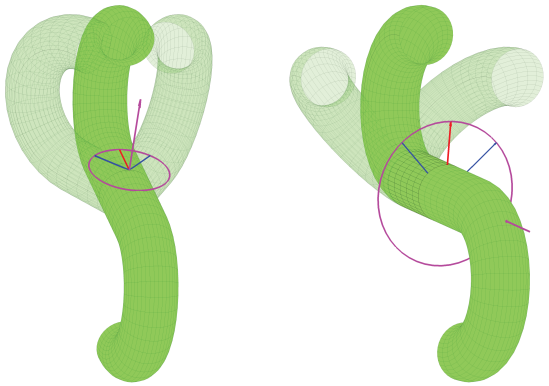

(a) OPR_1 **(b)** OPR_2

Figure 3.9, page 52: Illustration of the measured change of osculating planes between the posterior and the anterior bend. Each angle (between blue and red vectors) measures the rotation around the corresponding axis (magenta).

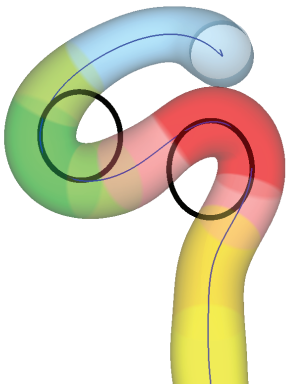

Figure 3.10, page 52: Circles (in black) fitted to the central segments of the anterior and the posterior bends.

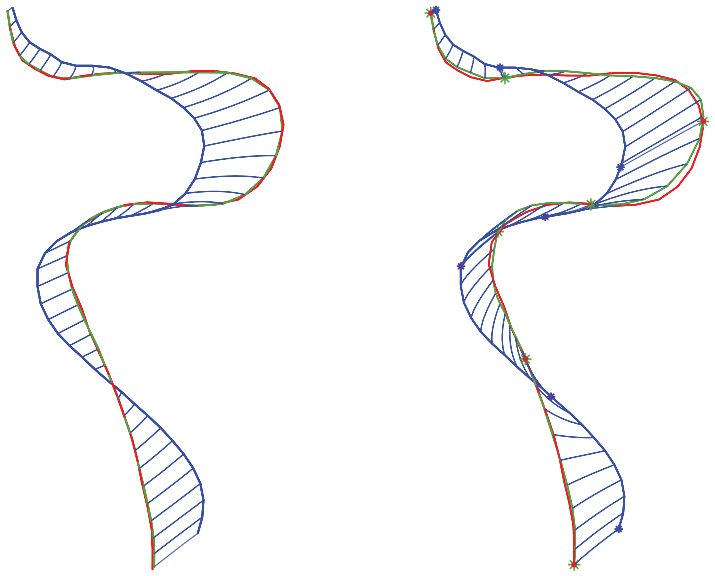

(a) $D = \rho(\phi_t) = 5.7$ **(b)** $D = \rho(\phi_t) = 6.8$

Figure 3.11, page 55: Diffeomorphic registration of source centerline (blue) to target centerline (red), with the registered centerline (green) and estimated distance D in shape space: (a) without ($E = E_{\text{cr}}$) and (b) with landmark matching term ($E = E_{\text{cr}} + E_{\text{lm}}$).

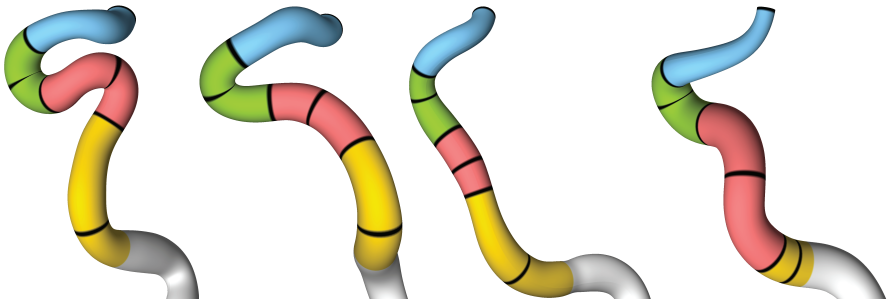

(a) **(b)** **(c)** **(d)**

Figure 3.14, page 59: Automated landmarking: (a-c) Examples of successful cases. (d) Example of a case where the posterior and the inferior bend were incorrectly detected as one ($\theta_{\text{post-inf}} = 40°$).

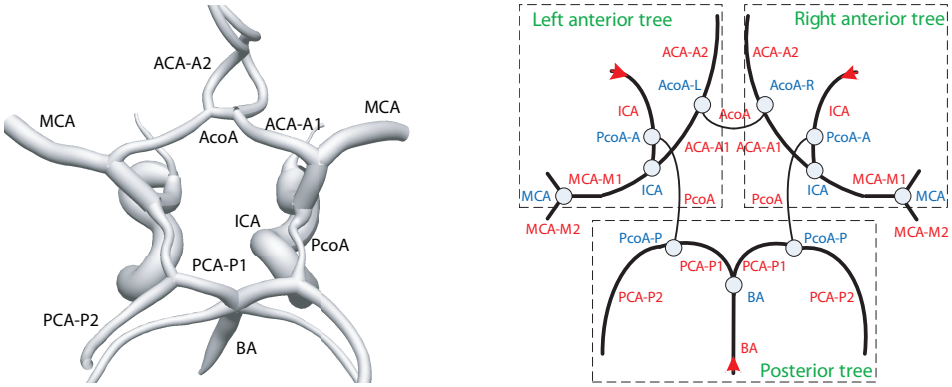

Figure 4.1, page 73: Anatomy of the Circle of Willis. (a) Surface rendering. (b) Schematic representation: The arteries (in red), the inflow (arrows), and the bifurcations of interest (in blue). Notation: '-A' denotes anterior, '-P' posterior, '-L' left and '-R' right.

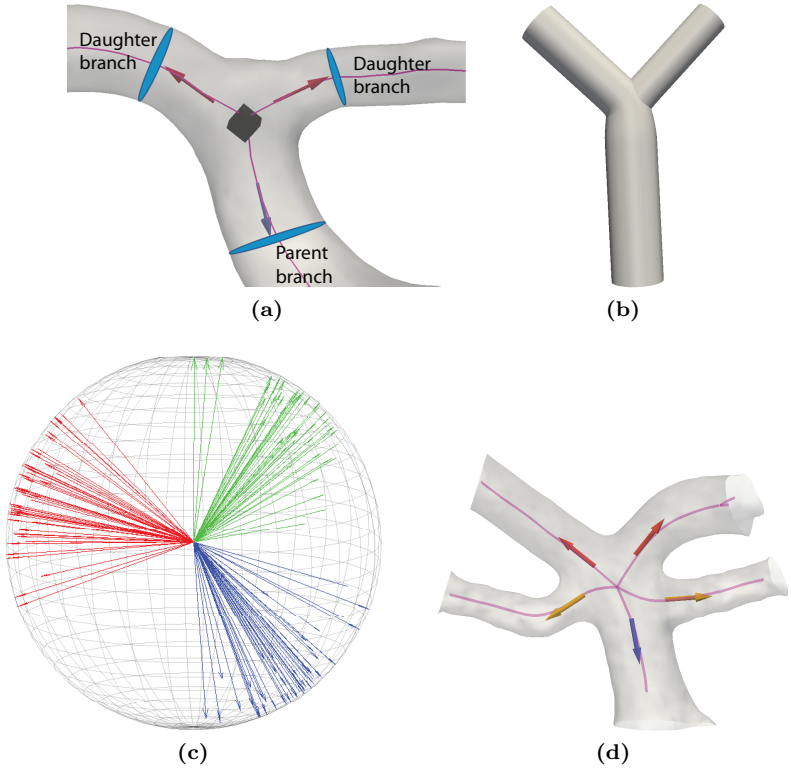

Figure 4.4, page 82: Unary attributes: (a) Bifurcation characterization, (b) general cylindrical model of a bifurcation, (c) distribution of bifurcation vectors (example for a terminal ICA bifurcation), (d) example of BA bifurcation (parent in blue and daughters in red) forming part of a quadfurcation.

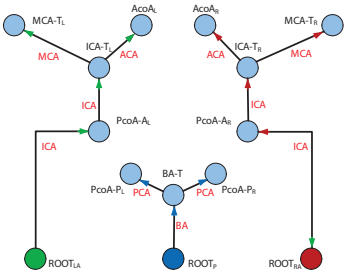

(a) ST1: Three isolated trees

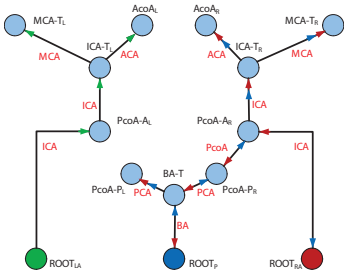

(b) ST2: Left ant. tree isolated

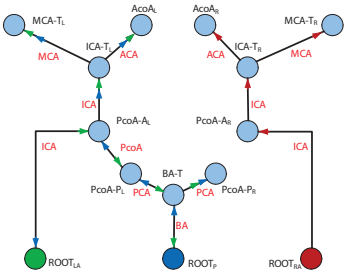

(c) ST3: Right ant. tree isolated

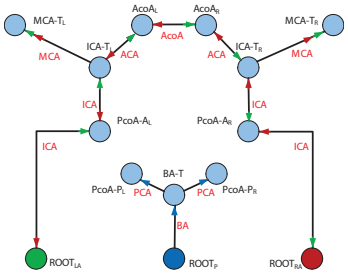

(d) ST4: Post. tree isolated

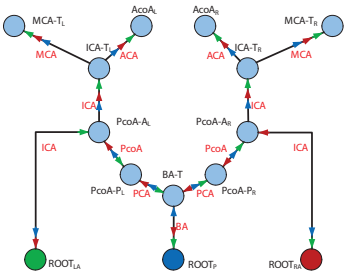

(e) ST5: Conn. via post. tree

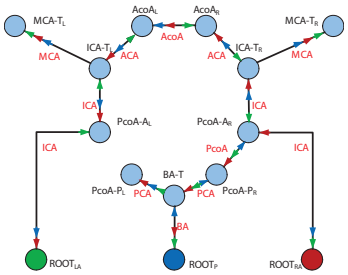

(f) ST6: Conn. via right ant. tree

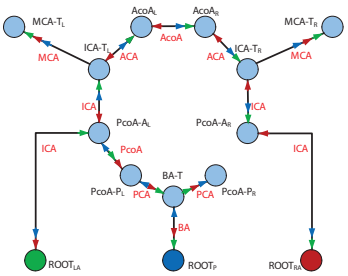

(g) ST7: Conn. via left ant. tree

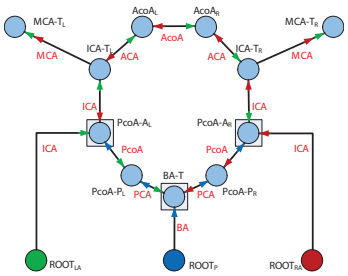

(h) ST8: Complete CoW

Figure 4.6, page 85: The eight reference graphs with overlayed digraphs, induced by each root of the graph. In (h), the *joining vertices* are denoted with square.

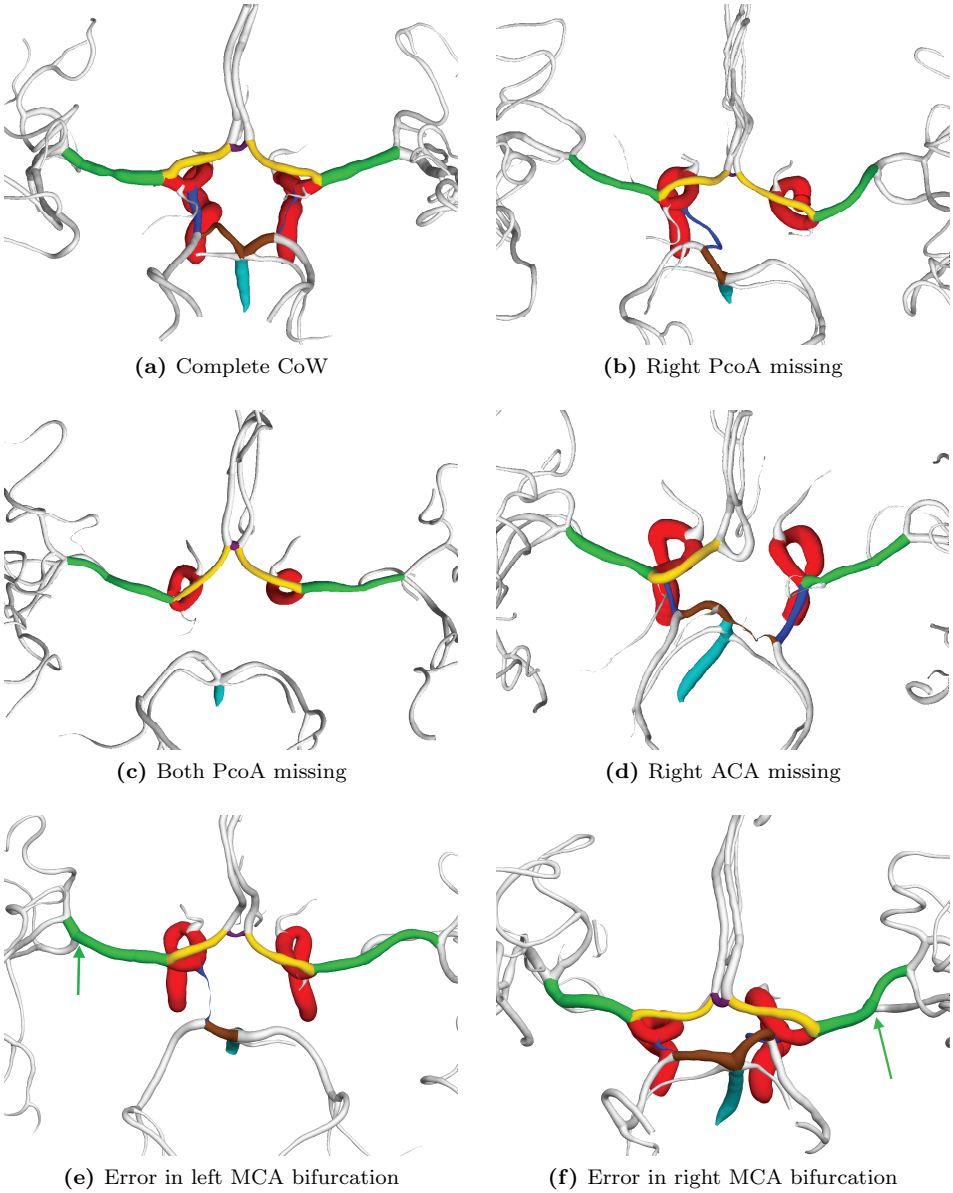

(a) Complete CoW

(b) Right PcoA missing

(c) Both PcoA missing

(d) Right ACA missing

(e) Error in left MCA bifurcation

(f) Error in right MCA bifurcation

Figure 4.7, page 89: Anatomically labeled Circle of Willis. Denoted vessels: ICA (red), BA (turquoise), ACA (yellow), PCA (brown), PcoA (blue), AcoA (purple), MCA (green). Correct labeling is shown in (a-d). Examples of incorrect MCA labeling are shown in (e,f), where the arrow denotes the true terminal bifurcation.

Notes:

Notes: